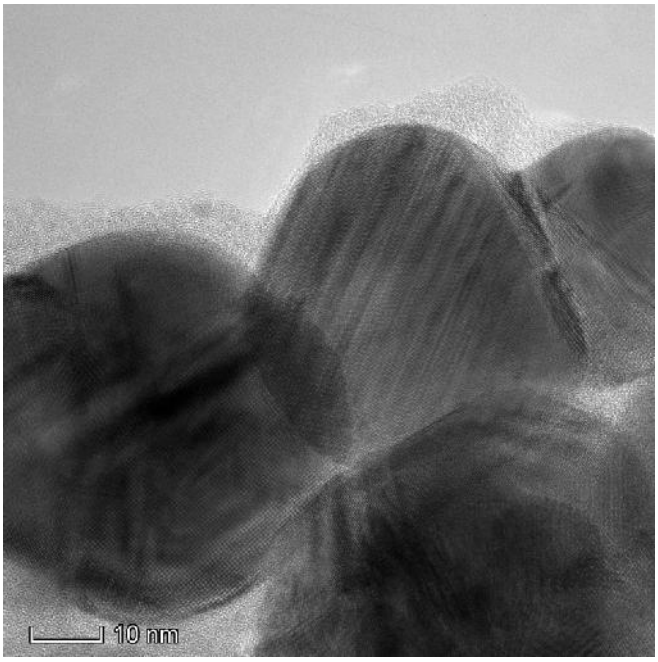

ADAMA SCIENCE AND TECHNOLOGY UNIVERSITY

SCHOOL OF APPLIED NATURAL SCIENCE

DEPARTMENT OF APPLIEDCHEMISTRY

SYNTHESIS OF GREEN Ag-BENTONITE & ZnO-BENTONITE NANOCOMPOSITE FOR ANTIBACTERIAL APPLICATION

THE PROJECT TEAM MEMBERS ARE:

1. Dr. Enyew Amare (PI)
2. Dr.Teshome Abdo (Co)

November 2023

Adama, Ethiopia

Table of Contents i
List of Tables iv
List of figures v
Abbreviations ix
Acknowledgments x
Abstract xi
1. INTRODUCTION 1
1.1. Background 2
1.2. Statement of the Problem 3
1.3. General Objective 4
1.3.1. Specific Objectives 4
1.4. Significance and Benefits Derived From the Project 5
2. LITERATURE REVIEW 5
2.1. Clay Minerals 6
2.1.1. Bentonite Clay 6
2.1.2. Structure of Bentonite Clay 7
2.1.3. Type of Bentonite Clay 8
2.1.3.1. Sodium Bentonite 8
2.1.3.2. Calcium Bentonite 8
2.1.4. Properties of Bentonite Clay 9
2.1.5. Anti-bacterial Activity of Bentonite Clay 9
2.2. Silver Metal and Silver Nanoparticle for Antibacterial Activity 10
2.3. Silver Bentonite nanocomposite for Antibacterial Activity 11
2.4. Zinc Oxide Nanoparticles (ZnO NPs) 12
2.5. Zinc Oxide/Bentonite Nanocomposite 12
2.6. Hagenia abyssinica leaf for Silver nanoparticles synthesis 13
3. MATERIALS AND METHODS 17
3.1. Study sites description 17
3.2. Chemicals and apparatus 17
3.2.1. Chemicals 17
3.2.2. Apparatus and Instruments 18
3.3. Methods 18
3.3.1. *H. Abyssinica* Plant Leaves Powder preparation 18

3.3.2. Preparation of Aqueous Plant Leaf Extract 19
3.3.3. Phyto-chemical screening of *H. abyssinica* plant leaf extract 19
3.4. Synthesis of Ag NPs 21
3.5. Synthesis of Zinc Oxide NPs 22
3.6. Purification and Activation of Bentonite 22
3.6.1. Purification of Bentonite 22
3.6.2. Activation of bentonite by sodium carbonate 23
3.7. Synthesis of Zinc Oxide-Bentonite Nanocomposite 24
3.8. Synthesis of Ag-Bentonite Nanocomposite 25
3.9. Characterization Techniques 25
3.9.1. Thermal analysis (TGA/DTA) 25
3.9.2. X-RAY Diffraction (XRD) 25
3.9.3. UV-visible spectroscopy (UV–Vis) 26
3.9.4. Bentonite Analysis 26
3.9.5. Image analysis 27
3.9.6. Fourier transforms infrared spectroscopy (FTIR) analysis 28
3.10. Antibacterial Test 28
3.10.1. Disc Diffusion Methods 28
3.10.2. Determination of MIC and MBC 29
4. RESULTS AND DISCUSSION 31
4.1. Phytochemical screening of the plant leaf extract 31
4.2. Compositional analysis of Bentonite 31
4.3. Analysis of XRD Results 32
4.3.1. XRD analysis of Bentonite 32
4.3.2. XRD Results of ZnO NPs 36
4.3.3. XRD analysis of ZnO-bentonite NCs 37
4.4. Scanning Electron Microscpy(SEM) Analysis 39
4.4.1. SEM Analysis of Bentonite 39
4.4.2. SEM Analysis of ZnO & ZnO/Bentonite 41
4.5. Characterization by UV-Vis spectroscopy 42
4.5.1. UV-Vis spectra of ZnO NPs 42
4.5.2. UV-Vis Absorption Spectra of ZnO-bentonite NCs 43
4.5.3. UV-Vis Diffuse Reflectance Spectroscopy of ZnO/Bentonite 44

4.6. Thermal Analysis (TGA/DTA) 46
4.6.1. Thermal analysis of ZnO NPs 46
4.6.2. Thermal Analysis Result of Activated Bentonite 47
4.6.3. Thermal Analysis Result of ZnO-Bentonite NCs 48
4.7. HRTEM images and SAED of ZnO, ZnO/Bentonite 49
4.8. FT-IR Results of Bentonite, ZnO, ZnO/Bentonite and leaf Extract 51
4.9. X-ray Diffraction (XRD) Analysis **Ag-NPs and Ag-Bentonite** 57
4.9.1. X-ray Diffraction Analysis **of Ag-NPs** 57
4.9.2. XRD analysis for Ag-Bent NCs 58
4.10. UV-Visible Analysis and optical properties 60
4.10.1. Variation of $AgNO_3$ concentration and optical properties of Ag NPs 60
4.10.2. Effects of volume ratio of $AgNO_3$ to plant leaf extract 63
4.10.3. UV-Vis of Ag/Bentonite 63
4.11. SEM-EDX of Ag NPs & Ag-Bentonite 64
4.12. HRTEM, TEM images and SAED of Ag NPs and Ag/Bentonite 66
4.13. FT-IR Results of Ag NPs & Ag-Bent 69
5. ANTIBACTERIAL ACTIVITY ANALYSIS AND DISCUSSION 71
5.1. Antibacterial Activity Results of ZnO NPs and ZnO/Bentonite NCs 71
5.1.1. MIC and MBC of ZnO/Bentonite Nanocomposites 80
5.2. Antibacterial Activity Analysis Results of Ag NPs and Ag-Bentonite 80
5.3. MIC and MBC of Ag/Bentonite Nanocomposites 85
6. CONCLUSION AND RECOMMEDATION 86
7. REFERENCES 87

#	LIST OF TABLES	page
Table 1	Phytochemical screening of the H. abyssinica plant leaves aqueous extracts	31
Table 2	Complete Chemical analysis (AAS and other techniques) of bentonite after sodium activation	32
Table 3	The interplanar spacing, and phases of raw, PB and Na-AB bentonite samples	35
Table 4	Average crystallites size and inter-planar d-spacing for the major peaks of ZnO-bentonite NCs	38
Table 5	The d-spacing values for ZnO NPs from its SAED pattern	50
Table 6	FT-IR summary of the H.abyssinicaplant Leaf Extract	54
Table 7	Average particle sizes of Synthesized Ag NPs Samples	58
Table 8	The average particle sizes of Ag- Bentonite composite samples	59
Table 9:	The zone of inhibition in mm for extract,Na-Bent, synthesized ZnO NPs and ZnO/Bent NCs	78
Table 10	MIC (μgmL^{-1}) and MBC (μgmL^{-1}) of nanocomposites for E. coli and S. aureus bacterial strain	79
Table 11	Antibacterial activity of H. abyssinica plant extract synthesized Ag NPs	81
Table 12	Antibacterial activity of Ag NPs –Bentonite synthesized with different concentarion of $AgNO_3$	84
Table 13	MIC (μgmL^{-1}) and MBC (μgmL^{-1}) of nanocomposites for E. coli and S. aureus bacterial strain	86

#	LISTS OF FIGURES	Page
Figure 1	Structure of Na- Bentonite clay	7
Figure 2	Image of *H. abyssinica* tree along with its flowers	15
Figure 3.	*H. Abyssinica* plant leafs in the wet, dry and powder forms	19
Figure 4	Change in the colour observed during Ag NPs Synthesis	21
Figure 5a	Purification process of raw bentonite	23
Figure 5b.	Activation of purified betonite with Na_2CO_3 and mechanical stirring	24
Figure 6:	XRD Patterns of a) raw, Purified Bentonite and 5%Na-Bentonite and b) 5% Na-Bent (a) and b) Purified Bentonite	35
Figure 7	XRD patterns of ZnO NPs synthesized using different volumes of plant leaf extract	36
Figure 8	XRD analysis result of activated bentonite(AB5), ZnO (Z100), ZnO-bentonite NCs: (ZB50) (d), ZB100 (c) ZB200 (b) and ZB300(a)	37
Figure 9a	The SEM image and EDX spectrum of the purified bentonite	40
Figure 9 b	The SEM image of purified bentonite	40
Figure10 a	SEM micrograph and EDX of ZnO NPs annealed at 650°C	41
Figure 10b	SEM Images and EDX of ZnO/Bentonite calcined at 650°C	42
Figure 11	UV-Vis absorption spectra of ZnO NPs synthesized by different ratios of plant extract to zinc acetate solution	43
Figure 12	UV-Vis DRS absorption spectra of ZnO-bentonite NCs	44
Figure 13	The band gap energies of pristine ZnO (a), Activated Bentonite-AB (b), and composite of ZnO/Bentonite prepared with different volumes of plant extracts ZB100 (c), ZB200 (d) and ZB300 (e).	45
Figure 14(a)	Thermal analysis of synthesized ZnO NPs (1:2)	47
Figure 14(b)	Thermal analysis of 5% Na_2CO_3 activated bentonite clay	48
Figure 14(c)	Thermal analysis of ZnO-bentonite nanocomposites	49

Figure 15	HRTEM of ZnO NPs (a) and (b) TEM (c) &(d) IFFT with crystal planes (e) SAED pattern of ZnO NPs (1 to 8 spots) ((f) particle size distribution	50
Figure 16	(a) and (b) HRTEM of ZnO-bentonite NCs with different magnifications (c) SAED pattern of ZnO NPs.	51
Figure 17	FTIR spectrum of purified Bentonite	52
Figure 18	FTIR spectrum of 5% Na_2CO_3 activated Bentonite	53
Figure 19	FT-IR spectrum of *H. abyssinica* crude extract	54
Figure 20	ZnO synthesized with 1:1ratio (a), before calcination Z100 b) and Z100 calcinated at 500°C.	55
Figure 21	FT-IR spectra for (a)) ZB02 calcined at 650°C (b) as synthesized ZB02	56
Figure 22	XRD Patterns of the Ag NPs synthesized with different leaf extract volumes	57
Figure 23	XRD patterns of the Ag-Bent NCs	59
Figure 24	UV–Vis absorption spectra of Ag NPs synthesized using different $AgNO_3$ concentration	61
Figure 25	Optical energy band gap for AgNPs synthesized from different concentration of $AgNO_3$ using fixed volume of plant leaf extract.	62
Figure 26	UV-Vis absorption spectra of Ag NPs suspension by varying volume ratio of plant leaf extract for fixed volume of 2mM $AgNO_3$ solution	63
Figure 27	UV-Vis absorption spectra of bentonite, Ag NPs and Ag-bentonite NCs	64
Figure 28	SEM –EDX of as synthesized Ag NPs using leaf extract of *H. abyssinica*	65
Figure 29	SEM –EDX of as synthesized Ag/Bentonite NPCs using leaf extract of *H. abyssinica*	66
Figure 30	a) TEM of Ag NPs, c) SAED pattern of Ag NPs (1 to 4 spots) (d) HRTEM with crystal planes	67
Figure 31	Ag/Bent NCs a) TEM images b) HRTEM, (c) SAED spots and (d) histogram of size distribution	68

Figure 32	FTIR spectra of Ag NPs and Ag-Bent NCs	70
Figure 33	The zone of inhibition measured for a sample at different concentrations	71
Figure 34	(a & b): Zone of inhibition of 5% Na-Bent and Aqueous extract of *H. abyssinica* at different concentration against *E. coli* and *S. aureus* bacterial strain	72
Figure 35	(a & b): Zone of inhibition of synthesized ZnO NPs at different concentration against *E. coli* and *S. aureus* bacterial strain	75
Figure 35	(c & d): Zone of inhibition of synthesized ZnO/Bentonite nanocomposites at different concentration against *E. coli* and *S. aureus* bacterial strain	76
Figure 36	Zone of inhibition of synthesized Ag NPs with different extract volume against *E. coli* and *S. aureus* bacterial strain	82
Figure 37	Zone of inhibition of synthesized Ag-Bentonite nanocomposite with different Ag NO_3 concentration against *E. coli* and *S. aureus* bacterial strain	85

ABBREVATIONS

AAS	Atomic absorption spectroscopy
Ag NPs	Silver nanoparticles
APHRRLC	Adama Public Health Research and Referral Laboratory Center
ATCC	American Type Culture Collection
ECC	Cation exchange capacity
CFU	Colony forming unit
DMSO	Dimethyl sulfoxide
DNA	Deoxyribonucleic acid
DTA	Differential thermal analysis
EDX	Energy Dispersive Spectrometry
FT-IR	Fourier Transmission Infra-red
H. abyssinica	*Hagenia abyssinica*
HRTEM	High Resolution Transmission electron microscopy
FWHM	Full width half maximum
JPCDS	The Joint Committee on Powder Diffraction Standards
MIC	Minimum Inhibitory Concentration
MBC	Minimum Bactericidal Concentration
MMT	Montmorillonite
Na-AB	Sodium Activated Bentonite
NCs.	Nanocomposites
NPs	Nanoparticles
PB	Purified bentonite
RNA	Ribonucleic acid
ROS	Reactive oxygen species
SAED	Selected Area Electron Diffraction
TEM	Transmission electron microscopy
TGA	Termo-gravimetric analysis
UV-Vis-DRS	UV-Visible-Diffuse reflectance spectroscopy
XRD	X-Ray Diffraction

ACKNOWLEDGMENTS

We are grateful to Adama Science and Technology University for financial support. This research work would not have been realized without the financial support of the Research Office of Adama Science and Technology University. We would like to give our gratitude to Dr. Bedassa Abdissa for facilitating administrative issues. We acknowledge Adama Public Health Referral & Research Laboratory for allowing us to conduct all the Microbial tests. We would like to acknowledge Dr. Ananda Murthy for taking our samples for SEM/EDX & HRTEM analysis to Indian materials testing laboratory. We also would like to express our gratitude to Mr. Jemal Adem, Mr. Adisu Girma, Ms. Heledana Aderajew, Ms. Sena Megerssa, and Ms. Sisay Geda for their valuable contributions during experimental work and sample collections. We would like to express our gratitude to all the applied chemistry staff of ASTU for their moral support and fruitful suggestion and constructive comments during the proposal review, progress report, and final report presentation.

ABSTRACT

The World Health Organization (WHO) estimated that, by 2050 bacterial infections, which are caused by two or more bacterial species, will cause more deaths than cancer. This implies the need to develop new antibacterial agents. This project work reports the synthesis and characterization of Ag/Bentonite, and ZnO/Bentonite nanocomposites (NCs) using *Hagenia abyssinica* plant extract and their antibacterial study. The synthesized NCs were characterized by using many advanced techniques such as; X-ray diffraction (XRD), thermal analysis (TGA/DTA), UV-Vis/DRS, FTIR, SEM/EDX and high resolution transmission electron microscopy (HRTEM). The FTIR spectral analysis revealed the presence of hydroxyl, carbonyl and other functional groups in the synthesized NCs. The TEM analysis revealed the formation of Ag NPs and ZnO NPs with hexagonal, rod-shaped and spherical structures and average particle sizes of 52 nm and 17.9 nm respectively. HRTEM also revealed the presence of (101) plane of ZnO and (002) plane of bentonte in ZnO/Bentonite nanocomposite with average composite particle size of 15.7 nm. The SAED of Ag/Bentonite displayed five spots; two spots ((100) and (300)) of bentonite planes and three spots; (111), (220) and (311) of Ag NPs planes of the composite. The antibacterial activities of the composites suspension were evaluated against *E. coli* ATCC 25922 and *S. aureus* ATCC 25923 by the disk diffusion and broth dilution methods. The inhibition zone results of ZnO/Bentonite nanocomposites suspension synthesized with 300 ml (ZB300)and 50 ml of (ZB50) volumes of plant extract at 30 mg/mL are 15.3 ± 0.2 mm and 10±0.3 mm against *E. coli* ATCC 25922 and 13.3 ±0.3 mm and 8±0.3 against *S. aureus* ATCC 25923 respectively. All the Ag/Bentonite synthesized for this work inhabited better than ZnO/Bentonite at one third concentration of the suspension (10 mg/mL) against both bacteria strains. The minimum inhibitory concentration (MIC) and minimum bactericidal concentration (MBC) values of ZnO/Bentonite (Z300) and Ag/Bentonites NCs (AB01) were found to be $6.25x10^{2}$ μgmL^{-1}, $1.25x10^{3}$ μgmL^{-1} and 78.125 μgmL^{-1}, 156.25 μgmL^{-1} for *E. Coli and* 78.125 μgmL^{-1}, 156.25 μgmL^{-1} and 39.1 μgmL^{-1} , 78.125 μgmL^{-1} S. aureus respectively. This investigation results revealed that bio-synthesized ZnO/Bentonite nanocomposites is a promising bactericidal composite.

Keywords**:** *Bentonite, Nanocomposite, Hagenia abyssinica, Inhibition zone, bactericide*.

SYNTHESIS OF GREEN Ag-BENTONITE & ZnO-BENTONITE NANOCOMPOSITE FOR ANTIBACTERIAL APPLICATION

1. INTRODUCTION

1.1. Background of the Study

Developments of inorganic antibacterial materials that inhabit bacterial growth have been of great interest in recent years due to the increasing of antibiotics resistance bacteria and their potential use in everyday products. Metal and metal oxide nanoparticles have gained a lot of attention as antibacterial materials. Nanoparticles are attractive because of their high reactivity, high surface atoms and large surface area to volume ratio (Sánchez-López ., 2020). The most common metallic and metal oxide inorganic materials with antibacterial properties are: pure Silver (Ag) (Franci et al., 2015, Brandell et al., 2017, Cakić et al., 2016), Copper (Cu)(Alzahrani and Ahmed, 2016, Cubillo et al., 2006), Iron (Fe)(Rajendran and Sengodan, 2017), and Zinc (Zn) (Demissie et al., 2020) etc. Recently, metals and metal oxides loaded in to clay (Motshekga et al,, 2013, 2015, Pouraboulghasem et al., 2020), zeolite (Hrenovic et al.,2012, Demirci, et al., 2014), graphene oxide(Shao et al. 2015) and other have been antibacterial agents under investigations.

Among metal nanoparticles, silver (Ag) metal is used for disinfection, in particulate form, suspension form or as coatings materials (Chernousova and Epple, 2013). Silver has been known for its antibacterial and therapeutic capabilities for ages. As a result, Ag-based compounds have become increasingly popular as antibacterial agents (Rahmati et al., 2020). These agents included Ag nanoparticles (Rajakannuet al., 2015), Ag nanocomposite (Yang et al., 2015) and Ag sulfadiazine (Aguzzi et al., 2014). On the other hand, there are also various innovative Ag based products which have been produced and studied recently such as structural modified Ag-loaded montmorillonite (Cao *et al.*, 2014), Ag nanoparticle–ionic silsesquioxane (Schneid et al ., 2014), nano-Ag fluoride in treating dental decay in children (Targino et al., 2014) and incorporation of silver nanoparticles into acrylic bone cement (Slane et al.,2015). Silver Nanoparticles (Ag NPs) have attracted a lot of attention among noble metal nanoparticles because of their appealing physicochemical features (Theivasanthi and Alagar, 2011). ZnO NPs possesses some antibacterial effect, good thermal qualities, low cost and little toxicity and has found a wide range of applications, including antibacterial, photoluminescence, optoelectronics, solar cells, catalysts, nanomedicine, pharmaceuticals

and cosmetics (Demissie et al., 2020). Biosynthesized ZnO NPs exhibit strong antimicrobial behaviours against bacterial and multifunctional behaviours and dynamic antibacterial activity (Nagarajan and Rajagopalan, 2008).

Furthermore, combining nanoparticles with other environmentally friendly, low cost and stable materials is ongoing to take advantage of their full properties in various applications. Nanoparticle can be applied on substrates in order to be used as an antibacterial agent (Suyoulema et al,, 2009). In this regard, clay mineral-based antibacterial complexes have been developed by a variety of method involving between the clay minerals and antibacterial substances to increase the strength of the interactions between clay and NPs. Clay minerals are hydrated alumino-silicates that contain alkaline and alkaline earth metals in general. They are great fillers for metal composites and good metal ion supporters (Lavorgna *et al.*, 2014). Among the clay, bentonite is considered as the main source in bioactive fields. It consists of microcrystalline particles of montmorillonite (MMT) which belongs to 2:1 phyllosilicate clay with one octahedral sheet of aluminum ion sandwiched between two tetrahedral sheets of silicon ions. The structural characteristics and multifarious application of bentonite are improved by replacing exchangeable inorganic cations (e.g. Na^{+},Ca^{2+},H^{+},K^{+}) on the interior and exterior surfaces with inorganic cations such as Ag nanoparticles (Krishnan and Mahalingam 2017). Because of its low cost and availability as well as its stable mechanical and chemical property, surface area (650 – 800 m^2/g), bentonites are being used for ion exchange and adsorption applications (Pourabolghasem et al., 2016). Because of this feature, they can be used for incorporation of various positively (cationic) charged inorganic compounds.

In this work, we prepared silver nanoparticles (Ag NPs), ZnO NPs, Zinc oxide-Bentonite nanocomposites (ZnO-Bent) and Silver–Bentonite nanocomposite (Ag-Bent NCs) using the leaf of *H. abyssinica* for antibacterial activity. The plant is chosen as a reducing and capping agent for the synthesis of Ag NPs, ZnO NPs, Zinc oxide-Bentonite NCs and Silver–Bentonite NCs.

1.2. Statement of the Problem

Drug resistance bacteria are a common problem and different antibacterial activities have been developed from different materials (Nikaido, 2009). The most excellent inorganic antibiotics nanomaterials, Ag and ZnO nanoparticle, are widely used in a growing number of applications due to their unique properties. According to the work of (Panyala et al. 2008) silver nanoparticles shows toxic effects at low concentration level on human-friendly microbes like heterotrophic (nitrogen-fixing and ammonifying bacteria) and chemolithotrophic bacteria in soil communities However, with the accelerating introduction of Ag NPs into commercial products, there is the possibility of this toxic nanoparticles enter into the environment, which gives rise to health and environmental concerns. According to the review work by (Froggett et al., 2014, Motshekga et al.,2013) and others insignificant amount of nanoparticles released from solid nanocomposite and easily stabilized in the soil and other environment. Review reports showed that clay doesn't cause any side effect, plentiful, non-toxic, inexpensive, possesses excellent adsorption property and Eco friendly. In recent years, clay mineral-based antibacterial complexes have been prepared by a series processes between the clay minerals and antibacterial materials to strength the bonds between clay and NPs. Hence, nanoparticles loaded into solid clay (bentonites), slowly released into the environment from its matrix, interact with soil and sediment to form inert aggregate. This work is trying to fill this gap by preparation of composites from bentonites with silver nanoparticle and ZnO NPs by using phytochemical aqueous extract of *H. abyssinica* to investigate the antibacterial activity of the as synthesized nano-composites.

1.3. Objectives of the Study

1.3.1. General Objective

- The general objective of this study is to Synthesis Silver-Bentonite Nanocomposite and ZnO-Bentonite Nanocomposite for antibacterial applications.

1.3.2. Specific Objectives

The specific objectives of this study are

- Preparation of Na-bentoinite from purified raw bentonite and evaluates the conversion efficiency by complete silicate analysis.
- Synthesis of silver nanoparticles and Ag-bentonite nanocomposite using *Hagenia abyssinica* aqueous leaf extract.
- Synthesis of ZnO nanoparticles and ZnO bentonite nanocomposite using *Hagenia abyssinica* aqueous leaf extract
- Characterization of the synthesized, silver Nanoparticles, Zinc oxide nanoparticles, silver-bentonite nanocomposite ZnO/bentonite nanocomposite using UV-Visible, FT-IR, XRD, SEM/EDX and HRTEM.
- Assessing the antibacterial activities of, *Hagenia abysinica* plant leaf, Na-Bentonite, Ag NPs, ZnO NPs, Ag- bentonite and ZnO/bentonite nanocomposite using agar diffusion method against gram-positive *Staphylococcus aureus and* gram-negative *Escherichia coli* selected strain of bacteria.

1.4. Significance and Benefits Derived From the Project

The significance of this study was to utilize locally available natural materials to develop new alternative and improved environmentally friendly antibacterial agent. Developing composite with high medicinal value from low cost, abundant, local raw materials for technological application is expected to encourage more entrepreneurs and researchers in the area. The project can be considered to be of particular interest, being it is part of the country's research focus area, health care. The project contributed to the socio-economic developments of the country through human resource development by involving five graduate MSc students.

1.5. Expected Output

The possible expected output from this project is a new green nano-composite with the improved antibacterial property over the established silver and zinc oxide nano-particles. Two articles were also published from this work on Scopus and science citation indexed journals, and Adama Science and Technology University was also acknowledged.

2. LITERATURE REVIEW

2.1. Clay Minerals

"Clay mineral" refers to phyllosilicate minerals, flexible and plastic when wet but hardens when dried or burnt, which are layer silicates that form at the earth's surface as a result of chemical weathering of other silicate minerals (Ani, 2018).

These materials are characterized by their extremely small size (a few micrometers at the most extreme) and occur under surface environments (Maisanaba et al., 2015). Clays have a variety of physicochemical properties, such as swelling, adsorption, ion exchange, and surface acidity (Yang et al., 2006). They are sheet silicate family of minerals, which have layered structures composed of polymeric SiO_4 tetrahedral sheets linked to sheets of (Al, Mg, Fe)$(O,OH)_6$ octahedral (Ani, 2018). Common clay minerals are Kaolinite(1:1phyllosilicates), Smectite, Sepiolite, Illite, Chlorite, and Vermiculite (2:1phyllosilicates) (Manfredini and Hanuskova, 2012). They are very different, even though each is composed of octahedral and tetrahedral sheets as their basic building blocks. However, the arrangement and composition of the octahedral and tetrahedral sheets account for most of the differences in their physical and chemical properties (Maisanaba et al., 2015).

2.1.1. Bentonite Clay

Bentonite clay is known as montmorillonite (MMT). It belongs the smectite clay family, which is mainly formed by aged volcanic ash clay mineral. This substance resulted from the alteration of glassy material ejected from volcanoes or the alteration of silica-bearing rocks like granite and basalt during geological time. In addition to MMT it also contains a variety of clay minerals such as Beidellite, Nontronite, Saponite, Saponite etc. The ideal half-cell chemical formula for montmorillonite is $M\ 0_{.33},H_2O\ Al_{1.67}(Fe^{2+},\ Mg^{2+})_{0.33}\ Si_4O_{10}(OH)_2$, where *M* refers to a metal cation in the interlayer space between sheets. The tetrahedral cations are Si^{4+} and the octahedral cations are Al^{3+}, Fe^{2+}, and Mg^{2+} (Pourabolghasem et al.2016). The chemical properties of bentonite can be altered by adding highly ionic, stable, and higher density species to the bentonite clay interlayer through an ion-exchange and

sorption process. Thermal and chemical changes can improve the adsorption capability of bentonite. For enhancing the adsorption capacity of bentonite, a variety of surface modification techniques, including as heat and acid treatment, can be utilized (Şahin et al., 2015).

2.1.2. Structure of Bentonite Clay

This type of clay is characterized by 2:1 phyllosilicate clay, with one octahedral sheet sandwiched between two silica tetrahedral sheets forming a unit crystal structure. Positive cations and water molecules make up the interlayer between units. Due to this crystalline arrangement, bentonites are able to expand and contract the interlayer with its two dimensional crystallographic integrity (Motshekga et al.,2013). Because of its structure, it can be used as a carrier. The porous structure of bentonite is roughly divided into three categories: micro-pores, meso-pores, and macro-pores, according to *Babaki, H.et al.* Micro pores are smaller than 2 nm, between 2 nm and 50 nm are meso pores and larger than 50 nm are macro pores (Babaki et al., 2008).

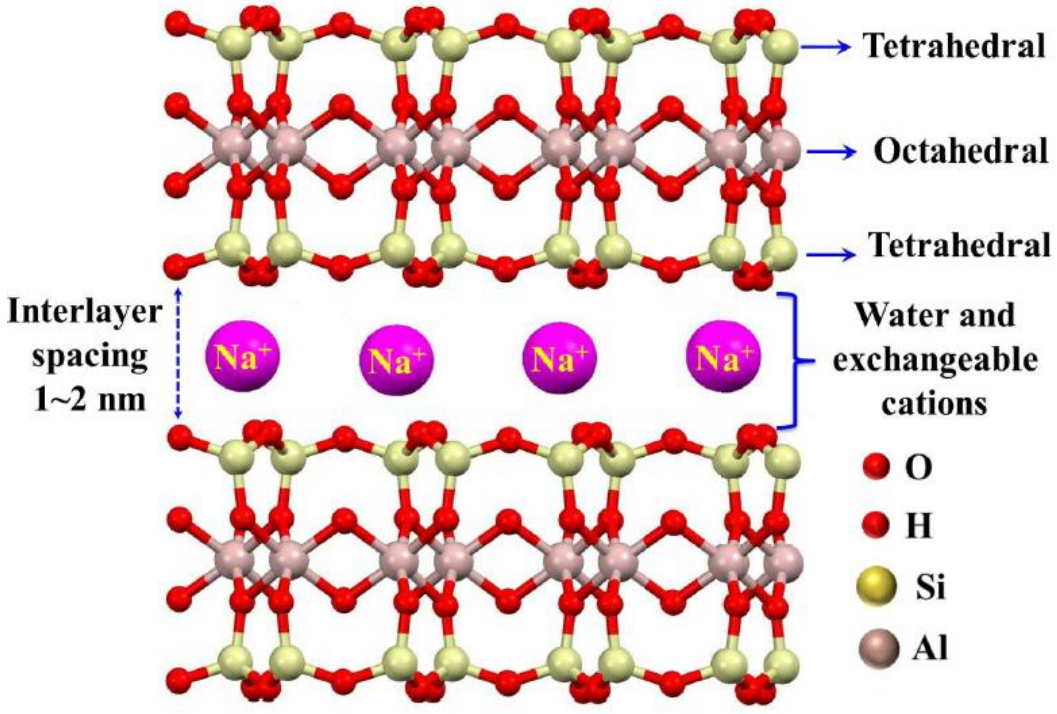

Figure 1: Structure of Na- Bentonite clay

As a result, they are classified as expandable 2:1 phyllosilicate clays with permanent charges that may interchange cations and anion. Both layers of these sheets contain oxygen atoms. These three –layer units are stacked (piled up) one on top of the other, with oxygen in surrounding layers next to each other. This results a weak bond, enabling water and other polar molecules to pass between layers and cause the mineral structure to expand (swelling). Silicon can be replaced by aluminum or iron in tetrahedral coordination (Allo and Murray, 2004). Substitution allows magnesium, iron, lithium, chromium, zinc, or nickel to be substituted for aluminum in the octahedral coordination. The different montmorillonite clay minerals are formed by differences in replacements within the lattice in terms of location and elemental content (Kim et al., 2016).

2.1.3. Types of Bentonite Clay

Bentonite clay can be classified in to K, Na, and Ca bentonite depending on the dominant element constituent, but the main two types of bentonites are Sodium (Na) and Calcium (Ca) are recognized, and the uses of each depend on specific physical properties(Uddin, 2018).

2.1.3.1. Sodium Bentonite

Sodium bentonite has single water layer particles that contain Na^+ as the exchangeable ion. When wet, it swells and absorbs up to several times its dry mass in water. Swelling of bentonite is mostly induced by montmorillonite swelling (Hayati-Ashtiani and Azimi, 2016). Swelling is an important property of clay mineral, because of this property it is the most useful material that can absorbs large quantities of water and swelling to many times than their original volume and gives rise to permanent suspension of gel like masses used for different applications (Fernández et al., 2004).

2.1.3.2. Calcium Bentonite

Calcium bentonite is a useful adsorbent of ions in solution, decolorize fats and oils. Calcium bentonites are non-swelling and break down to finely granular aggregate that is widely used as an absorbent clay sometimes called fuller's earth (Fernández et al., 2004). By using an ion exchange method, calcium bentonite may be transformed to sodium bentonite (also known as

sodium activation) to display sodium bentonite's properties. Using a soluble sodium salt, such as sodium carbonate, soda activation has high montmorillonite content. Some properties of sodium-beneficiated calcium bentonite (or sodium-activated bentonite) are high swell potential, small particle size, and high specific surface area than Ca-montmorillonite (Christidis et al., 2006).

2.1.4. Properties of Bentonite Clay

The widespread use of bentonite can be attributed to its physical and chemical properties such as small particle size, high porosity, large surface area and high cation exchange capacity. It has excellent adsorption capacity and its adsorption ability is determined by the chemical nature and pore structure (Doulia et al., 2009). The exceptional adsorption properties and cationic exchange capacity originated from the fundamental crystalline arrangement, which consists of two tetrahedral layers of silica connected by one octahedral layer of alumina. Each one is separated by an interlayer gap, which contains exchangeable cations (Na^{+}, Ca^{2+}, Mg^{2+}) to counteract the structural superficies' apparent negative charge caused by isomorphic replacements of less-charged cations in the octahedral sheet (Keller-Besrest et al.,1994).

Sodium bentonite is most widely known for its ability to swell. It can absorb nearly 5 times its weight in water and at full saturation may occupy a volume 12 to 15 times its dry bulk. The high water absorption capacity of bentonite also makes it very plastic and resistant to fracturing or cracking. Sodium bentonite has an exceptionally high surface area of 600 to 800 square meters per gram. Less than 10 grams of bentonite, if fully dispersed, could cover a football field. It is a combination of these physical properties that make sodium bentonite an ideal material (Zuber et al., 2010).

2.1.5. Antibacterial Activity of Bentonite Clay

Bentonite is a widely distributed, low-cost mineral that possesses high ion adsorption, porosity, and microbial adhesion, as well as being environmentally friendly (Sajadi et al., 2018, Guo *et al.*, 2020). It is also considered as the main source in bioactive fields and it has been used in ancient and modern medicines because of their special layer structures, and a

wide range of multifarious and potential biomedical applications. It is microcrystalline particles of montmorillonite which may interact strongly with certain antimicrobials, affecting their bioavailability. Potentially, this interaction can be highly advantageous in the design of modified-release systems for the controlled administration of antibacterial substances, which nowadays is one of the most interesting fields for pharmaceutical and veterinary applications (Rapacz-kmita et al., 2017). As the montmorillonites layer structure gives the antimicrobial and antifungal carrier, it has the property of antibacterial and it can adhere to pathogens and excrete them, reinforce intestinal mucosal barrier and help regeneration of epithelium (Hu and Xia,2006). Bentonite can have varying antibacterial activity depending on its mineral composition, which can differ depending on where it comes from and how it is processed. Generally, bentonite that contains higher amounts of certain minerals like aluminum, iron, and magnesium tends to exhibit stronger antibacterial properties. Pharmacology studies have revealed that montmorillonite (MMT) adsorbed bacteria such as *E. coli, S. aureus* and immobilize cell toxins (Meng et al.,2009).

2.2. Silver and Silver Nanoparticles for Antibacterial Activity

Silver (Ag) is the metal of abundance, among the valuable metals for future applications in the areas of living organisms and biological systems. Silver (Ag) is a noble metal, is not attacked by water or acids. However, silver metal continuously releases small amounts of ions, which act antibacterial at the metal surface (Chernousova and Epple, 2013). It has a long history of use in medicine as an antimicrobial agent. Silver ions have been found to have antibacterial effects on some microbes. Several studies have demonstrated that silver ions are selectively toxic for prokaryotic microorganisms, with little effect on eukaryotic cell (Park and Jang, 2003). I. Sondi and B. Salopek-Sondi reported that silver ions and silver-based compounds are highly toxic to microorganisms showing strong biocidal effects on as many as 16 species of bacteria including *E. Coli* (Sondi and Salopek-Sondi, 2004).

Silver is generally used in the nitrate form to induce the antimicrobial effect but when silver nanoparticles are used, there is a huge increase in the surface area available for the microbes to be exposed. Hernández Sierra *et al* compared the anti-Streptococcus mutants activity of nano scale silver, gold, and zinc oxide and found that silver nanoparticles (Ag NPs) worked

best (Hernández-Sierra *et al.*, 2008). Antibacterial activity against *Aspergillus niger, Bacillus subtilis, S. aureus, E. coli, Proteus vulgaris* and other investigations also reported the better results (Sondi and Salopek-Sondi, 2004). Silver is a well-known antibacterial agent against more than 650 microorganisms from various classes such as gram-positive and gram-negative, fungi or viruses. Out of the metals with antimicrobial properties, it was found that silver has the most effective antibacterial action and is the least toxic to animal cell (Ahmed et al., 2016).

Ag NPs are used in a growing number of applications across a diverse range of commercial consumer products such as food storage containers, coating materials, liquid fabric softeners and detergents, fabrics and clothing, sporting goods, cosmetics, wound dressings, toothbrushes, and antimicrobial coatings. According to reports from different group tons of nano-silver are added into the aquatic environment annually from wastewater plants (Sohn et al., 2015), septic tanks (Benn and Westerhoff, 2008) and agricultural lands (Kaegi et al., 2011). According to the work of (Panyala et al. 2008) silver nanoparticles shows toxic effects at low concentration level on human-friendly microbes like heterotrophic (nitrogen-fixing and ammonifying bacteria) and chemolithotrophic bacteria in soil communities. However, with the accelerating introduction of Ag NPs into commercial products, there is the possibility of this toxic nanoparticles enter into the environment, which gives rise to health and environmental concerns.

2.3. Silver Nanoparticles -Bentonite nanocomposite

Clays such as bentonite, kaolinite, halloysites, and palygorskite are commonly used supporting substrates for nanoparticles (Dutta & Wang, 2019; Krishnan & Mahalingam, 2017a). The unique properties of silver NPs (or its composites) and its supportive materials such as clay, ceramics, charcoal, silica beads, cotton fabric, filter paper, cellulose gels, alginate beads and polyurethane sponge have provided great opportunity to revolutionize the water disinfection systems which have achieved 99 to 100% of deactivation of bacteria (Bhardwaj et al., 2021). According to the work of (Motshekga et al.,2013) and others

insignificant amount of Ag nanoparticles released from silver –bentonite nano-composite in the water environment.

2.4. Zinc Oxide Nanoparticles (ZnO NPs)

Transition metal oxides nanomaterials are heavily studied. These oxides are of particular interest because of their varied metal to oxygen ratio and large number of phases with different structures, properties, and application. Zinc oxide (ZnO), which belongs to II-VI transition metal oxides, is one of the most widely studied oxides as a result of its interesting physicochemical, optoelectronic properties and its application in many areas including in catalysis, sensors, medicine, personal care products, paints, batteries, solar cells, memory devices, electronic and spintronics, and in agriculture to control crop disease and as bio fertilizer. In particular, by virtue of its chemical stability, biocompatibility and biodegradability nature, it has been extensively used as antibacterial agent in antifouling application and also in the radiation–assisted degradation of organic contaminants in wastewater treatment (Chaudhuri & Malodia, 2017; Mankad et al., 2016). ZnO NPs is the most commonly used nanomaterials in cosmetics, skincare products, and sunscreens to act as UV filters starting from size of 20 nm. It shows better dispersion and run off cosmetic materials(Fytianos et al., 2020).

2.5. Zinc oxide/Bentonite nanocomposite

There are challenges in the large-scale utilization of nanoparticles such as ZnO in water treatment and the likes due to the difficulty in their separation and recovery after treatment. In addition, the use of metal oxides nanoparticles for water treatment has some disadvantages, namely: (1) higher colloidal stability in aqueous solution, (2) agglomeration of the nanomaterials at high concentrations, and (3) difficulty in separating and recovering the nanomaterial after use (Lei et al., 2017). However, steps have been adopted in order to overcome these shortcomings. These include doping and co-doping of metal oxide nanomaterials and immobilization of nanomaterials on suitable matrices (Darvishi Cheshmeh Soltani et al., 2016). This suitable substrate could function as support in order to overcome the difficulties involved in post-separation and recovery. Moreover, the support of nanosized semiconductor materials on matrices could help to enhance their activity when compared

with ordinary nanomaterials. In this respect, various clay matrices such as kaolinite, montmorillonite, and bentonite have been successfully employed as support. An immobilizing and anchoring nanosized ZnO nanoparticle on the surface of clay minerals provide more active surface sites, reduces the agglomeration of the nanoparticles, and prevents the release of nanoparticles into the environment. Clay nanocomposites have become major components of clay with metallic nanoparticles used in recent research findings in tackling environmental pollutions. Since, ZnO nanoparticles are cheap, non-toxic, and capable of removing emerging contaminants, and given the fact that rural communities are affected by contaminants from wastewater, cheaper and environmentally friendly methods for the wastewater treatment need to be adopted for water and wastewater treatment (Chakraborty et al., 2019).

It has been demonstrated that using nanoparticles alone is dangerous, because their sizes can affect human health and the environment. To overcome this problem, hybrid processes were introduced by combining nanoparticles with other environmentally friendly materials, such as inert and stable materials to utilize nanoparticles' full properties in wide-range applications. Moreover, introducing nanoparticles with other substrates/fillers would result in composites with novel and enhanced properties that cannot be achieved by the individual components (Pouraboulghasem et al., 2016).

2.6. *Hagenia abyssinica* leaf for Silver nanoparticles synthesis

Hagenia abyssinica is the only species of the genus *Hagenia* and belongs to a monotypic genus in the family *Rosaceae* (Wolde et al., 2016). *Rosaceae* is a large family containing more than 100 genera and 2,000 species of herbs, shrubs, and trees (Kifle et al., 2021). *Hagenia abyssinica* is a tree up to 20 m tall, with a short trunk and thick branches. The bark, flower, leaf, and root parts of *H. abyssinica* have been used for both medical and nonmedical purposes (Feyissa et al., 2005). This tree species is known by its common name 'kosso' in Ethiopia. Currently, it is however sparsely distributed in mountainous areas in Central, South-western and South-eastern parts of Ethiopia. The species is also found in different parts of Africa such as Kenya, Tanzania, Burundi, Sudan, Democratic Republic of Congo,

Malawi, Uganda and Rwanda. *H. abyssinica* has been used as a remedy for intestinal parasites, and it has served as an anthelmintic in ruminants and also against tapeworms in humans (Assefa et al., 2010).

This strong medicine when taken in large quantities; it is sometimes taken as an abortifacient in traditional medicine the extract is used as abortifacient which initiated investigations examining it as a potential contraceptive agent (Wolde et al., 2016). Also its roots are cooked with meat and the soup drunk for general illness and malaria, while bark hammered and added to cold water and the liquid drunk as a remedy for diarrhea and stomach. Besides being a source of medicine, *H. abyssinica* has been utilized for various other purposes such as construction, furniture, fuelwood, soil fertility management, as fertile soil formation, soil conservation, as well as rainwater conservation (Feyissa et al., 2005).

Figure 2**:** picture of *H. abyssinica* tree along with its flowers.

H. abyssinica plant provides a rich and rare combination of zeatin, and it is loaded in nourishment owing to the presence of essential phytochemicals, It is rich in phytochemicals particularly secondary metabolites such as tannins, terpenoids, flavonoids, Saponins,

alkaloids, phlobathanins and phenol compounds which act as reducing, stabilization agents and that have been demonstrated to have antibacterial properties which are compounds that help in the characterization of this plant as a natural reducing agent of remarkable efficiency (Melkamu and Bitew., 2021, Murthy et al., 2020, Kilonzo and Munisi, 2021). Those biological active ingredients tend to reduce growth of bulk inorganic complex compounds into nanoparticles (Galan et al.,2021). Due to their strong tendency for chelating metals, these bioactive chemicals, such as phenol compounds, function as a ligand, particle size controller, and antioxidant, bind to metal ions and reduce and cap them to form nanoparticles. This compound have a very high tendency to bind metal ions that interact with polyphenol compounds and helps in the nucleation and formation of NPs due to the presence of hydroxyl and carboxylic groups (Murthy et al., 2020). In particular, the leaves extract of *H. abyssinica* are used owing to their medicinal values and chemical constituents which helps in the reduction of toxic contents from the Ag NPs (Ananda Murthy et al., 2020, Melkamu and Bitew., 2021, Kilonzo and Munisi, 2021, Obakiro et al 2021).

3. MATERIALS AND METHODS

3.1. Study Sites Description

Raw Bentonite was collected from Mille (Warssiso) (Elevation of 518 m above sea level, Latitude: 11° 25' 18" N, Longitude: 40° 45' 46" E.500 km from Addis Ababa), woreda of Awsi Rasu (Administrative Zone 1), Located in Afar Region, north-eastern Ethiopia. The plant *H. abyssinica* that used as a reducing and capping agents in the synthesis was collected from Adele town, Amigna Woreda (Elevation 2,475 m, Latitude 7°47′26″N, longitude 39°54′26″ E. 241 Km from Addis Ababa) East Arsi Zone, Oromia regional state, South Eastern of Ethiopia.

Plant extraction, bentonite purification, activation and synthesis of nanoparticles and nanocomposites using *H. abyssinica* medicinal plant leaf extract were carried out in the Applied Chemistry laboratory of Adama Science and Technology University (ASTU). The UV-Vis characterizations were conducted in Applied Biology laboratory; TGA, UV-Vis-DRS, and XRD analysis were conducted at the Materials Science Engineering laboratory, ASTU. Complete composition analysis of bentonite was conducted at Geological Survey of Ethiopia laboratory and FTIR analysis was performed at Addis Ababa University, Dept of Chemistry, antibacterial activity tests was conducted in Oromia Public Health Research and Referral Laboratory Centre, Adama. HRTEM, and SEM-EDX were conducted using JEM-2100 (accelerating voltage up to 200 kV, LaB6 filament), EDS-1.5 Å TEM resolution.

3.2. Chemicals and Apparatus

3.2.1. Chemicals

The important chemicals and reagents used for this project are presented in this section. Zinc acetate ($Zn(CH_3COO)_2{\cdot}2H_2O$)-99.9% AR analytical reagent (Guandong Guanglua Sci-tech Co., Ltd, France), Silver Nitrate ($AgNO_3$) (LOBA CHEMI), distilled water and ethanol (Wasse PHARMA PLC., 96-99%), Sodium carbonate (Na_2CO_3), Dimethylsulfoxide (DMSO)-(Sisco, Research laboratories Pvt. Ltd, India), Sodium Hydroxide (NaOH) was used as precipitating agent, Mueller Hinton agar (Sisco. Research laboratories Pvt. Ltd, India), Ethyl acetate ($CH_3CH_2OOCCH_3$), Ammonia (NH_3), Iodine (I_2), Potassium Iodide (KI),

Methanol(CH_3OH), 2, 4- Dinitrophenyl Hydrazine(2,4-DH), and Hydrochloric Acid (HCl) were also used.

3.2.2. Apparatus and Instruments

Glasswares (Beaker, Conical Fask, Pipette, Quartz Cuvete, Volumetric Flask, Funnels, Measuring Cylinder), Electronic Balance, Magnetic Stirrer with Hot Plate, Petri-Dish, Crucible, Mortar and Pestle, Dropper, Ball Milling, Centrifuge, Mechanical shaker were used. The instruments used were UV- Spectrophotometer (Perkin-elementary, Germany), Fourier transform Infrared spectroscopy (FTIR) (Perkin Elmer, Spectrum 65 FTIR, and USA), X-ray Powder Diffusion (XRD-700 shimadzuco, South Korea)(Cu-Kα1 radiation (λ=1.5406 A°) operating at 45 KV and 30 mA) and Atomic Absorption Spectroscopy(AAS). HRTEM, and SEM-EDX were conducted in Sprint Testing Solutions centre, India.

3.3. Methods

3.3.1. *H. Abyssinica* Plant Leaves Powder preparation

H. abyssinica plant leaf sample was washed four times with tap water followed by distilled water to remove unnecessary substance. The cleaned leaves were dried in open air under shadow for two weeks (15 days) to reduce the moisture content of the leaves. The dried leaves were crushed by using a domestic electrical grinding machine to produce a fine powder which was packed in a brown glass bottle to protect it from the effect of light (Susanto et al., 2018).

Figure 3**.** *H. Abyssinica* plant leafs in the; wet, dry and powder forms

3.3.2. Preparation of Aqueous Plant Leaf Extract

H. abyssinica plant aqueous leaf extract was prepared for the synthesis of the targeted material. For preparing the fresh leaf extract, 25 g of the powdered leaves of *H.abyssinica* was taken in a 1000 ml conical flask containing 400 ml of distilled water. The flasks were then covered with aluminium foil; to prevent the effect of light. After that, the contents of the flask was stirred using a hot plate magnetic stirrer for 90 min and allowed to warm at 50 ˚C for 1 h followed by cooling to room temperature. The content of the flask was left as such overnight. The prepared solution was centrifuged at 5000 rpm for 10 min to obtain a clear solution. The filtrate was stored at 4° and used for the synthesis of the targeted materials (Ahmed et al., 2016).

3.3.3. Phyto-chemical screening of *H. abyssinica* plant leaf extract

The medicinal value of traditionally important plant species is due to the presence of some chemical substances which produce a definite physiological action like alkaloids, tannins, flavonoids, saponins, etc (Edeoga et al., 2005). The preliminary phyto-chemical screening for the plant leaf of *H. abyssinica* were carried out to analyze the presence of different compounds as described below:

Test for Saponins: to 3 mL of the plant leaf extract 5 mL of distilled water was added and shaken vigorously in a test-tube for about 5 min, kept it to settle for 30 min to observe foam (appearance of creamy foam of small bubbles) which shows the presence of saponins (Auwal et al., 2014).

Test for flavonoids: 3 mL plant extract with 10 mL of ethyl acetate were mixed and heated with a steam bath for 3 min. The mixture was filtered and 4 mL of the filtrate was shaken with 1 mL of dilute ammonia solution and a yellow coloration was observed, which shows the presence of flavonoids (Tanaka et al., 1989).

Test for Phenols: 2 mL of plant extracts was put and treated with a few drops of 2% of $FeCl_3$ in test tube; the formation of bluish green or black coloration indicated the presence of phenols (Wolde et al., 2014).

Test for Alkaloids: 5 mL of plant extract was dissolved in 10 mL of 10% ammonia solution and extracted with 15 mL of chloroform. The chloroform portion was evaporated to dryness and the resultant residue dissolved in 15 mL of dilute sulphuric acid. Reddish brown colour was formed which showed the presence of alkaloids (Auwal et al., 2014).

Test for Tannins: A few drops of 10% ferric chloride ($FeCl_3$) solution added to 2 mL of the aqueous solution of the plant leaf extract. The occurrence of blackish blue color showed the presence of tannins (Tanaka et al., 1989).

Test for Terpenoids: 0.5 g of each crude powders were separately dissolved in 5 mL of methanol. 2 mL of the extract were treated with 1 mL of 2, 4- dinitrophenyl hydrazine were dissolved in 100 mL of 2M HCl. Yellow-orange colorations were observed as an indication of Terpenoids (Wolde et al., 2014).

Test for Steroids: 3 mL of plant extract was dissolved in 5 mL of methanol. 1 mL of the extract was treated with 0.5 mL of acetic acid anhydride and cooled in ice. This mixed with 0.5 mL of chloroform and 1 mL of concentrated sulphuric acid was then added carefully by means of a pipette. At the separations level of the two liquids, reddish-brown rings were formed, as indication of the presence of steroids(Melkamu and Bitew, 2021).

Test for Phlobatannins: 2 mL of plant extract was added to 2 mL of 1% HCl and the mixture was boiled. Deposition of a red precipitate was taken as an evidence for the presence of phlobatannins (Auwal et al. 2014).

3.4.Synthesis of Ag NPs

The Ag nanoparticles were synthesized using 0.2 mM $AgNO_3$ solution with different volume ratio of leaf extract prepared from 25 g in 400 ml distilled water. First 25 ml of plant leaf extract was mixed with 100 ml of 0.2 mM $AgNO_3$ solution (A25), 100 ml of 0.2mM $AgNO_3$ solution was mixed with 50 ml of leaf extract (A50), next 100 ml of plant leaf extract was mixed with100 ml of 0.2 mM $AgNO_3$ solution (A100), followed by adding 200 ml (A200) and 400 ml (A400) to the fixed volume of 0.2 mM $AgNO_3$ solutions with constant stirring at the temperature of 50 °C. The mixture has been incubated in dark chamber to minimize photo-activation of silver nitrate at room temperature until a colour change observed. Then, the solution was centrifuged for 15 min at 10000 rpm, the obtained Ag-NPs (Figure 4) was filtered by Whatman's No#1 and washed by deionized water and ethanol to remove impurities. Thereafter, the NPs was allowed to dry and ground so as to be used for further analysis (Ananda Murthy et al., 2020). The formation of the Ag NPs during the reduction process was indicated by change in the colour observed with different time interval: 0 min, 15 min, 30 min and 1h, respectively from colorless to dark brown within reaction duration. Another group of Ag NPs were prepared from fixed volume of plant leaf extract and $AgNO_3$ salt solution of different concentration: 5 mM , 2 mM, 1m M, 0.5 m M , 0.01m M and 0.001 mM $AgNO_3$.

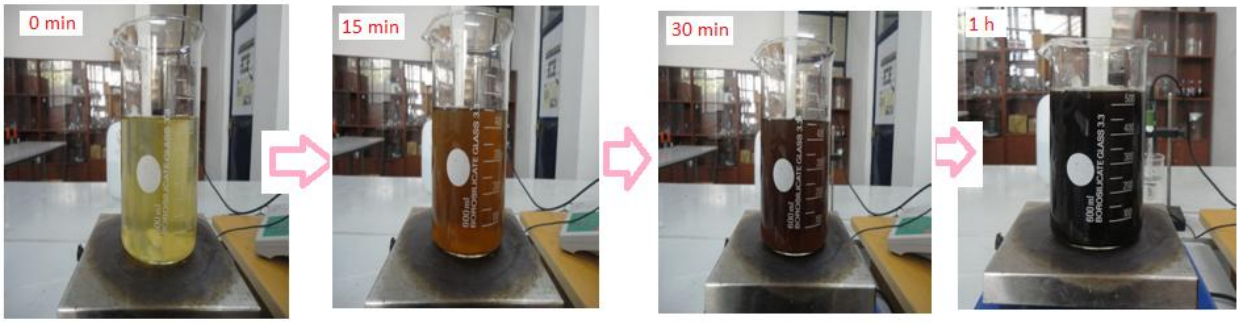

Figure 4: The colour observed during Ag NPs Synthesis with different time intervals

3.5.Synthesis of Zinc Oxide NPs

ZnO NPs were synthesized by a co-precipitation method by following the procedures used by (Upadhyaya et al., 2018). The volume ratio of the leaf extract to (0.2M) Zn (CH_3COO) $2.2H_2O$ aqueous solution were varied from 10 ml: 100 ml (1:10), 20 ml : 100 ml (1:5), 50 ml: 100 ml (1:2), 100 ml: 100 ml (1:1) and 200 ml : 100 ml (2:1). In a typical procedure, the leaf extract was added slowly to the precursor solution under continuous stirring at 60 °C for 2 hrs. The solution pH was adjusted to pH 12 by drop-wise addition of 1M NaOH. The formation of the ZnO NPs was indicated by a change in the colour of the solution. The obtained precipitate was centrifuged at 5,000 rpm for 10 min, washed with sufficient amounts of distilled water and ethanol, and collected in a ceramic crucible. The contents of the crucible were dried in an oven and ground with a mortar and pestle to obtain a fine powder. The obtained ZnO NPs were calcined at 500˚C for 2 hrs, cooled to room temperature, and packed in a plastic sample holder till required for characterization and application. For later discussion the ZnO NPs synthesized denoted as: Z10, Z20, Z50, Z100 and Z200 respectively.

3.6.Purification and Activation of Bentonite

3.6.1. Purification of Bentonite

Bentonite was dried at room temperature for one week and ball-milled using a planetary ball mill with a rotation of 350 rpm to a sieve particle size of 125 µm. To remove impurities such as quartz, carbonates, calcites, and iron hydroxide ($Fe(OH)_2$), 100 g of the sieved bentonite was dispersed in 1 L distilled water at room temperature and stirred for 1 hr. The suspension was allowed to stand for 24 hrs to settle the impurities. The supernatant was decanted and centrifuged at 3000 rpm for 20 min to obtain clean bentonite. This process was repeated four times, in order to ensure that the clay was in a pure form. The clay was dried in an oven at 105°C for 24 h, then again ball milled and sieved through a 63 µm mesh sieve, and stored in tightly closed plastic bottles till required for further experiments (Shah *et al*., 2013, Abdelhamid Elshater et al., 2018).

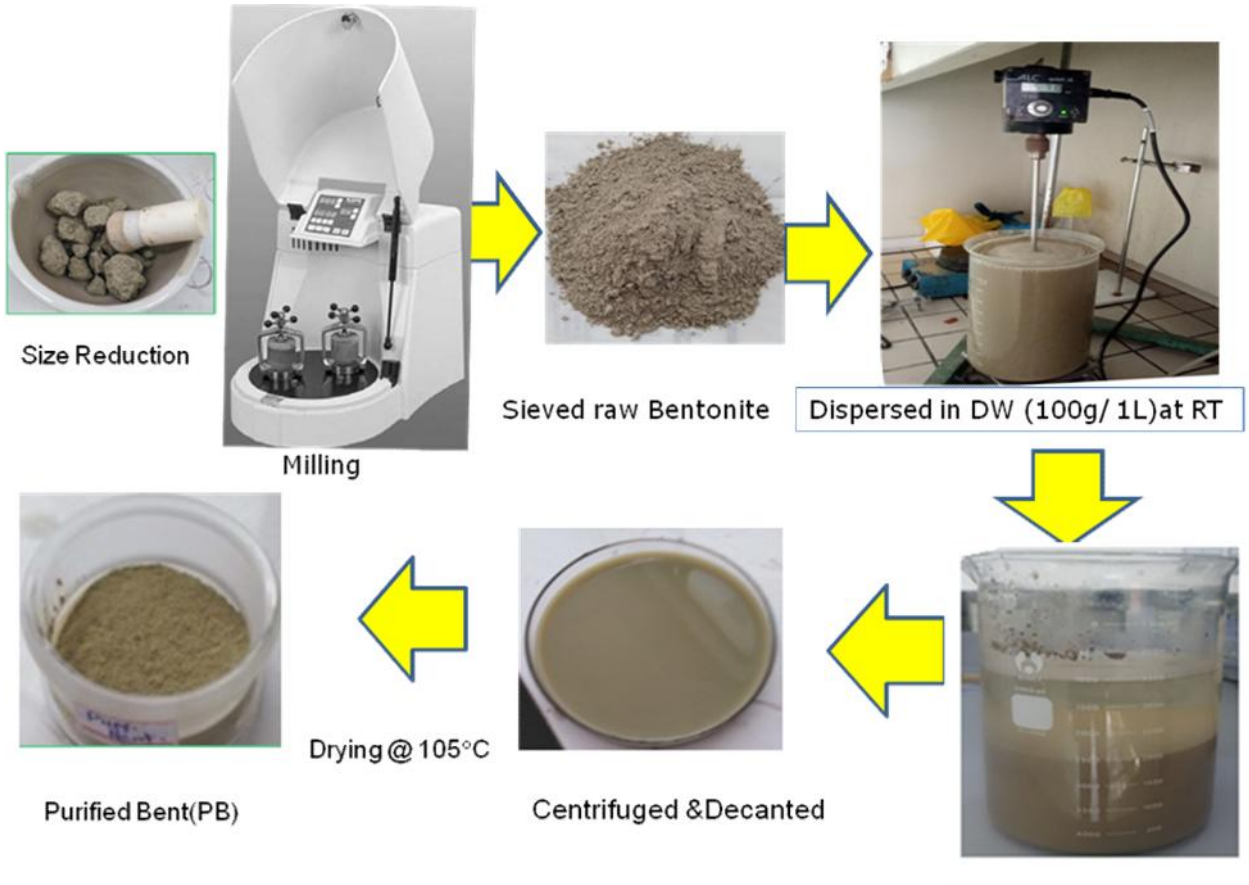

Figure 5a. Purification process of raw bentonite

3.6.2. Activation of bentonite by sodium carbonate

Activation of bentonite by sodium carbonate was conducted by using the procedure detailed by Shah*et al*. with slight modification (Shah *et al*., 2013, Abdelhamid Elshater et al., 2018). A 100 g of purified bentonite powder was dispersed into 1 L boiled distilled water to form a suspension. Then, different amounts (2.5 g, 5 g, 7.5 g, and 10g) Na_2CO_3 was added to the suspension to obtain a stable aqueous dispersion. The suspension was stirred slowly with a magnetic stirrer and boiled for 1h. After activation, the suspension was allowed to cool to room temperature and diluted with 1Ldistilled water. The diluted suspension was allowed to stand for 24 h to settle the impurities. The supernatant was decanted and the impurities settled at the bottom of the beaker were discarded. The bentonite suspension was centrifuged

at 3000 rpm for 20 min and then dried in an oven at 60 ˚C for 12 h to obtain Na-rich bentonite. The dried sample was then ground to obtain fine powder for further experiment.

Figure 5b. Activation of purified betonite with Na_2CO_3 and mechanical stirring

3.7. Synthesis of Zinc Oxide-Bentonite Nanocomposite

ZnO-bentonite NCs were synthesized by varying molar concentrations of $Zn(CH_3COO)_2.2H_2O$ and plant extract volume with fixed mass of activated bentonite adopting a previously reported procedures of (Kassem, 2015, Sasikala et al., 2019). But for this work we reported the results of ZnO-bentonite nanocomposites synthesized using 0.2 M concentration of 100 ml of $Zn(CH_3COO)_2 \cdot 2H_2O$ and 2.0 g of 5% Na_2CO_3 activated bentonite mixed in 1000 mL beakers with four different volumes aqueous extract of *H. abyssinica* volumes (50 ml, 100 ml, 200 ml and 300 ml) through dropwise addition and vigorous stirring for 30 min at room temperature. After 30 min, the mixtures were transferred to a heated oil bath, and stirring continued at 80 ˚C for a further 30 min at pH 12 adjusted by the addition of 1 M NaOH solution. Reddish-brown colour precipitates were formed and the contents of the beakers were centrifuged at 5000 rpm for 5 min followed by washing with distilled water

three times. The samples were then allowed to dry at room temperature for five days, followed by calcination at 650 ˚C for 2 hr and stored in amber-colour glass bottles till required. For subsequent discussion the ZnO/Bentonite nanocomposite synthesized denoted as: ZB50, ZB100, ZB200 and ZB300 respectively.

3.8. Synthesis of Ag-Bentonite Nanocomposite

The preparation of Ag-Bentonite composite were carried out as follow: in three different beakers with 100 ml distilled water about 2 g of activated Bentonite were added to prepare bentonite suspensions, and 100 ml solutions of 0.05M, 0.1M and 0.2M of $AgNO_3$ were separately added to the above three different beakers and stirred for 24 hrs at room temperature, followed by adding 100 ml leaf extract to each beaker respectively, to obtain coloured suspensions through vigorously stirring on magnetic stirrer for 1 hr at a temperature of 60^{o}C and denoted as AB005, AB01 and AB02. The suspensions of Ag/Bent NCs obtained were then centrifuged at 15,000 rpm for 5 minutes, and the precipitates washed 4 times using distilled water in order to remove the silver ion and other residues, ethanol & methanol to remove organic matters and dried overnight under vacuum (Shameli et al., 2011).

3.9. Characterization Techniques

3.9.1. Thermal analysis (TGA/DTA)

The thermal analyses of the synthesized samples were analyzed using thermal gravimetric analysis (TGA) and deferential thermal analysis (DTA). It was conducted to evaluate the thermal stability of ZnO NPs, bentonite nanoclay and ZnO-bentonite NCs by using a TGA (model DTA-60H, Shimadzu Co., Japan). 11.902 mg of ZnO NPs, 15.946 mg bentonite and 13.88 mg ZnO-bentonite NCs sample were analyzed under 50 [ºC/min] nitrogen flow rate with a heating rate of 10^{o}C in the temperature range of 23-1000^{o}C.

3.9.2. X-RAY Diffraction (XRD) (XRD-700 shimadzuco, South Korea)(

Crystalline structure and the average crystalline size of the synthesized ZnO NPs,Ag NPs, bentonite clay, Ag-Bentonite and ZnO-bentonite NCs were characterized using an X-ray diffractometer (XRD-700 shimadzuco, South Korea) equipped with a Cu target for

generating a Cu Kα radiation with λ = 1.54056 Å. XRD patterns were recorded from 10° to 80° for ZnO NPs and Ag NPs and 2° to 80° for bentonite, Ag-Bentonite and ZnO-bentonite NCs with 2θ angles using Cu Kα radiation operated at 40 kv and 30 mA in continuous scan mode with scan rate 3 (deg/min). The crystallite sizes (D) of the powders were calculated by using Scherrer's equation:

$$D = \frac{K\lambda}{\beta c \quad \theta} \quad \text{..... Eq. (1)}$$

Where K = 0.94 is Scherrer's constant, λ is the X-ray wavelength, θ is Bragg's diffraction angle, and β is the Full width at half maximum (FWHM) of the diffraction line at half of the maximum intensity.

3.9.3. UV-visible spectroscopy (UV–Vis)

The optical properties of the Ag NPs, ZnO NPs, bentonite clay, Ag NPs and ZnO-bentonite NCs were determined from absorbance obtained by (SM-1600 Dual beam UV-VIS Spectrometer, Azzota Corp., USA). The suspension was prepared from 0.01g samples powder in 15 mL de-ionized water to note the UV- Visible spectra. The absorbances of samples were recorded in the wavelength range: 200 nm to 800 nm and their maximum absorbance was recorded. Base line correction of the spectrophotometer was carried out by using a blank reference. The UV-Vis absorption spectra of the samples were recorded.

3.9.4. Bentonite composition Analysis

The purified bentonite and activated bentonite clay samples complete analysis were conducted for chemical composition. The determination **calcium and magnesium** were done by complexometric titration using Ethylenediaminetetracetate (EDTA) reagent as a complexing agent eriochrom Black T and calcon as indicators. Other reagents used were cyanide ions which form stable complex with interfering ions such as iron. Colorimetric method was used for the determination of total iron contents. Iron III was converted to iron II using hydroxylamine chloride solution. The Iron II react or complexed with 1,10-phenanthrolin to form an orange red complex at pH range 3-6. Flame emission photometry was used for sodium and potassium determination at 589.0nm and 766.5nm respectively. 1.0g of each sample was heated with a dry mixture of calcium carbonate (5.0g) and

ammonium chloride (0.5g) in a platinum crucible to convert sodium and potassium to soluble chlorides. The sintered mass was digested with hot water and the reactant calcium oxide and matrix elements- silicon, aluminum, iron, magnesium, beryllium, titanium etc that are retained in the precipitate in the form of insoluble oxide were removed by filtration. The resulting filtrate was analyzed for sodium and potassium. Interference from calcium error from the presence of small amounts of other alkali metals that may be present in the calcium carbonate and aluminum chloride used for sample decomposition was compensated for by adding identical liquors of a reagent blank solution to the calibration solution. Gravimetric method was used in the total silica determination. The samples were ignited to destroy organic matter. The residue was then taken up in hydrochloric acid.

1.0g of the finely ground dried (105-110°C) of each sample was weighed into a platinum crucible. The sample in the crucible was then ignited in a muffle furnace at 1030°C for 1 hour; allowed to cool and then weighed. The difference in weight before and after ignition represents the loss on ignition. Atomic absorption spectrophotometry at 364.2 mm was adapted in the determination of titanium. Phosphate was determined using Vanadomolybdo-phosphoric acid colorimetric method using ammonium molybdate which under acidic condition form molybdo-phosphoric acid. The intensity of the yellow colour was measured with spectrophotometer at 400- 490 nm (Ahmad and Birnin-Yauri, 2008).

3.9.5. Image analysis

Scanning electron microscopy with energy-dispersive x-ray spectroscopy (SEM-EDX-EVO18 model with low vacuum facility and ALTO1000Cryo attachment) and transmission electron microscope with high-resolution (JEOLJEM2100HRTEM) were used for understanding morphological and structural features of the synthesized nanoparticles and composites. Selected area electron diffraction (SAED) also performed to confirm the crystal structures. Particle size and SAED image was also computed by using imageJ and Microsoft paint software.

3.9.6. Fourier transforms infrared spectroscopy (FTIR) analysis

The functional groups present in dried powders of *H. abyssinica* crude extract, ZnO NPs, bentonite clay and ZnO-bentonite NCs were analysed by a FTIR (Perkin Elmer, Spectrum 65 FTIR, and USA). The spectra were acquired in the range 4000-400 cm^{-1}using KBr disc.

3.10. Antibacterial Test

The antibacterial activity of *H. abyssinica* leaf powder, Na Bentonite, Ag NPs, ZnO NPs, Ag/ Bentonite, and ZnO/Bentonite nanocomposite were investigated against Gram-negative bacteria *Escherichia coli (E. coli)* ATCC 25922 and Gram-positive bacteria *Staphylococcus aureus* (*S. aureus*) ATCC 25923 using disk diffusion and Broth dilution method in Adama Public Health Research and Referral Laboratory Centre (APHRRLC).

3.10.1. Disc Diffusion Methods

A). Media Preparation

Muller Hinton Agar and Sheep Blood Agar Media were prepared by dissolving, 38 g of Muller Hinton powder and 50 mL of Sheep Blood in1L of distilled water separately and then sterilized by autoclave at 121 °C and 15 pound pressure for 20 min. After cooling, about 20 mL of medium are added aseptically to sterilized Petri dishes. Then the Petri dishes were labelled and incubate until they solidify. The pH of the medium is generally maintained around the physiological pH of 7.4.

B). Bacterial cultures, Serial Dilution and inhibition zone testing of synthesised Samples

Bacterial cultures were maintained on Blood agar at 37 °C. Bacterial strains were taken from ATCC and grown aerobically on Blood Agar for 24 h at 37 °C and 0% CO_2. Bacterial suspension was prepared by taking it from blood agar and dissolving in sterile normal saline until the concentration of bacterial suspensions were achieved to1×10^8 colony forming units (CFU) mL^{-1} by comparison with the 0.5 McFarland Standard. 100 µL of 24 hr standardized culture of test bacteria was first evenly spread onto the surface of the Muller-Hinton agar plates using sterile cotton swabs. A sterile swab is used to inoculate the surface of the media in Petri dishes with making three rotations with an angle of 60° to ensure a homogeneous

growth. The plates were then turned upside down. 6 mm diameter of filter paper was prepared and placed in different areas of the disc. The antibiotic Contrimoxazole was used as the positive control and DMSO solvent was used as the negative control. 30 mg of each prepared samples were dissolved in 1 mL DMSO (30 mg mL^{-1}). From 30 mg mL^{-1} concentration of each sample, 15 mg mL^{-1}, 7.5 mg mL^{-1} and 3.5 mg mL^{-1} were diluted serially for Na-AB, ZnO NPs and ZnO/Bentonite NCS and 5 mg mL^{-1}, 2.5 mg mL^{-1} , and 1.25 mg mL^{-1} were serially diluted from10 mg mL^{-1} for Ag NPs, and Ag/Bentonite NCs. 6 mm diameter disc were saturated with 20 μL of each concentration and 25 μg of Contrimoxazole(positive control) and placed on a plate covered with lids and incubated at 37 °C and 0% CO_2 for 24 hr (Shao et al., 2015). The diameter was measured from the area around the disc where no bacterial growth has been observed, called the inhibition zone. All antibacterial tests were carried out in triplicate and the averages were reported. This diameter can be compared to the critical diameters of antibiotics Contrimoxazole and digital images were captured (Dadi et al., 2019).

3.10.2. Determination of the Minimum Inhibitory Concentration (MIC) and Minimum Bactericidal Concentration (MBC)

Ag/Bentonite and ZnO/Bentonite nanocomposites were tested for bactericidal effect using both the microbial culture selected for the study by following the procedure used by (Gupta & Kumar, 2018). The lowest concentration of material that inhibits the growth of an organism was defined as the minimum inhibitory concentration (MIC). The serial dilution method was employed to determine the MIC of the composites. Each of the 10 test tubes was filled with 2 mL of the liquid Muller Hinton Agar medium. In the test tubes number 1, 2 mL solution containing 20 $mgmL^{-1}$ of nanocomposite that had been sonicated at room temperature was added and mixed thoroughly with the culture medium. The concentration of nanocomposites in test tube 1 becomes 10 $mgmL^{-1}$. Then, 2 ml of the content of test tube number 1 was added to test tube number 2 and mixed completely. This process was performed serially to test tube number 11. Consequently, 2 ml content of test tube number 11 was discarded. Finally, 0.2 mL of standard microbial suspensions *Escherichia coli* (ATCC 25922) and *Staphylococcus aureus* (ATCC 25923) containing 1×10^8 $CFUmL^{-1}$ microorganism were added to test tubes number 1 to 10, and the test tubes were incubated at

35 °C for 24 hr. Then, the microbial growth was studied by turbidity observation. The experiments also included a positive control (test tube containing nanoparticles and Muller Hinton Agar medium, devoid of inoculum) and a negative control (test tube containing inoculum and Muller Hinton Agar medium, devoid of nanocomposites). The negative controls indicated the microbial growth profile in the absence of nanocomposites. All the experiments were carried out in triplicate. The minimum bactericidal concentration (MBC), i.e., the lowest concentration of nanoparticles that kills 99.9% of the bacteria was also determined from the batch culture studies. For growth inhibitory concentration (MIC) the presence of viable microorganisms was tested and the lowest concentration causing bactericidal effect was reported as MBC (Chikezie, 2017). To experiments for bactericidal effect, from each test tube (Specially, negative and positive test tubes) was inoculated on Muller Hinton Agar and incubated at 35 °C for 24 hrs. The nanoparticles concentration illustrating bactericidal effect was picked out based on absence of colonies on the agar plate.

4. RESULTS AND DISCUSSION

4.1. Phytochemical screening of the plant leaf extract

The phytochemical analysis result *of H. abyssinica* plant leaf extract is presented in the table 1. The aqueous leaf extract analysis demonstrates that *Hagenia abyssinica* is a good source of various phytochemicals such as saponins, flavonoids, phenols, terpenoids, alkaloids, and tannins which serve the roles of reducing and capping agent to inhibit the growth of nanoparticles and prevent agglomeration of the particles. From the preceding report this plant is a medicinal plant that contains large number of bioactive compounds (Wolde et al., 2016).

Table 1: The phytochemical screening results of *H. abyssinica* plant leaf aqueous extracts.

No	Test	Phytoconstituents	Observation	Result
1	Wagner's reagent	Alkaloids	A reddish-brown precipitate	+
2	Benedict's reagent	Reducing sugars	Yellow colour	+
3	Alkaline reagent test	Flavonoids	An intense yellow colour, becomes colourless on addition of diluted acid	+
4	Ferric chloride test	Phenols	Bluish black colour	+
5	Braymer's test	Tannins	Blue-green colour	+
6	HCl test	Phlobatannins	A red colour	-
7	Salkowski test	Terpenoids	A grey coloured solution	+
8	Frothing test	Saponins	The formation of stable persistent froth	+

(+) indicates the presence of phytochemical constituents (-) the absence of phytochemical constituents.

4.2. Compositional Analysis of Bentonite

Table 2 shows the major elemental analysis of pure and sodium activated bentonite samples. The compositions of activated bentonite with Na_2CO_3 to exchange Ca^{2+} ions with Na^+ ions, where the percentage of Na_2O increased from1.41 % to 4.89 % with 5% of Na_2CO_3, but the CaO content decreased from 3.15% to 1.02%, indicating that Ca^{2+} has been replaced by Na^+ in MMT. Hence, Na^+ bentonite clay is one of the preferred layered materials for the preparation of nanocomposites because of its high cation exchange capacity, high surface

area, strong adsorption capacities within their inter-lamellar spaces and swelling capacity (Unnithan, 2017, Shah et al., 2013).

The increase percentage of H_2O, also enhanced the swelling capacity of Na-bentonite due to the presence of more Na+ in between the Octahedral and Tetrahedral layer, and water could hydrate in the clay mineral due to weak electrostatic interaction between the sodium ion and the negatively charged bentonite layer, allowing excess water molecules to enter. Smaller ions tend to have greater hydration energies, and thus within the interlayer of clays can attract more water than large ions (Bazbouz and Stephen, 2018, Unnithan, 2017, Shah et al., 2013). The decrease of SiO_2 and Al_2O_3 percentages after activation with Na_2CO_3, confirmed the removal of minor amount of quartz as an impurity and followed by sedimentation. In contrast the MgO content decreased ~ 3%. The percentage of Fe_2O_3 and K_2O also decreasedduring the activation process as impurities. The source of K_2O in the clay mineral may be from illite or feldspar.

Table 2: Chemical analysis of bentonite before and after sodium activation

Oxides %	SiO_2	Al_2O_3	Fe_2O_3	CaO	MgO	Na_2O	K_2O	P_2O_5	TiO_2	H_2O	LOI
PB	55.50	12.64	7.70	3.10	2.49	1.38	0.97	0.63	0.35	4.38	10.89
5%Na-B	55.15	12.50	6.86	1.02	2.20	4.89	0.94	0.55	0.36	6.31	9.22

*PB: purified bentonite, *5%Na-B: 5% Na_2CO_3 activated Bentonite

4.3. Analysis of XRD Result

4.3.1. XRD Analysis of Bentonite

XRD patterns of raw bentonite, purified bentonite (PB) and Sodium-activated bentonite (Na-AB) samples are displayed in Figure 6. Figure 6a shows montmorillonite (MMT) reflections at the 2θ positions of 6.20 (raw), 6.24 (PB,), 6.9 (Na-AB); 19.8 (raw), 19.8 (PB), 19.34 (raw); 34.45 (PB), 34.60 (Na-AB), and 61.35 (raw), 61.55 (PB), 61.74 (for Na-AB) and so on. According to the crystal data sheet JCPDS 02–0037, the 2θ correspond to basal reflections of d(001), d(003), d(100), d(104), and d(061), respectively, which is in agreement with the earlier report (Colín-Luna et al., 2018). The d_{001} diffractions of the main

montmorillonite (MMT) component of raw, PB and Na-AB for 2θ ~ 6° are with the basal distances of ~14 (for raw and PB), 12.8 (for 5% Na-AB) respectively and the other d values of MMT are presented in Table 3. The peaks originating from the other clay components like kaolinite (in raw bentonite) observed at 15.80°, dolomite (D) and quartz (Q) are observed at 26.4 and 29.4° with the d_{400} and d_{330} values of 3.37 and 3.04 Å, respectively. From the intensities of the d_{001} peaks of raw, PB, (Na-AB) and the diffractions of the non clay components comparison, it may be concluded that the main component of bentonite is montmorillonite and the quartz and dolomite fractions in all samples are small, which agree with other report (Caglar et al., 2009). The powder diffraction patterns before the activation of the bentonite revealed that this bentonite is in the family of smectite having similar reflection from (001) plan with inter-planar distances (d_{001}) value of greater than 14 Å. This shows that the natural (raw) bentonite is in calcium form (El Miz et al., 2017). The higher d_{001} values of raw and PB (~14 Å) than that of Na_2CO_3 activated bentonite (Na-montmorillonite) may be explained as the raw and PB were calcium-rich bentonite (Caglar et al., 2009). The Na-montmorillonite obtained by soda activation at 5 g Na_2CO_3/100 g bentonite has a lower d_{001} spacing (~12.8 A˚) than the original Ca-montmorillonite (~14 A˚) (Table 3), suggesting that the Na^+ ions replaced Ca^{2+} ions in the montmorillonite. This finding agreed with early report(Shah et al., 2013). So, comparative XRD pattern of PB and of sodium exchanged bentonite actually confirms a good exchange of calcium by sodium by comparison of the lines with the (001) peak. The shift in the basal space of the (001) plan from 14.1Å to 12.8 Å (Figure 6a), shows that the exchange between calcium and sodium was well take place. In the conventional methods of bentonite activation with soda, the calcium ions expelled from the interlayer have been reported to precipitate as $CaCO_3$. Directly after activation the dominant reflection maximally corresponds to d_{001} ~ 14.1 Å, with a shoulder ~ 13.2 Å, with 2.5 g of Na_2CO_3 addition in 100 g of purified bentonite indicating that some exchange of calcium cations with Na^+ occurred, the interlayer of montmorillonite is still occupied mainly with Ca^{2+}. Additionally, 5 %, 7.5 % and 10 % of Na_2CO_3 addition to the purified bentonite changed the d_{001} interplanar space to 12.8, 12.9 and 12.7 Å respectively. The gradual transformation of Ca-montmorillonite into Na-rich form proves that cation exchange of Ca^{2+} with Na^+ continues and become constant above 5%. At the same time the

2θ values of diffraction also shifted toward the right from 6.24 to 6.92 as the conversion of Ca-bentonite to Na-bentonite increases due to water of hydration. A broad, low-intensity peak corresponding crystalline calcite formed by the activation associated with precipitation of $CaCO_3$ was not observed on the XRD pattern, this might achieved during the purification of the activated bentonite. The mineralogical pattern of the natural bentonite is shown in Fig. 1 and significant amounts of quartz, dolomite and kaolinite are presented in the mineral. This result showed that the clay is highly heterogeneous, so the pre-treatments are mandatory in order to reduce the content of non-clay minerals that negatively interfere on the bentonite properties (Ye et al., 2016). The XRD patterns in Fig 6b, show the d_{001} reflections values changes with activation of bentonite by Na_2CO_3 at 2 theta value or d-values which is a typical characteristic peak of natural sodium bentonite clay, revealing that the predominant exchangeable cation could be sodium, as suggested by AAS analysis (see Table 3).

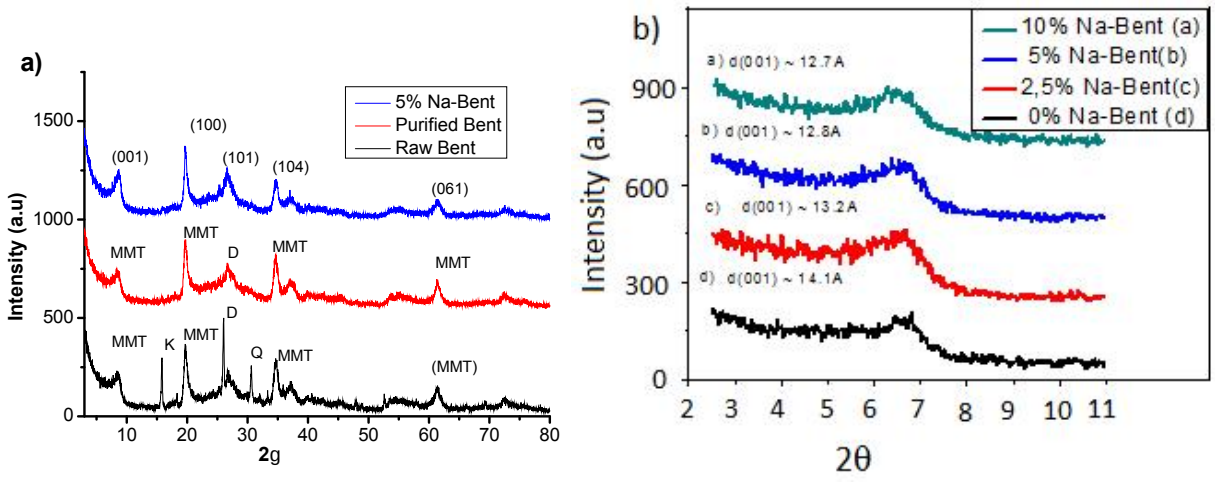

Figure 6: XRD Patterns of a) raw, Purified Bentonite and 5%Na-Bentonite and b) 10%, 5%,2.5% Na-Bent and Purified Bentonite . Where, MMT: Montmorillonite, D: Dolomite, K: Kaolinite and Q: quartz.

Table 3: The interplanar spacing, and phases of raw, PB and Na-AB bentonite samples

Raw Bentonite (RB)				Purified Bentonite (PB)				5% Na-AB			
2θ (°)	(hkl)	d-space (Å)	Phase	2θ (°)	(hkl)	d-space (Å)	phase	2θ (°)	(hkl)	d-space(Å)	phase
6.20	(001)	14.13480	MMT	6.24	(001)	14.14281	MMT	6.9	(001)	12.80047	MMT
15.8	(003)	5.569418	K	19.8	(100)	4.480335	MMT	19.8	(100)	4.480335	MMT
19.8	(100)	4.480335	MMT	26.4	(400)	3.373318	D	26.4	(400)	3.373318	D
26.4	(400)	3.373318	D	29.4	(330)	3.03557	Q	29.4	(330)	3.03557	Q
29.4	(330)	3.03557	Q	34.5	(105)	2.597612	MMT	34.5	(105)	2.597612	MMT
34.83	(105)	2.597512	MMT	61.4	(300)	1.508786	MMT	61.7	(300)	1.502168	MMT
61.5	(300)	1.508886	MMT								

4.3.2. XRD Results of ZnO NPs

Figure 7 shows the XRD pattern of the ZnO NPs synthesized by using various ratios (1:10, 1:5, 1: 2, 1:1 and 2:1) of plant leaf extracts to zinc acetate. The XRD pattern of nanostructure of ZnO shows that the diffraction peaks at around the angles 31.82^{o}, 34.46 ^{o}, 36.3 ^{o}, 47.62 ^{o}, 56.64 ^{o}, 62.9^{o}, 68^{o} and 69.18^{o} which corresponds to the crystal planes of (100), (002), (101), (102), (110), (103), (112) and (201) in the wurtzite structure showed similarity to that obtained by Salam *et al*., using *Ocimum basilicum L.var. purpurascens* extract (Salam et al. 2014). All the peaks observed were related with the hexagonal phase (wurtzite structure) in comparison with the data from JCPDS card No. 36-1451. The average crystallites sizes of Z200, Z100, Z50, Z20 and Z10 were found to be 13.5 nm, 18.1 nm, 21.7 nm, 23.3 nm and 28.7 nm which were derived from the FWHM of more intense peaks corresponding to (100), (102) and (101) using Scherrer's formula. The difference in diffraction angles and peaks width could be due to the effect of the volume of plant extract used for the synthesis of ZnO NPs. This result confirms the concentration effect of capping agent in the leaf extract on crystallites sizes of the zinc oxide crystals synthesized.

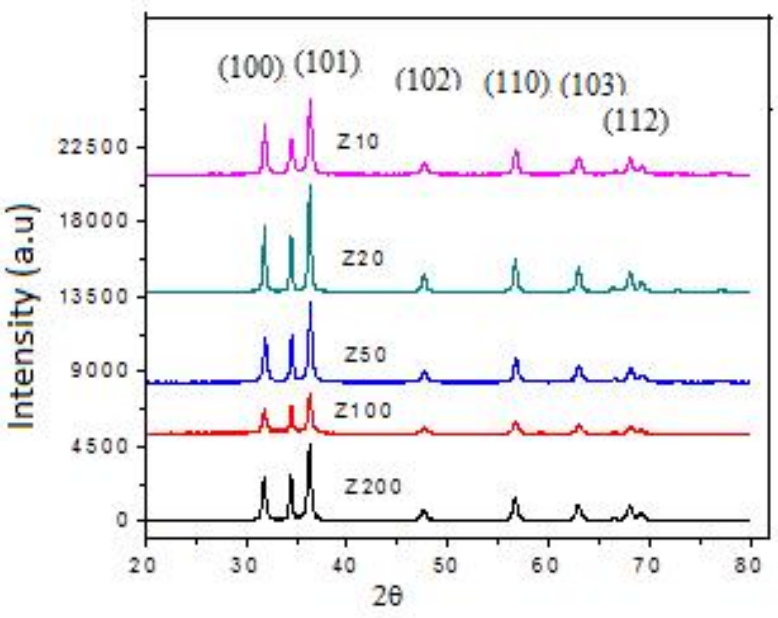

Figure 7. XRD patterns of ZnO NPs synthesized using different volumes of plant leaf extract

4.3.3. XRD analysis of ZnO-bentonite NCs

Figure 8 depicted the XRD patterns of mixed phases; activated bentonite with the diffraction peaks located at 2θ¼ 19.8, 26.6^{o}, 34.5^{o} corresponding to (100), (400), and (105) planes due to the silicate units and ZnO NPs characteristics peaks are also observed at 2θ~ 31.8 ^{o}, 34.4 ^{o}, 36.2 ^{o}, which corresponds to (100), (002), and (101) planes and bentonite characteristics peaks are also again observed at 2θ~ 8.8°, that indicated the composite are composed of ZnO and benonite phases**.** As indicated in the table 2, the average crystallites sizes of the composite particles are slightly affected by volume of the extracts used during the synthesis (table 4)**.**

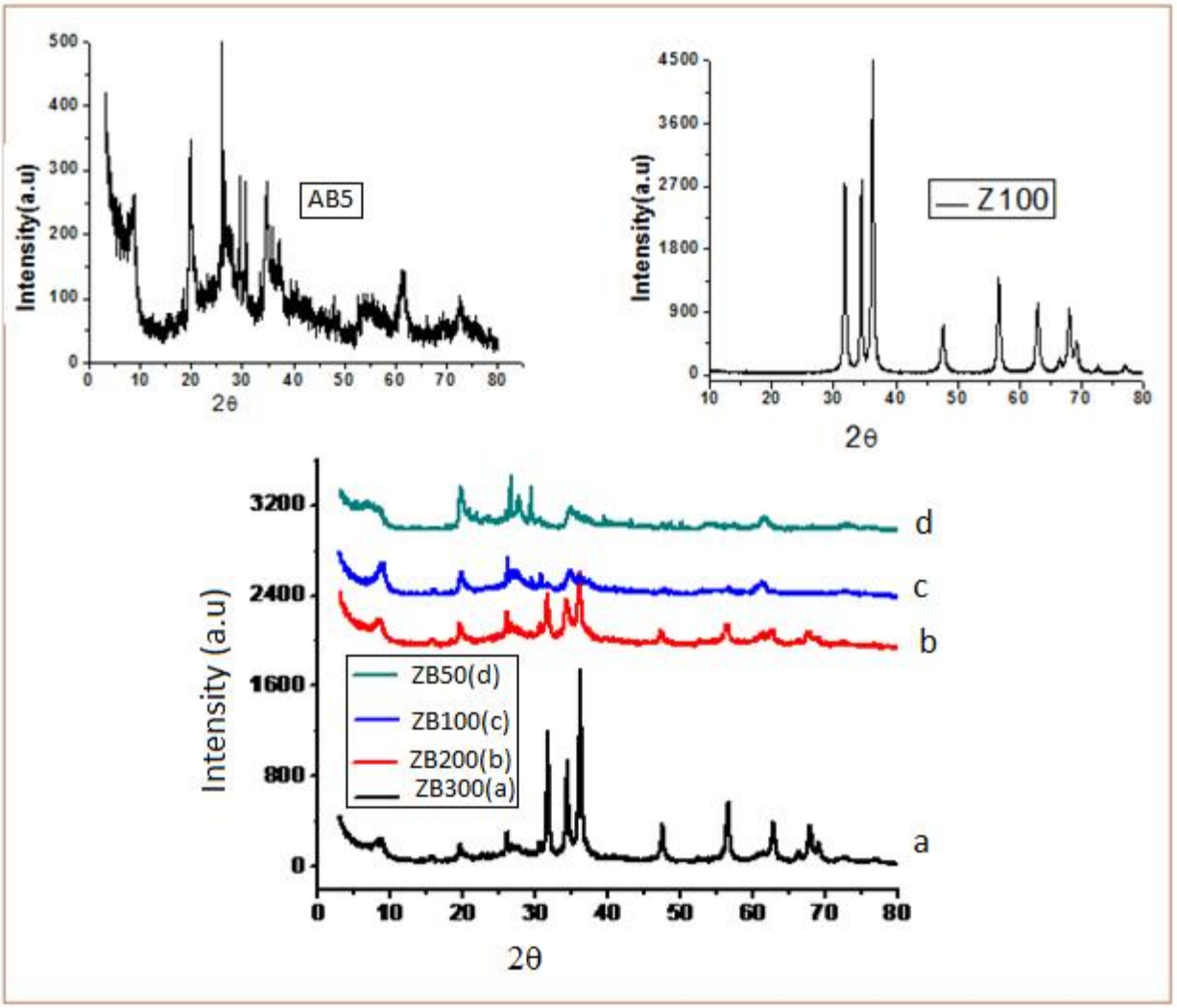

Figure 8: XRD analysis result of activated bentonite(AB5), ZnO (Z100), ZnO-bentonite NCs: ZB300(a), ZB200 (b), ZB100 (c) (and ZB50) (d).

Table 4**:** Average crystallites size and inter-planar d-spacing for the major peaks of ZnO-bentonite NCs

Composite	Peak 2θ	sin θ	d(Å)	cos θ	β(rad)	D(nm)
ZB300	31.8	0.274	2.8120	0.5662	0.0098	13.51
	34.4	0.296	2.6004	0.5436	0.0094	13.89
	36.3	0.312	2.4743	0.5816	0.0101	12.45
Na-AB	19.7	0.171	4.48853	0.985	0.01187	11.86
	26.7	0.231	3.33387	0.973	0.02967	4.80
	34.5	0.297	2.59565	0.955	0.01203	12.07
Average particles size						11.32nm
ZB200	31.8791	0.273	2.82219	0.96203	0.009080	15.87
	34.4242	0.296	2.60316	0.95522	0.013926	10.42
	36.1225	0.31	2.48457	0.95073	0.010315	14.14
Na-AB	19.8	0.172	4.47423	0.985	0.0117	12.03
	26.6	0.23	3.30538	0.973	0.0169	8.43
	34.5	0.297	2.60046	0.955	0.0095	15.28
Average particles size						12.70
ZB100	31.8	0.274	2.81077	0.962	0.01065	13.54
	34.5	0.297	2.59565	0.955	0.01203	12.07
	36.3	0.312	2.46968	0.951	0.01357	10.75
Na-AB	19.78	0.172	4.48291	0.985	0.0103	13.66
	27.8	0.24	3.20469	0.971	0.0066	21.64
	34.6	0.297	2.58612	0.955	0.01117	13.00
Average particles size						14.11 nm

ZB50	31.7564	0.274	2.81549	0.96185	0.006301	22.88
	34.4236	0.296	2.60320	0.95522	0.006899	21.04
	36.2352	0.311	2.47710	0.95042	0.006582	22.16
Na-AB	8.8784	0.077	9.95205	0.997	0.020771	6.70
	26.2289	0.227	3.39493	0.97392	0.011304	12.59
	34.9554	0.30	2.56481	0.95383	0.022416	6.49
Average particles size						15.31 nm

4.4. Scanning Electron Microscopy(SEM) Analysis

4.4.1. SEM Analysis of Bentonite

Figure 9a & b shows the SEM image of the as-received and purified bentonite powders. The raw clay presented large particles in blocks, which is consistent with the presence of minerals, which acted as a binder in the formation of agglomerates. After treatment, agglomerates had a more fragmented particles, less homogeneous, with more channels, contact areas, and smaller particles, which are more favourable for material exchange. Thus, the treated samples were chosen as precursors for sodium activation and composite preparations. The EDX analysis of the raw bentonite confirmed the elemental analysis reports.

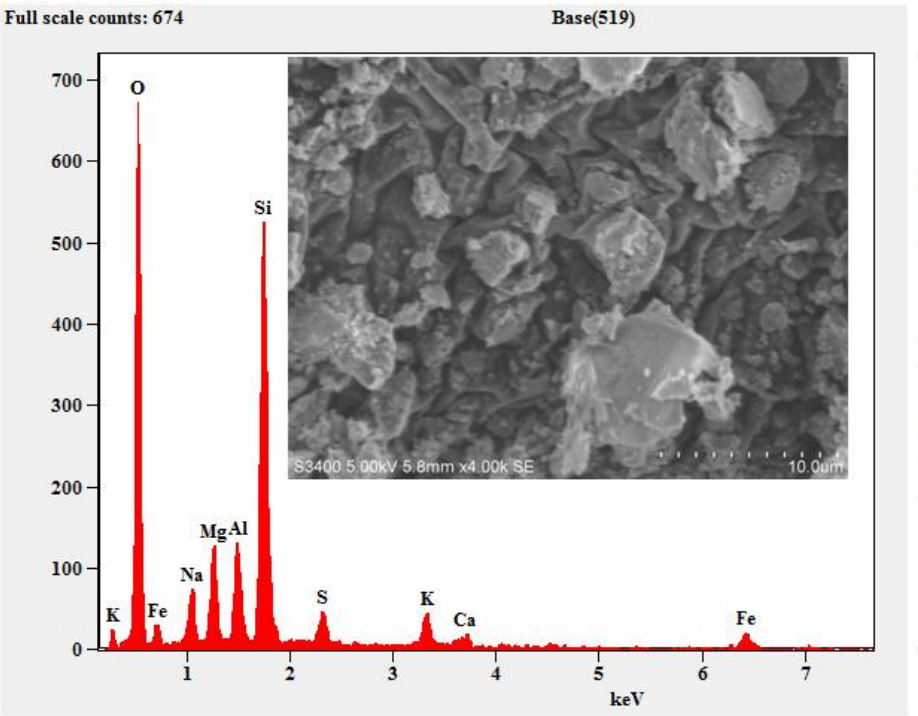

Element Line	Weight %	Weight % Error	Atom %
O K	55.58	± 1.01	69.53
Na K	5.23	± 0.55	4.55
Mg K	4.12	± 0.43	3.39
Al K	3.90	± 0.47	2.89
Si K	20.74	± 0.50	14.78
S K	2.07	± 0.27	1.29
K K	2.40	± 0.28	1.23
Ca K	1.36	± 0.15	0.68
Fe K	4.60	± 0.45	1.65
Total	100.00		100.00

Figure 9a: The SEM image and EDX spectrum of bentonite before purifcation

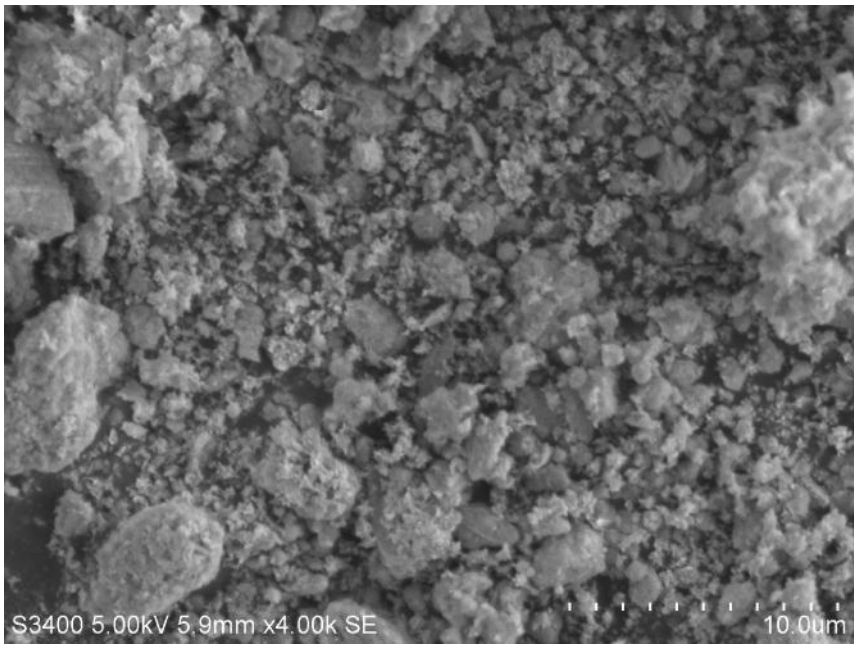

Figure 9 b: The SEM image of purified bentonite

4.4.2. SEM Analysis of ZnO & ZnO/Bentonite

The morphologies of ZnO NPs and ZnO- bentonite nanocomposite were investigated using SEM. Figure 10a depicted the SEM image with EDX spectrum which demonstrates the presence of unevenly sized and agglomerated particles. After loading ZnO (Figure 10b), the morphology of the composite was still similar with that of ZnO NPs, but they are looser and the surface was rougher. From literatures very few of the ZnO NPs may enter the interlayer of bentonite, while the majority of the ZnO NPs were impregnated onto the surface of bentonite, which is confirmed by the XRD phase analysis (Mustapha et al., 2020, Xu et al. 2015, Meshram et al., 2011).

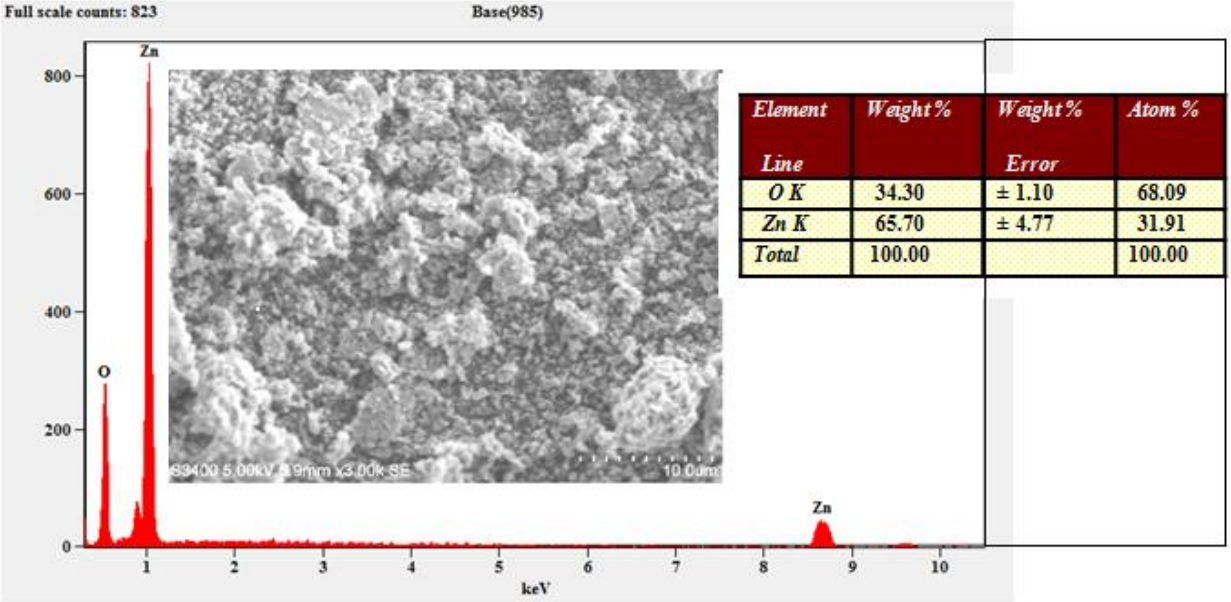

Element Line	Weight %	Weight % Error	Atom %
O K	34.30	± 1.10	68.09
Zn K	65.70	± 4.77	31.91
Total	100.00		100.00

Figure 10 a: SEM micrograph and EDX of ZnO NPs (Z100) annealed at 650°C

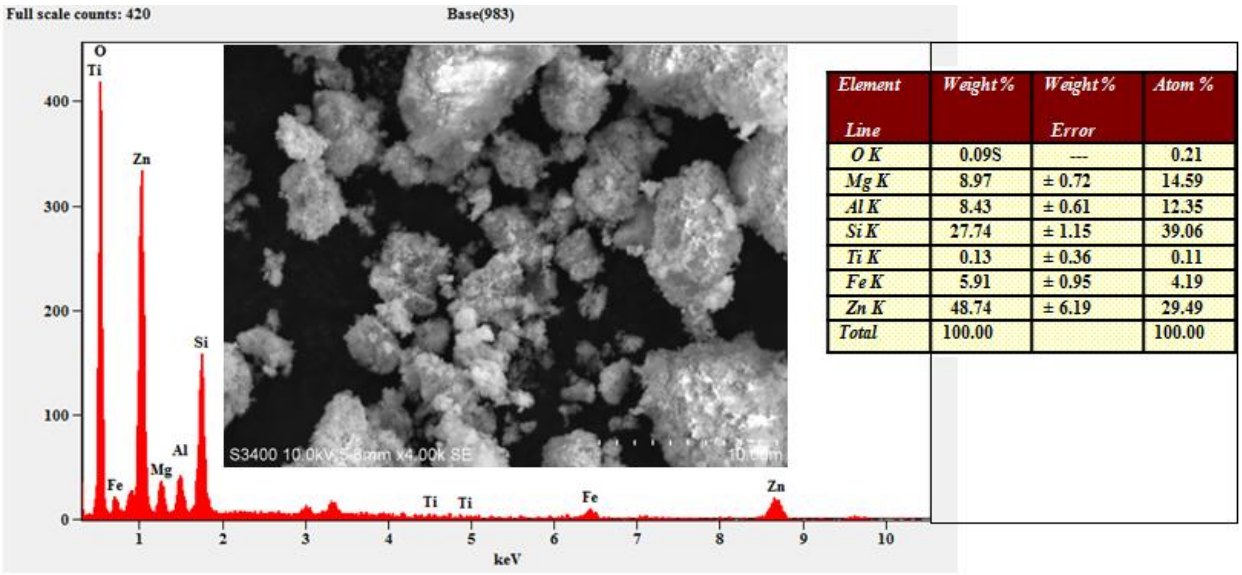

Element Line	Weight %	Weight % Error	Atom %
O K	0.09S	---	0.21
Mg K	8.97	± 0.72	14.59
Al K	8.43	± 0.61	12.35
Si K	27.74	± 1.15	39.06
Ti K	0.13	± 0.36	0.11
Fe K	5.91	± 0.95	4.19
Zn K	48.74	± 6.19	29.49
Total	100.00		100.00

Figure 10b: SEM Images and EDX of ZnO/Bentonite (ZB100) calcined at 650°C.

4.5. Characterization by UV-Vis spectroscopy

4.5.1. UV-Vis spectra of ZnO NPs

The UV/Vis experiments were performed in order to examine the optical characteristics of ZnO NPs. The UV-Vis spectra recorded the maximum absorbance peak in the range of 371-382 nm (Figure 11), which established the formation of ZnO NPs from different volumes of leaf extract, and consistent with earlier studies conducted by (Senthil kumar et al., 2017). Similar results were also reported earlier by (Nethravathi et al., 2015, Jamdagni et al., 2018, Jamdagni et al., 2018). Additionally, there are no other peaks observed in the spectrum as an impurity. Furthermore, the high absorption band seen for different ratios might be attributed to ZnO's inherent band-gap absorption caused by electron transitions from the valence band (VB) to the conduction band (CB) (O2p–Zn3d) (Awwad et al., 2014, Zak et al., 2014). In earlier studies, other groups reported absorbance peaks at 377 nm and 375 nm respectively for ZnO NPs (Zak et al., 2012, Akbar et al., 2021).

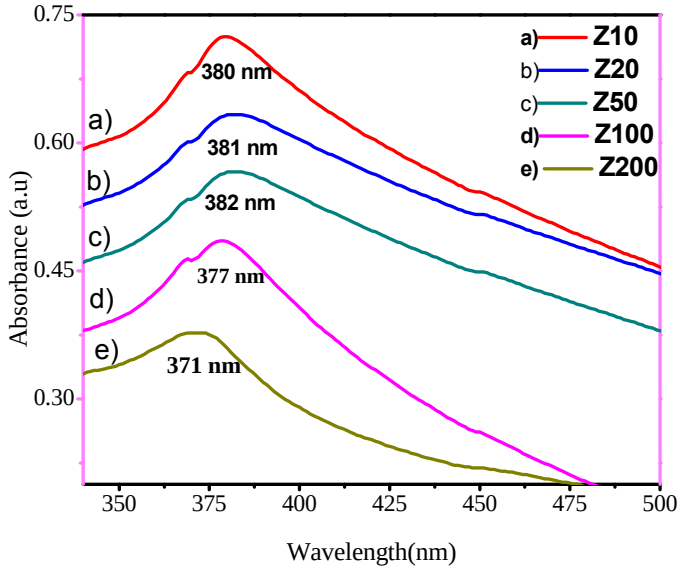

Figure 11: UV-Vis absorption spectra of ZnO NPs synthesized by different ratios of plant extract to zinc acetate solution.

4.5.2. UV-Vis Absorption Spectra of ZnO-bentonite NCs

The absorption property of ZnO/Bentonite is a key factor that determined the optical property of the composites. The nanocomposites synthesized for this work has absorption peaks in the range of 273-285 nm, and weak absorption peak is located near 385 nm (Figure 12). The results revealed the influence of leaf extract volumes in the optical properties of the composite materials. The maximum absorption peak located around 273 nm is slightly blue shifted to lower wavelengths because of the usage of more extract volume for the synthesis of the composite. This blue shift and enhanced absorbance is an indicator for the absence of agglomerations in the composite crystals (Ghorbanpour and Falamaki, 2013). The UV-graphs show a large change (85%) in the absorption with volume of extract changes (ZB30 to ZB200). This qualified the changes in the number of ZnO NPs impregnated on the surface of bentonite clay with the change of the volume of leaf extract. The additional band observed like that of ZB50 at 380 nm on absorption spectra can be assigned to Zn-O chromophoric groups (Agarwal et al., 2019). Thus, in contrast to the visible, the composite materials are strongly absorbing in the UV region. So, the result could be attributed to high absorbance of ZnO. These results show the strong interaction between the bentonite and the zinc oxide nanoparticles. In addition, there are no absorption bands in the visible

region for all samples under investigation, because the composites are transparent. The optical absorption of the nano nanocomposite in the UV region is quite high and this aspect highlights the prospects or applications of these composites in UV shielding. A shift in the absorption peaks from UV-B to UV-A region was observed, in the ZnO/Bentonite nanocomposite developed for this project.

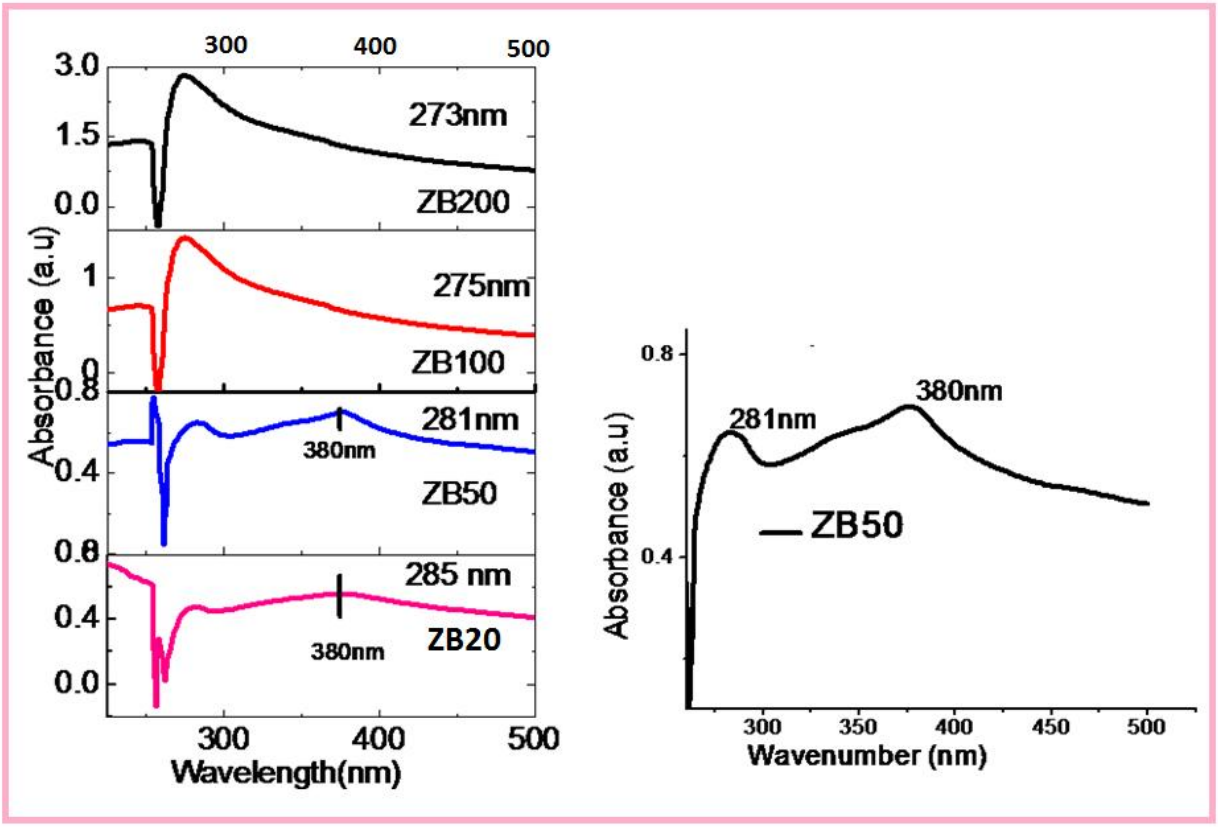

Figure 12: UV-Vis absorbance spectra of ZnO-bentonite NCs

4.5.3. UV-Vis Diffuse Reflectance Spectroscopy of ZnO/Bentonite

Ultraviolet-visible diffuse reflectance spectroscopy (DRS) is a common method to characterize the optical absorption properties of materials. As displayed in Figure 13, the pristine ZnO synthesized with different ratios of leaf extract shows a strong absorption in ultraviolet region or UV-A (371-382 nm), which is consistent with the light absorption characteristics of ZnO. Selected samples of ZnO/Bentonite prepared with different ratios of leaf extract showed absorption in the range of UV-B (273-285nm). The blue shift absorption spectra were observed in the ZnO/Bentonite with respect to all as synthesized ZnO. According to the Kubelka-Munk function, the band gap energies can be calculated from the plots of $(\alpha hv)^2$ versus photon energy and extrapolating the linear part of the graph until it meets the x-axis which

will give the value of the band gap (Zhang et al., 2011, Aadnan et al., 2020). The band gap energies of pristine ZnO, Activated Bentonite (AB), composite of ZnO/Bentonite prepared with different volumes of plant extracts (ZB100, ZB200 and ZB300) are 3.24 eV, 3.73 eV, 3.23 eV, 3.15 eV and 3.07 eV, respectively (Figure 10 a, b, c, d and e). The obtained Eg value of ZnO (3.24 eV) indicates ZnO cannot absorb wavelengths above 400 nm, whereas that of ZnO-Bentonite with leaf extracts to Zn^{2+} volume ratios of (1:1/AB100, 1:2/AB200 and 1:3/AB300) nano-composite are not sensitive to visible light. The band gap values are estimated to be varying between 3.15 eV and 3.07 eV and it is also observed that band gaps are found to deceases with making composite of bentonite with ZnO NPs (Ajith1 et al., 2021), decrease with combination of composite with the increase in extracts volume.

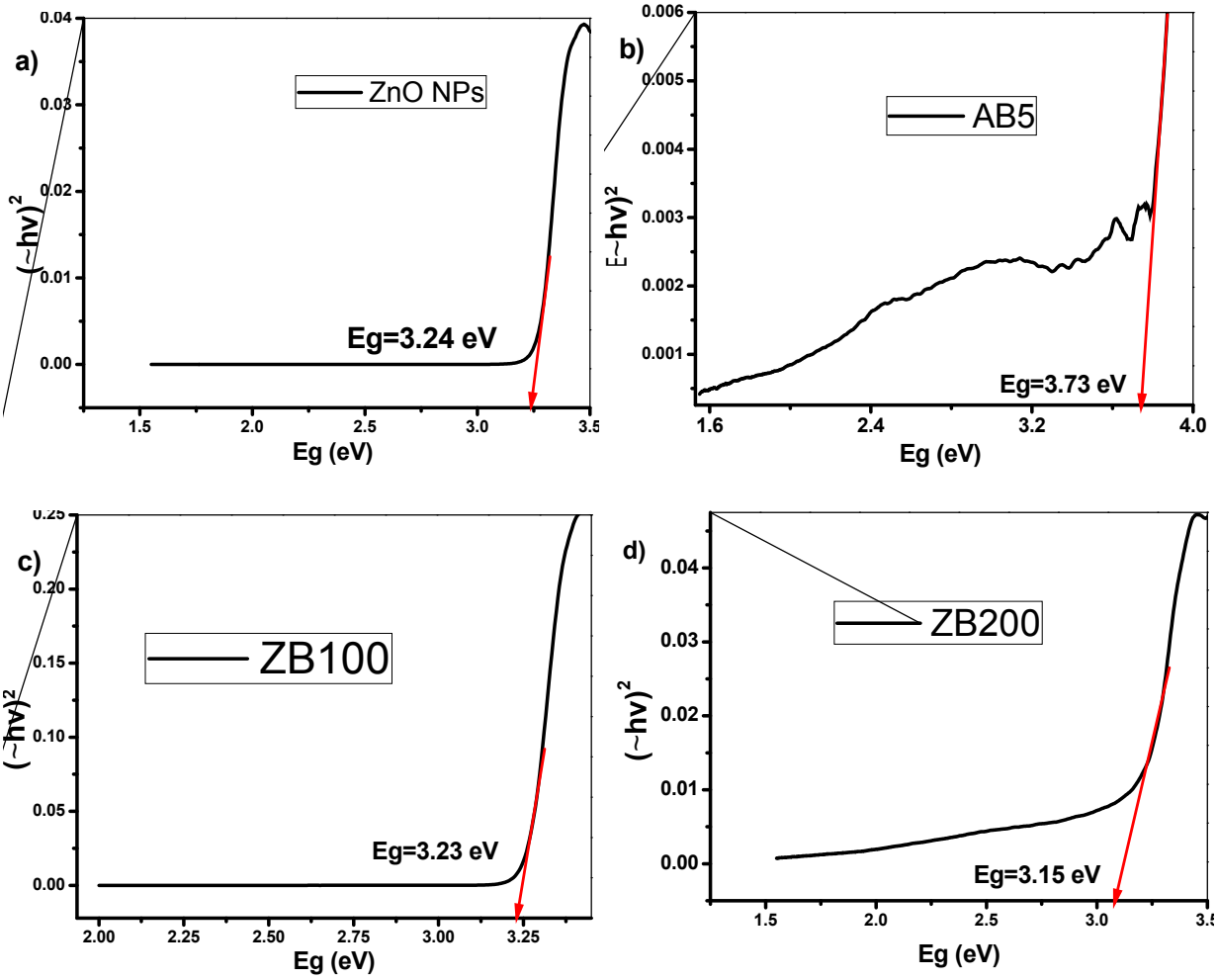

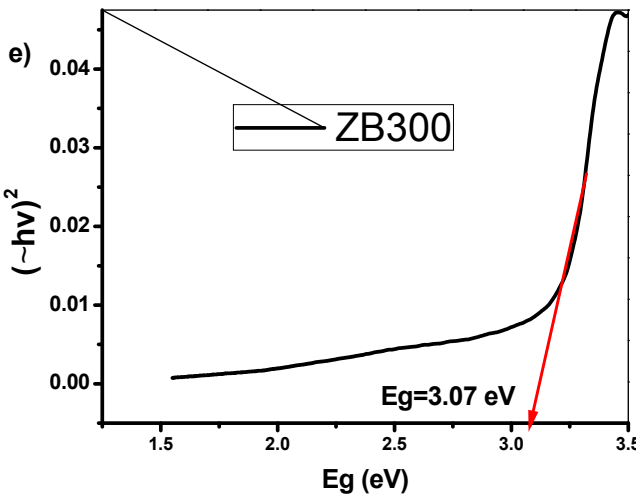

Figure 13. The band gap energies of pristine ZnO (a), Activated Bentonite-AB (b), and composite of ZnO/Bentonite prepared with different volumes of plant extracts ZB100 (c), ZB200 (d) and ZB300 (e).

4.6. Thermal Analysis (TGA/DTA)

This technique is used to investigate the thermal decomposition and stability of samples. The as synthesized ZnO NPs, bentonite clay and ZnO-bentonite NCs thermal analysis were conducted from room temperature to 1000˚C at the heating rate of 10 ˚C/ min. TGA curve shows the mass loss of the sample, whereas the DTA curve indicates the energy gain or loss during the process.

4.6.1. Thermal analysis of ZnO NPs

The thermo-gravimetric analysis (TGA) curves (Figure 14a) revealed the weight loss in three main temperatures ranges for ZnO, (30 °C–110 °C), (210 °C–420 °C) and (420 °C–500 °C). In the latter specimens, the mass loss ends at about 500 °C which is due to the decomposition of $Zn(OH)_2$ (Moharram et al., 2014). TGA transition shows a total loss of 11.669 % up to 500 ^{0}C. No considerable loss is observed after this up to 1000 ^{0}C. The DTA curve showed the heat gain and loss in three steps at 59˚C, 330.46 ˚C and 450°C with corresponding one exothermic and two endothermic peaks at these temperatures. Above 500 °C there is almost no mass loss but there is a broad endothermic peak which might be due to phase change of zinc oxide.

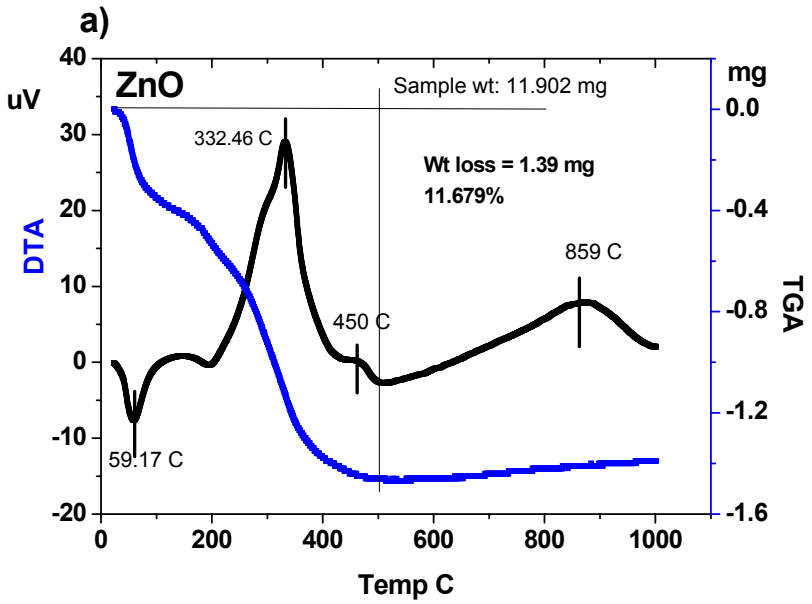

Figure 14(a). Thermal analysis of synthesized ZnO NPs (Z200)

4.6.2. Thermal Analysis Result of Activated Bentonite

Thermogravimetric analysis was undertaken to investigate the thermal behaviour of activated bentonite with Na_2CO_3. Figure 14b shows a distinct endothermic peak with a maximum between 30 to 200 °C that corresponds to the release of physically adsorbed water and the dehydration process. The dehydroxilation was executed with more and more favourable temperatures, ranging from 290 to 650°. In this work, TGA-DTA transition curve for 5% Na_2CO_3 activated bentonite clay shows a loss of mass of 1.877 mg (11.771% in the temperature range of RT-650 ˚C. No considerable loss in mass is observed after 650 ˚C temperatures up to 1000 ˚C (Khansaa et al. 2021).

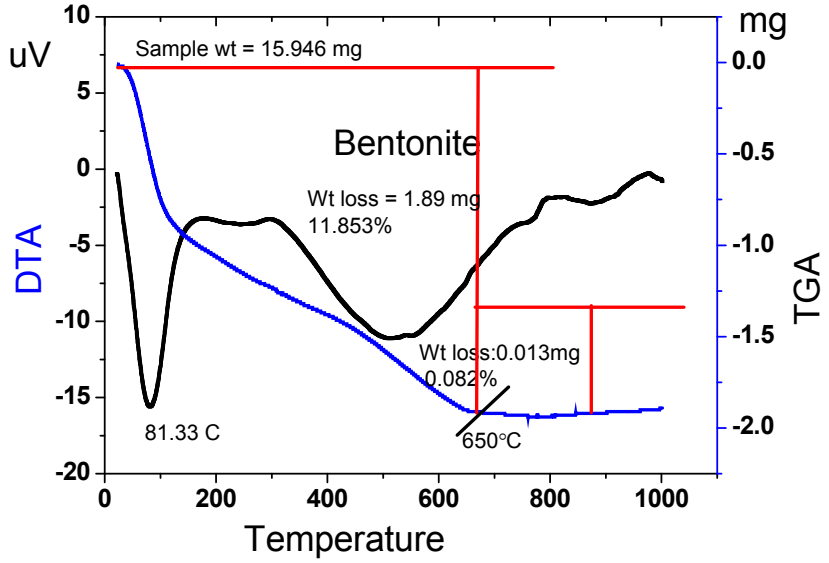

Figure 14(b). Thermal analysis of 5% Na_2CO_3 activated bentonite clay

4.6.3. **Thermal Analysis Result of ZnO-Bentonite NCs**

The thermo-gravimetric analysis (TGA) curves (Figure 14c) revealed the weight loss in three inflection points in the temperatures ranges, (RT °C–133 °C), (192-276 °C) and (378-650°C). The weight loss around these temperature ranges was ~ 11.6%, which is ascribed to the loss of water and hydroxyl group. The TGA study of ZnO-bentonite NCs shows the loss of masses (1.213 mg) for the temperature range of RT-650 ˚C. Hence, annealing above 650 ˚C seems to guarantee the formation of stable ZnO-bentonite NCs**.**

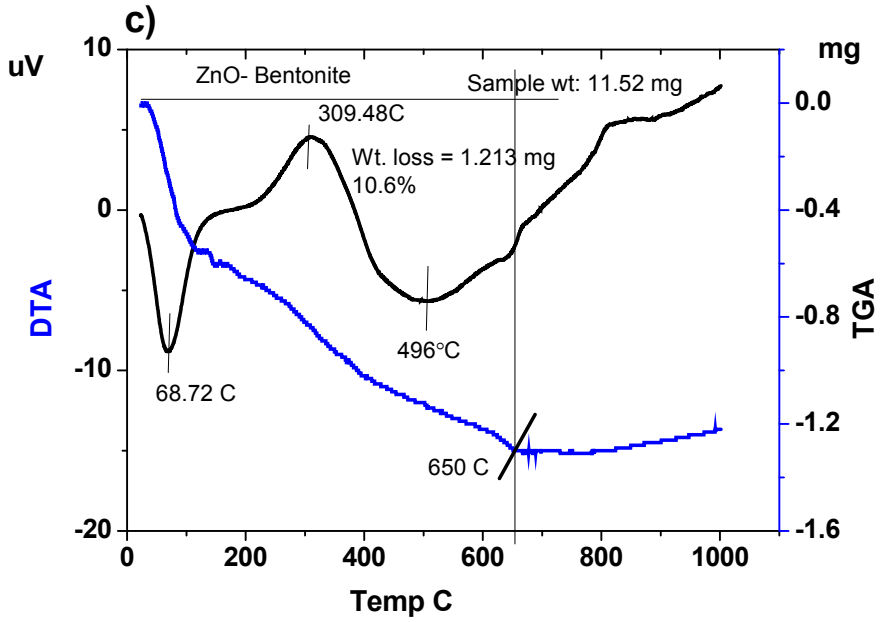

Figure 14(c). Thermal analysis of ZnO-bentonite nanocomposites(ZB100)

4.7. Transmission electron microscopic (TEM) images and SAED

The TEM study was carried out to obtain information about the internal structure (phase, morphology, average particles size and inter-planar space) of the ZnO NPs (Z100) as shown in Figure 15. The morphology of ZnO NPs obtained from the TEM images are hexagonal, rod-shaped and spherical at different nanoscales (Figure 15 a and b) and the size ranges between 5 - 35 nm. The average diameter of ZnO NPs was found to be around 17.9 nm which correspond the XRD results. The XRD pattern of ZnO NPs presented earlier in Figure.7, revealed 8 major peaks corresponding to (101), (100), (002), (110). (102), (103), (112), and (201) planes of hexagonal phase (wurtzite structure) of pure ZnO NPs (JCPDS card No.36-1451 ($P6_3mc$)). The d-spacing values derived from diffraction planes of SAED spots (1 – 8) as listed in table 4; d_{101} ZnO =2.47 Å, d_{100} ZnO =2.80 Å, d_{002} ZnO =2.59 Å and d_{110}ZnO =1.62 Å, d_{102} ZnO = 1.90 Å, d_{103} ZnO =1.47, d_{112} ZnO= 1.37 Å and d_{201} ZnO = 1.36 Å are in good agreement with XRD diffraction pattern of ZnO NPs. A lattice spacing of 0.279 nm and 0.242 nm were calculated, corresponding to the plane family (100) and (101), of hexagonal (wurtzite) ZnO (Figure 15 c and d). The SAED ring pattern is presented in Figure 15 e. The corresponding data obtained is presented in Table 5.

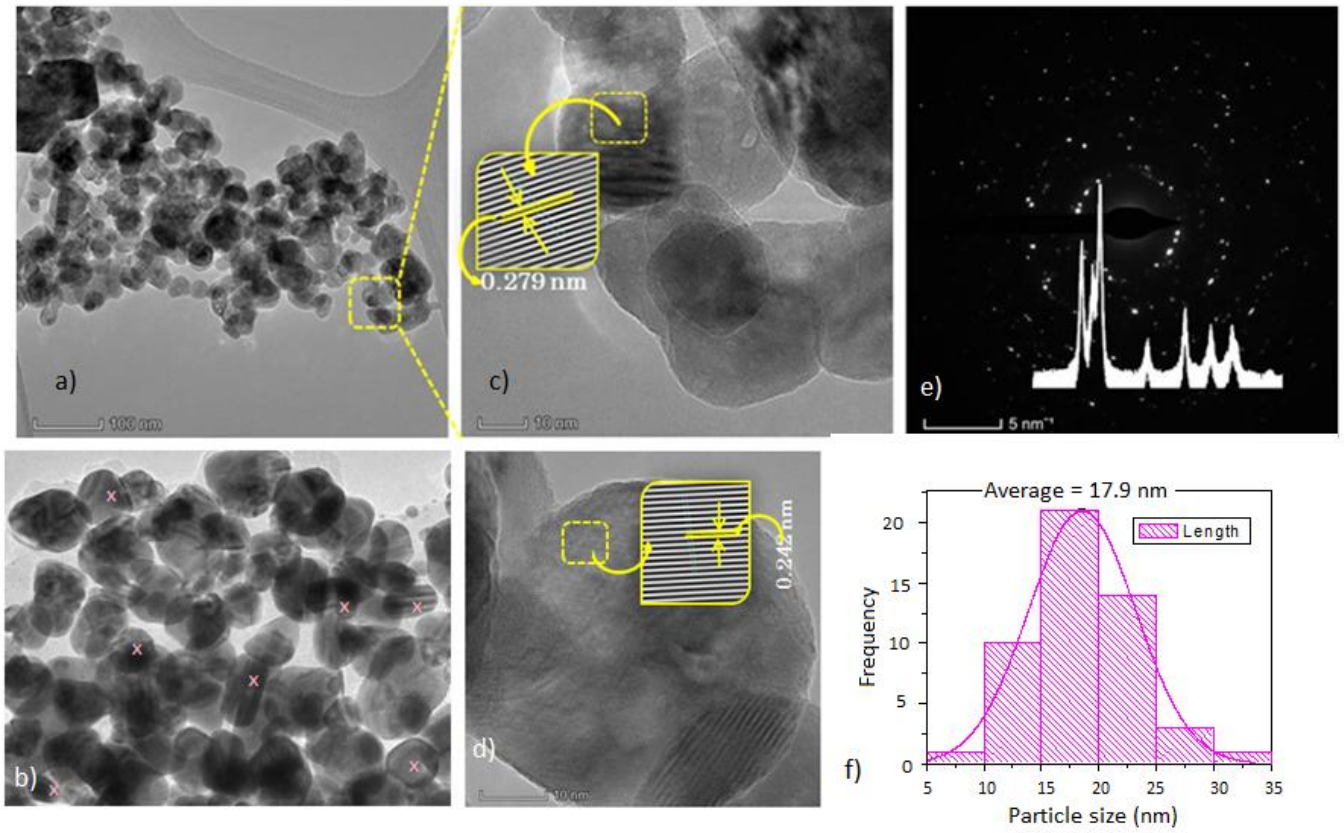

Figure 15: TEM images of ZnO NPs(Z100) (a) and (b) HRTEM images of ZnO NPs(c) &(d) IFFT with crystal planes (e) SAED pattern of ZnO NPs (1 to 8 spots) ((f) particle size distribution

Table 5. The d-spacing values for ZnO NPs from its SAED pattern

NPs	1/2r (nm^{-1})	1/r (nm^{-1})	r (nm)	d-spacing(Å)	(hkl)
ZnO	8.096	4.048	0.247	2.47	(101)
	7.14	3.57	0.28	2.80	(100)
	7.72	3.86	0.259	2.59	(002)
	12.34	6.17	0.162	1.62	(110)
	10.52	5.26	0.190	1.90	(102)
	13.6	6.80	0.147	1.47	(103)
	13.62	6.81	0.37	1.37	(112)
	14.7	7.35	0.136	1.36	(201)

Similarly, the HRTEM images and SAED pattern of the nanocomposites have been presented in Figure 16. Spherical morphological features were obtained for the composites as depicted in Figure 16a and b,

and the size ranges between 5 - 30 nm. The average diameter of ZnO NPs was found to be around 15.7 nm which correspond the XRD results. The presence of circular ring pattern on the SAED image (16g), reveal the crystalline nature of the nanocomposites. In the HRTEM image depicted on Figure 16d, the lattice spacing of 0.24 nm and 0.34 nm were calculated, corresponding to the plane family (101) and (002) of ZnO Nanoparticles and Bentonite phases respectively.

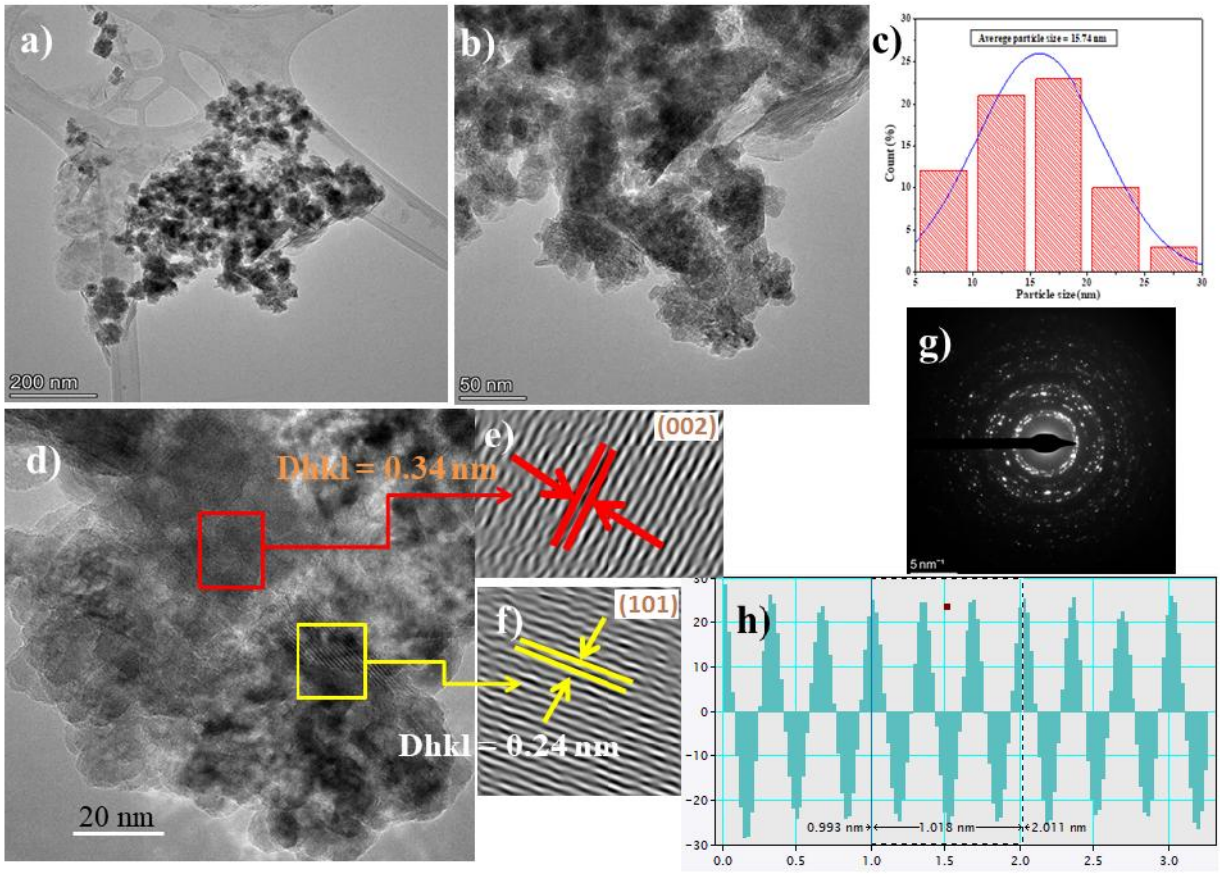

Figure 16.TEM images of ZnO-Bentonite NCs a(ZB100) at 200 nm, b) at 50 nm, c),average particle size, d)HRTEM at 20 nm, e) IFFT patterns of Bentonite, f) IFFT patterns of ZnO NPs, g) SAED pattern, and h)**Profile of IFFT with d-spacing distance.**

4.8. Fourier Transforms Infrared Spectroscopy (FT-IR) Results

FT-IR measurements were carried out to identify the major functional groups in the Plant leaf extract, purified and activated bentonites, Ag NPs, ZnO NPs, and Ag/Bentonite, ZnO/Bentonite NCs. That was to identify possible involvement of plant leaf extract in the synthesis and stabilization of NPs

and NCs. Figure 17 shows the FTIR spectrum of purified bentonite that indicates montmorillonite is the dominant mineral phase in bentonite. The montmorillonite presented bands in the region of approximately at 3557cm^{-1} is due to stretching vibrations of structural OH groups (hydroxyl group) of montmorillonite and a broad band at 3424 cm^{-1} of the OH stretching vibration and structural adsorbed water, coordinated to octahedral Al^{3+} cations. In the lower frequency region, montmorillonite had a strong band at and around 1020 cm^{-1} bonding to the Si–O stretching vibration of bentonite mineral. The absorption band at 1635 cm^{-1} was attributed to the OH deformation mode of water. The clay spectrum also contains a band in the region 600-800 cm^{-1} which indicated the presence of quartz. In addition the peak at 462 cm^{-1} angular Si-O-Si vibrations and 523 cm^{-1} band is related to the angular Si-OH-Al (octahedral layers of aluminosilicate) vibration in the bentonite (Fisseha, 2017).

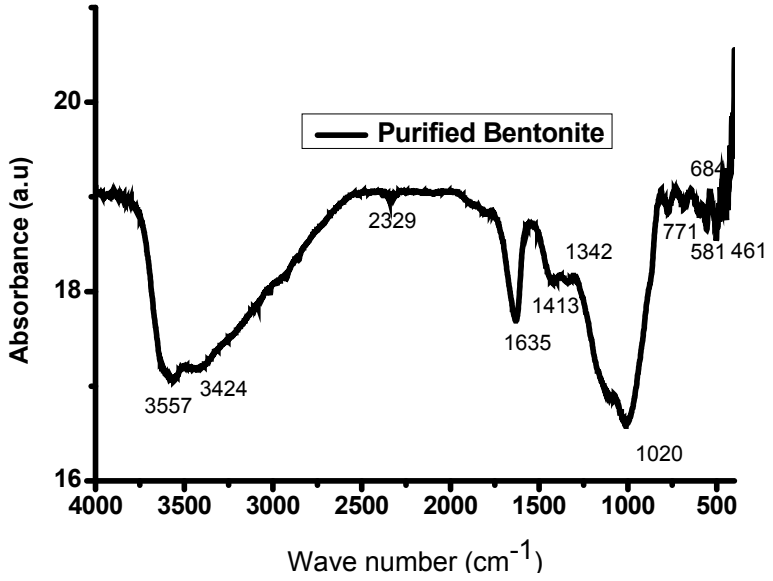

Figure 17: FTIR spectrum of purified Bentonite

FT-IR of bentonite is sensitive to the structural changes which occur upon soda activation and the IR data recorded in this study confirmed that both the octahedral and tetrahedral sheets of the activated bentonite were not influenced by soda attack (Figure 18). The intensity of stretching bands observed at 3600 cm^{-1} for purified bentonite (Al-OH-Al along with the Al-Mg-OH stretching vibrations) was lowered than the activated bentonite by sodium carbonate. Activation of bentonite by Na_2CO_3 has changed the peaks of the bands associated with the absorbed water at 3424 cm^{-1} (H-O-H stretching).

Also, the activation of bentonite by Na_2CO_3 affected the peaks of the bands associated with the absorbed water at 1635 cm^{-1} (H-O-H bending). Changes in the intensities of these bands were explained as due to gain of water molecules as pure bentonite to activated bentonite (Kumar & Lingfa, 2020).

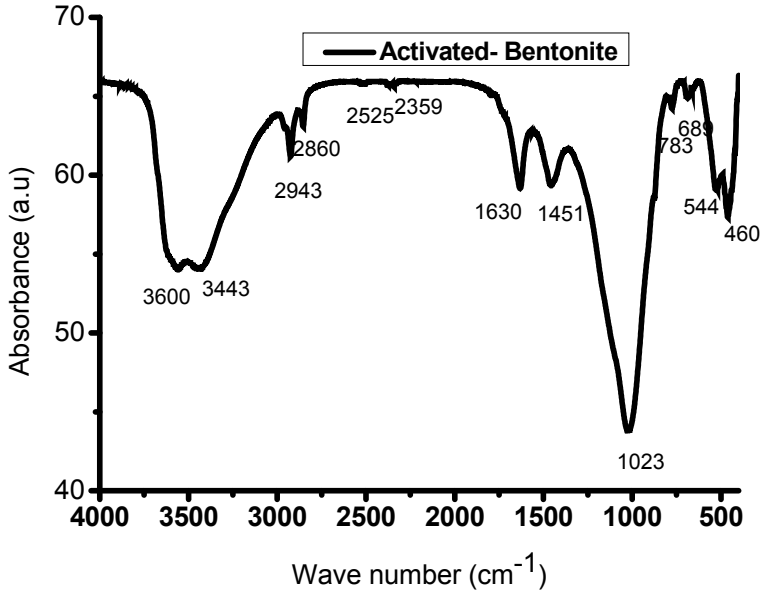

Figure 18: FTIR spectrum of 5% Na_2CO_3 activated Bentonite

The FT-IR Profile of the *H.abyssinica*plant Leaf Extract are listed in the table 6 and depicted on spectrum 19. The peak observed at 3400 cm^{-1} is typical of –OH (alcohol) while, 3000 and 2854 cm^{-1} can be said to be C-H (stretch) for alkanes. Also, the peak at 1615 cm^{-1} (C=C) is that of conjugated alkenes. The signal at 1358 (C-O) is that of alcohol and 1010 cm^{-1} (C-O stretch) is also typical of alcohols. Table 6 and Fig 19, FTIR spectrum analysis revealed the presence of two basic functional group; C=O and O-H which indicate the presence of alcohol, phenol or esters. The O-H (Alcohol/ Phenol) group was observed in the leaf extract with wavelengths of 3400 cm^{-1}. The peaks between the range of 1000 – 1500cm^{-1} are present in the extract is due to the presence of the C-O bond. This band may either be an alcohol, ester, ether or anhydride. The presence of secondary amine was also detected at 1615 cm^{-1} for the extract (S. Kumar et al., 2020, Awwad, 2014).

Table 6: FT-IR summary of the *H.abyssinica* plant Leaf Extract

Peak values (cm^{-1})	Functional group	Class
3400	-OH	Alcohol
3000	-C-H (Stretch)	Alkane
2854	C-H	Alkane
1615	C=C	Alkene(conjugated)
1358	C-O	Alcohol
1010	C-O (strech)	Alcohols

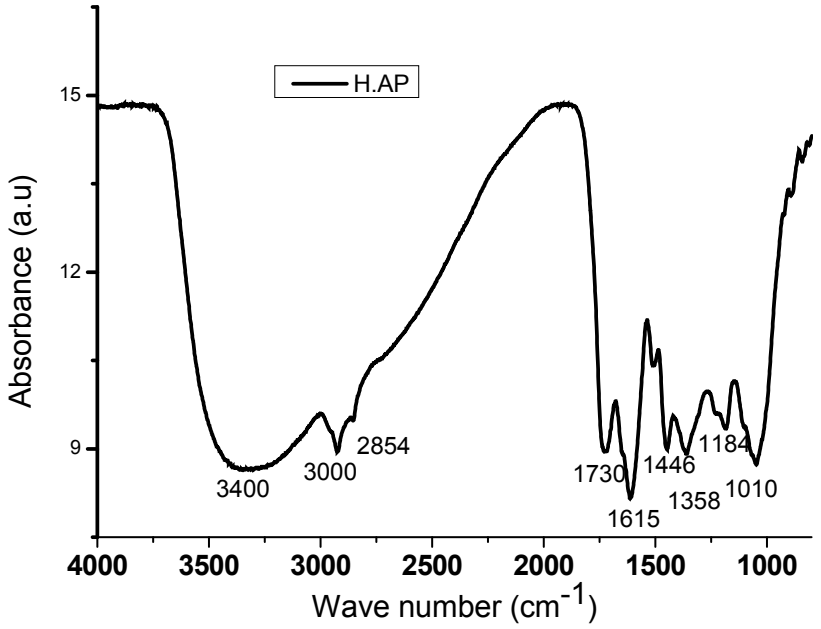

Figure 19: FT-IR spectrum of *H. abyssinica* crude extract

Figure 20 shows the FTIR spectrum of ZnO before calcinations NPs which was resulted in various peaks at 3433, 2911, 2860, 1429, 1020, 673 and 466 cm^{-1}. The FTIR band around 1020, 1429, 1576 and 3433 cm^{-1} suggests the presence of bio-molecules present in leaf extract on ZnO NPs which acted as capping agents. The broad band peaks at 3433 cm^{-1} correspond to H bonded OH stretching of polyphenols and flavonoids (Jamdagni *et al.*, 2016). Two low intensity peaks around 2911 cm^{-1} and 2860 cm^{-1} corresponded to the symmetric and asymmetric C–H of the aliphatic group and C–H stretching

vibrations of an aromatic aldehyde. The 1576 cm^{-1} peak results from the stretching bands of C=C functional group on the as synthesized ZnO was disappeared because of calcinations at 500 °C. The peak around 1429 cm^{-1} refers to the amine –N=O vibration stretch in protein amide linkages (Jamdagni *et al*., 2016). The 1023 cm^{-1} and 679 cm^{-1} peaks correspond to alkanes and evidently, C-H bend in alkynes, respectively and the peak in the region between 400 and 600 cm^{-1} is assigned to Zn-O stretching vibration, confirming the formation of ZnO using *H. abyssinica* extract as a reducing and capping agent (Dobrucka and Długaszewska, 2016). On the same Figure 20, the FTIR spectrum of calcinated ZnO NPs which resulted in various peaks in the region of 400 cm^{-1} to 4000 cm^{-1}. The band around 3400 cm^{-1} was assigned to the O-H stretching vibration. The Peaks at 2911 cm^{-1} and 2859 cm^{-1}corresponds to stretching of the symmetric and asymmetric C–H of SP^3 (Kahsay, 2021). Stretching vibration at 1743 cm^{-1} and 1429 cm^{-1}were attributed to C=O (carbonyl group) and C=C, respectively (Suresh *et al*., 2018). The intense band located at 1023 cm^{-1} and 887 cm^{-1} illustrates the presence of C-C, C-N, and C-O cm^{-1} stretching vibration. The stretch for ZnO NPs was found in the region 400-600 cm^{-1}. Therefore the synthesized particles were surrounded by proteins and metabolites such as terpenoids and flavonoids having functional groups.

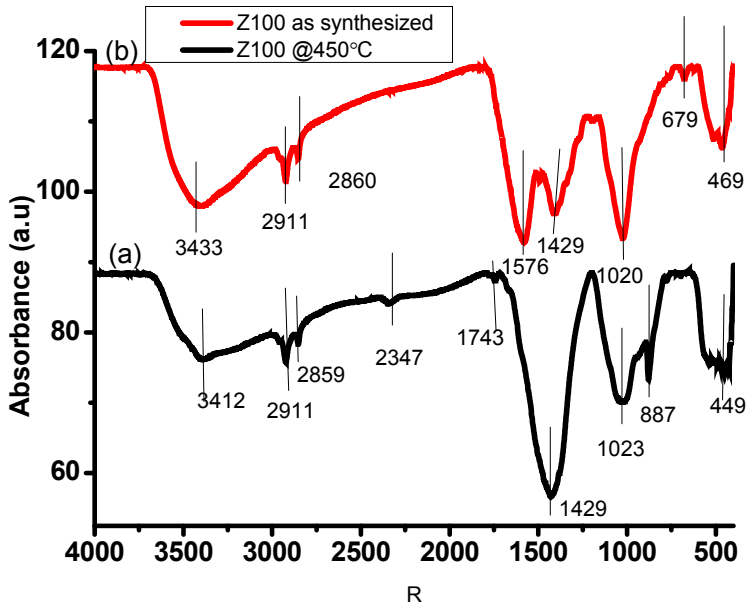

Figure 20: ZnO synthesized with 1:1ratio (a), before calcination Z100 b) and Z100 calcinated at 500°C.

As depicted on Figure 21, the broadband between 3400–3700 cm^{-1}, represents the stretching vibration of the O-H group of Zn-OH and Si-OH in ZB200 composites. The spectrum of calcined nanocomposite exhibited weak intensity band at 2843 and 2920 cm^{-1}, which indicates the removal of C-H bond in CH_2 and CH_3 groups of plant leaf extract from the surface of the ZnO-Bentonite composite. The peak of Si-O-Zn also appeared at 1024 cm^{-1}. The absorption peaks at 460 cm^{-1} and 400 cm^{-1} in both ZB200@650 and as synthesized nanocomposites are assigned to Zn-O bond similar to the earlier study (Chakraborty et al., 2019) with the vibration of Zn-O appeared in the range of 540-426 cm^{-1}, (Kassem,2015).

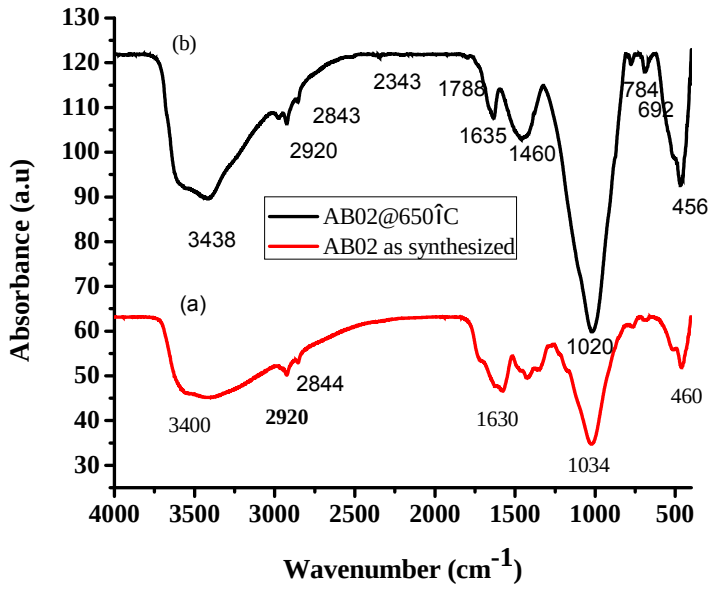

Figure 21: FT-IR spectra for (a) ZB200 calcined at 650°C (b) as synthesized ZB200

4.9. X-ray Diffraction (XRD) Analysis Ag-NPs and Ag-Bentonite

4.9.1. X-ray Diffraction Analysis of Ag-NPs

Diffraction peaks of Ag NPs (Figure 22) at 2θ values of 38.074°, 44.365°, 64.485°, and 77.424°, corresponding to (hkl) values of (111), (200), (220), and (311) Bragg's reflections, which are comparable and evident in all patterns, which previously reported by (Bar et,al., 2009) and suggest that the synthesized Ag NPs using aqueous extract of plant leaf is found to possess a FCC structure which were in good agreement with reference to the unit cell of FCC structure of silver nano-crystals (Joint

Committee on Powder Diffraction Standards: File (JCPDS file No. 5-2872). Different phytochemicals in *H. Abyssinica leaf extract* reduced the silver ion and stabilized silver metallic nanoparticles (Melkamu and Bitew, 2021). The high intense peak reflection is observed for (111) plane of Ag NPs crystal with high degree of crystallinity. The diffraction peaks are broad and the crystallite sizes estimated using the Debye–Scherer equation are 9.1 nm (A400), 9.4 nm (A200), 10.0 nm (A100), 11.2 nm (A50) and 11.8 nm (A25) respectively.

very small (Wani et al., 2011). The unassigned peaks, marked with # at 2θ near to 20°, 27.8°, 32.20 ° and 46.2 ° in Figure 22 could be due to the formation of crystalline oxide or Ag_2O (JCPDS, file No. 42-0874), it might be due to the small volume of leaf extract used for the synthesis (Yang et al. 2016). This result validates the reducing and capping power of *H. abyssinica* plant leaf extract in the case of Ag NPs synthesis. No remarkable change in the average crystallites size was observed when different volumes of leaf extract were mixed with the 0.2M $AgNO_3$concentration.

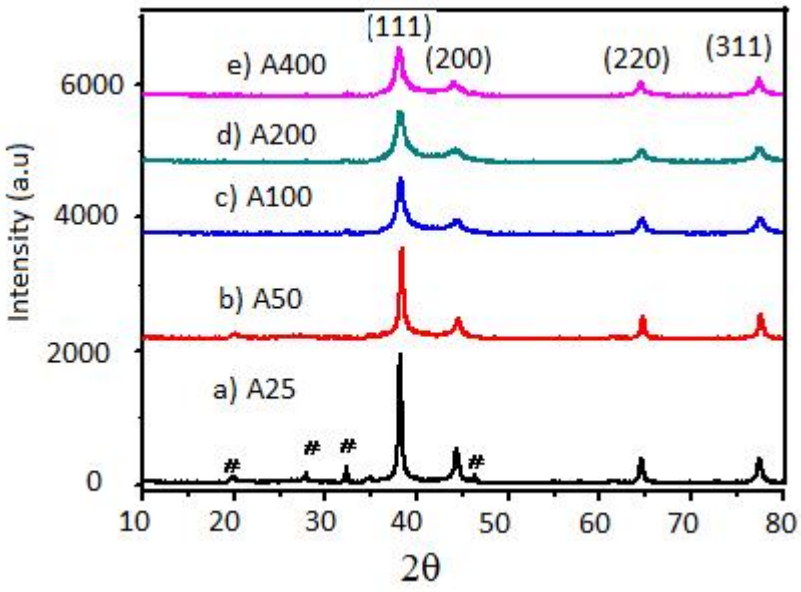

Figure 22: XRD Patterns of the Ag NPs synthesized with different leaf extract volumes

Table 7: Average particle sizes of Synthesized Ag NPs Samples

	2 θ	d	θ	cosθ	β(Rad)	D(nm)	Av.Size
A400	**38.2312**	2.35224	19.1156	0.94486	0.021084	6.960004	9.05
	77.4392	1.23148	38.7196	0.780216	0.017453	10.1819	
	64.5129	1.44329	32.25645	0.845668	0.016406	9.993466	
A200	**38.2017**	**2.35399**	19.10085	0.944944	0.019844	7.393962	
	77.4175	1.23177	38.70875	0.780335	0.017162	10.35325	
	64.5329	1.44289	32.26645	0.845575	0.015708	10.43877	9.40
A100	38.1138	2.35921	19.0569	0.945195	0.014888	9.853112	
	32.2007	2.77765	16.10035	0.960777	0.015708	9.1871	
	77.3592	1.23255	38.6796	0.780653	0.016057	11.06109	10.03
A50	38.2	2.3527	19.1	0.944949	0.0148	9.914049	
	64.5	1.4423	32.25	0.845728	0.0157	10.44217	
	77.4	1.2308	38.7	0.78043	0.0134	13.25813	11.21
A25	38.0796	2.36125	19.0398	0.945292	0.016464	8.908977	11.81
	77.3627	1.2325	38.68135	0.780634	0.013561	13.09711	
	64.4329	1.44489	32.21645	0.84604	0.012217	13.41389	

4.9.2. XRD analysis for Ag-Bentonite NCs

The XRD patterns of bentonite with the diffraction peaks at 2*θ*¼ 8.6^{o}, 15.8^{o}, 20.08^{o}, 26.04^{o}, 29.42°, 30.68°, 34.74^{o} corresponding to (001), (211), (220), (400), (330), (332), (431) Bragg's reflections. The peaks are evident in all patterns, which are also consistent with other reported works. Ag NPs characteristic peaks are also shown at 2θ values of 38.074°, 44.365°, 64.485°, and 77.424°, corresponding to (hkl) values of (111), (200), (220), and (311) Bragg's reflections, in the mixed phase composites of AB005 and AB02 as depicted on Figure 23 and table 8. The crystallites sizes of Ag NPs in bentonite matrix are also influenced by the concentration of $AgNO_3$ solution used for the synthesis,

which are comparable with the other results reported (Shameli,et al., 2010, Maga˜na et al., 2008, Shameli et al., 2011, Santos et al., 2011). The presence of the diffraction patterns of Ag and bentonite confirms that the prepared composites are composed of the two species.

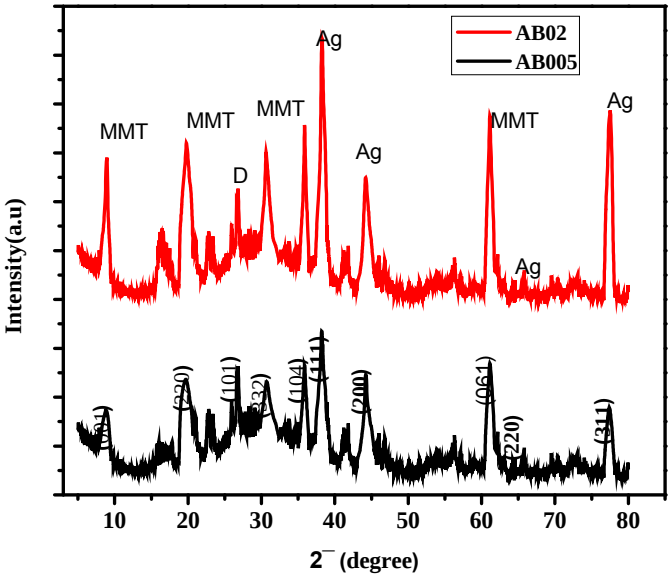

Figure 23: XRD patterns of the Ag-Bent NCs

Table 8**:** The average particle sizes of Ag- Bentonite composite samples

Composite	2θ (°)	d(Å)	β(rad)	(hkl)	D(nm)
AB005 Ag NPs peaks	38.2	2.3527	0.0148	(111)	8.83
	64.5	1.4423	0.0157	(220)	6.88
	77.4	1.2308	0.0134	(311)	8.71
Na-AB Na- Activated Bentonite peaks	19.72	4.49833	0.0079	(100)	17.97
	26.6138	3.34670	0.0028	(400)	49.70
	29.4131	3.03425	0.0031	(330)	45.30
Average D (nm)					22.90
AB02 Ag NPs peaks	38.1	2.3595	0.0107	(111)	12.20
	64.4	1.4439	0.0091	(220)	12.86
	77.3	1.2322	0.0097	(311)	11.10
Na-AB	19.78	4.48291	0.0103	(100)	13.80

Na- Activated Bentonite peaks	27.8	3.20469	0.0066	-	21.20
	34.6	2.58612	0.01117	(105)	12.40
Average D (nm)					13.93

4.10. UV-Visible Analysis and optical properties

4.10.1. Variation of $AgNO_3$ concentration and optical properties of Ag NPs

The effect of concentration of $AgNO_3$ on the synthesis of Ag NPs using fixed volume of plant leaf extract and the UV-Vis data of these samples are illustrated in Figure 24. This operational parameter was monitored at various concentrations of silver ion solution. The experiment was carried out on the following series of silver ion concentration: 5 mM , 2 mM, 1m M, 0.5 m M , 0.01m M and 0.001 mM. The maximum formation of the absorbance peak is in the range of 395–422 nm and the colour turned to brown. For the different concentrations, the intensity was increased with an increase in the concentration of Ag ion. A distinctive and maximum absorbance was observed at a wavelength of 420 nm for a concentration of 2 mM $AgNO_3$ solution. The height of the absorption peak of UV-Vis spectrum around 420 nm intensifies as the concentration of silver nitrate increased and the maximum peak intensity was obtained for 2mM of $AgNO_3$ concentration (Figure.20). Results reported by (Christopher et al., 2015) showed that 6 mM concentration of silver nitrate using plant leaf extracts as a reducing agent gave the maximum formation with the absorbance peak at 400–420 nm and the colour turned to brown. Peaks of different absorbance and different wavelength observed on the figure confirm the influence of concentration of $AgNO_3$ on the synthesis of Ag NPs. Varying the concentration of Ag ion solution will affects the size and shape of the Ag NPs produced and this result correlates with (Nadzir et al., 2019).

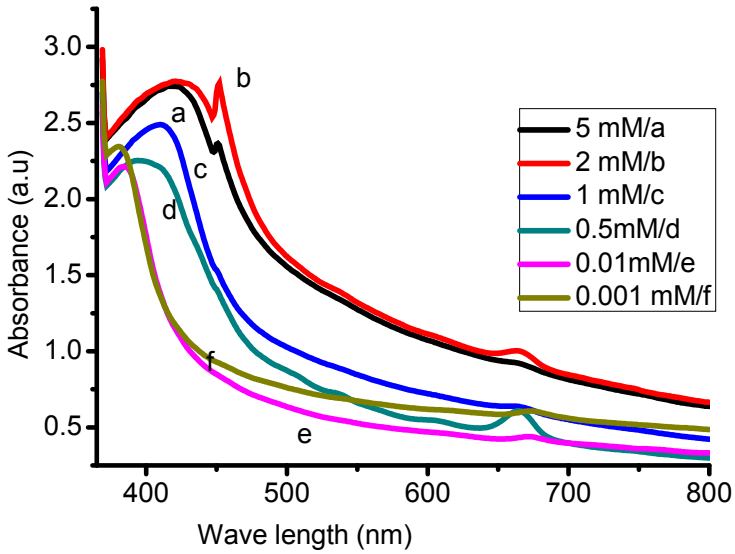

Figure 24.UV–Vis absorption spectra of Ag NPs synthesized using different $AgNO_3$ concentration

Ag NPs band gap was estimated using $(\alpha\lambda\nu)^{1/2}$ vs. νh plot as shown in Figure 25. The graph showed that the band gap slightly decreased with decreasing the concentration of the $AgNO_3$ solution. The band gap energies determined for five Ag NPs prepared from the equal volumes of plant leaf extract and $AgNO_3$ salt solution for different concentration: 5 mM , 2 mM, 1 mM, 0.5 mM , 0.01 mM and 0.001 mM $AgNO_3$ are 2.85 eV, 2.76 eV, 2.46 eV, 2.5 eV, 2.4 eV,and 2.38 eV respectively. These results might be obtained due to the increase or changes of the sizes of the Ag NPs with concentration of the $AgNO_3$ as reported by (Isah et al., 2016).

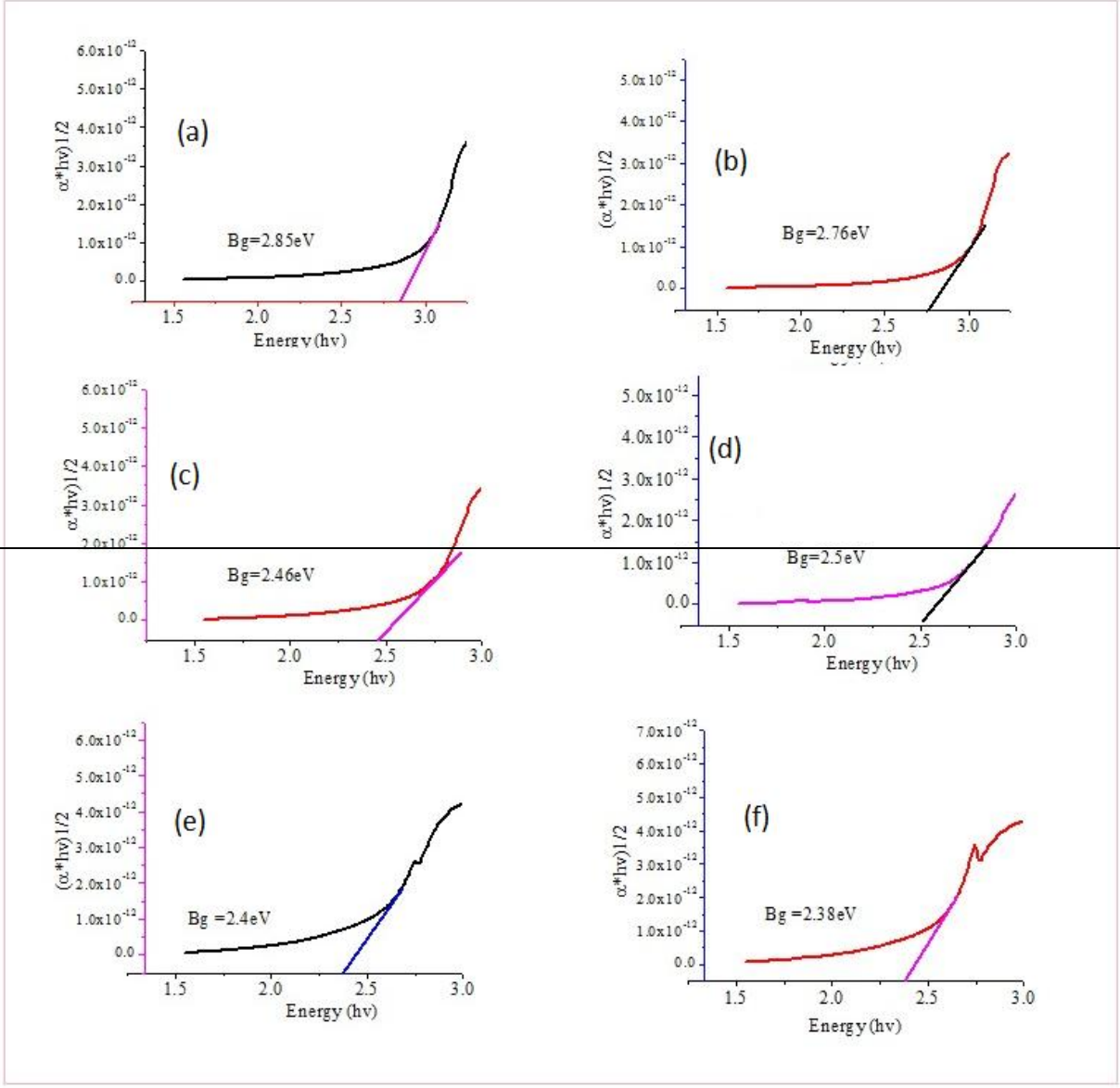

Figure 25. Optical energy band gap for Ag NPs synthesized from different concentration of $AgNO_3$ using fixed volume of plant leaf extract.

4.10.2. Effects of volume ratio of $AgNO_3$ to plant leaf extract

Following the procedure reported by (*Sharma et al., 2020)*, the effects of volume ratio on optical property Ag NPs suspension was studied by varying the volume ratio the leaf extract in the ratio 1:1, 1:2, and 1:4 (A100, A200 and A400) by keeping constant the volume of 2 mM $AgNO_3$ solution. The absorption peak at 406 nm with maximum absorbance was recorded at 1:1 volume ratio (15 mL $AgNO_3$ solution to 15 mL extract) and it was an optimized condition for the synthesis of Ag NPs. The absorption peaks were less broader and slightly lower absorbance were recorded for 1:2 and 1:4 volume ratios with lower and higher volume of extract which indicates a slow reduction of Ag^+ to Ag^0. Thus, other works was carried out using this optimum volume ratio. It was in a good agreement with the previously studied and synthesized Ag NPs from plants leaf aqueous extract by (*Sharma* et al., 2020).

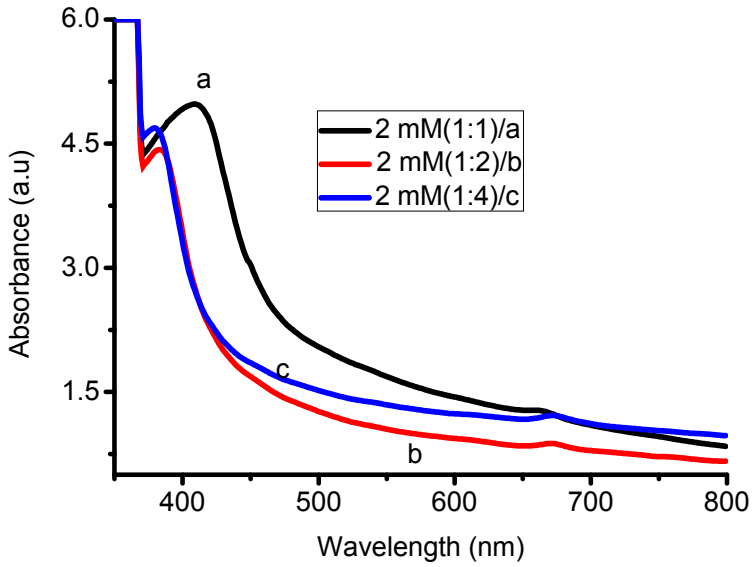

Figure 26. UV-Vis absorption spectra of Ag NPs suspension by varying volume ratio of plant leaf extract for fixed volume of 2mM $AgNO_3$ solution

4.10.3. UV-Vis of Ag/Bentonite

The UV-Vis absorption spectra of Ag-bentonite NCs with different concentrations: 0.05 M, 0.1 M and 0.2M of $AgNO_3$ and fixed mass of bentonite denoted as (AB005, AB01 and AB02) respectively are shown in figure 23. Improved band and maximum absorption was observed for the AB02 composite.

When the concentration increases large amount of Ag^{+} has been converted to Ag NPs on the surface and gallery of bentonite. In Ag-bentonite nanocomposite synthesized with 0.2 M $AgNO_3$ (AB02), the absorption peak slightly red-shifted to higher wavelength (426 nm), which indicated the increase in the size of Ag NPs. UV-Vis spectra of bentonite showed (Fig. 27) a peak 275 nm (strong) corresponding to tetrahedral coordinated ions Fe^{3+} (Shameli et al., 2011, Venkatathri,2006).

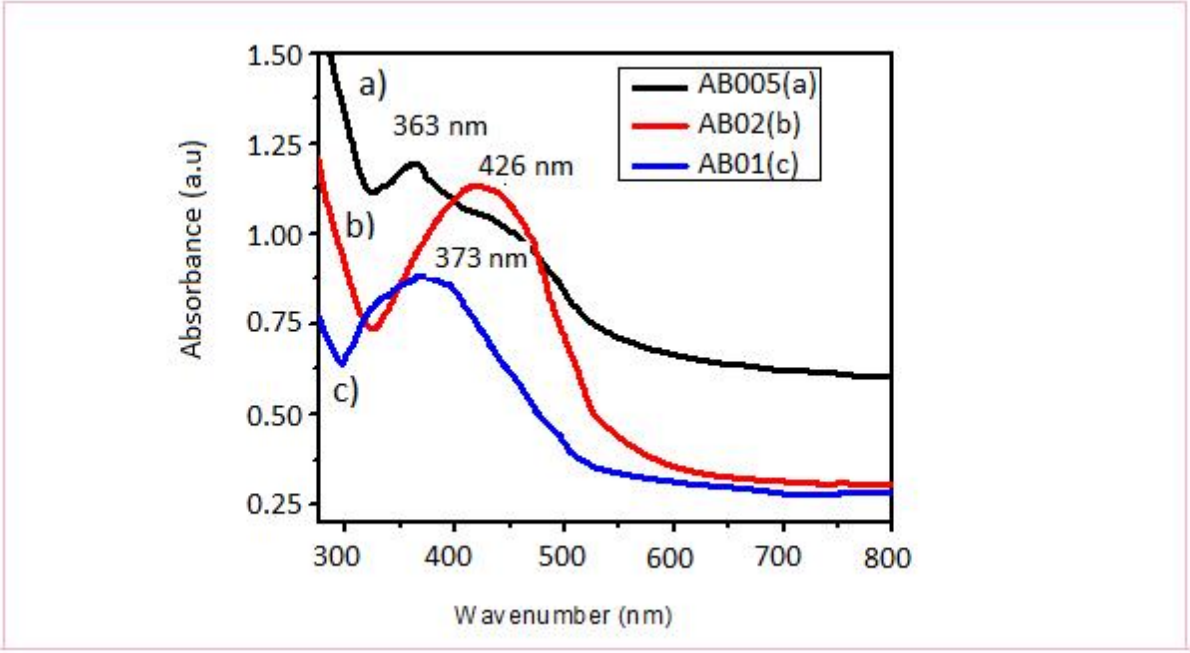

Figure 27: UV-Vis absorption spectra of Ag-bentonite NCs a) AB005 b) AB02 and c)AB01

4.11. SEM-EDX of Ag NPs & Ag-Bentonite

The surface morphology and elemental compositions of the synthesized Ag NPs were determined by scanning electron microscopy–energy dispersive X-ray (SEM-EDX). The SEM image of Ag NPs was blurred. But, it showed almost spherical shaped particles (Figure 28). The EDX spectrum of the intense peak at 3 keV, suggesting Ag is the main element in Ag NPs. In the EDX spectra of the Ag NPs, Cu and C peaks appear due to the scattering caused by the carbon film and copper of the device grid (Król-Gracz et al. 2011). Figure 29 displayed the micrograph of modified bentonite with Ag NPs somewhat different from pure Ag NPs. Aggregated particles with a large number of spherical particles were observed in Ag-Bentonite SEM image. The composition of the Ag-Bentonite analysis by EDX is one of the supporting evidence (Wu et al., 2011).

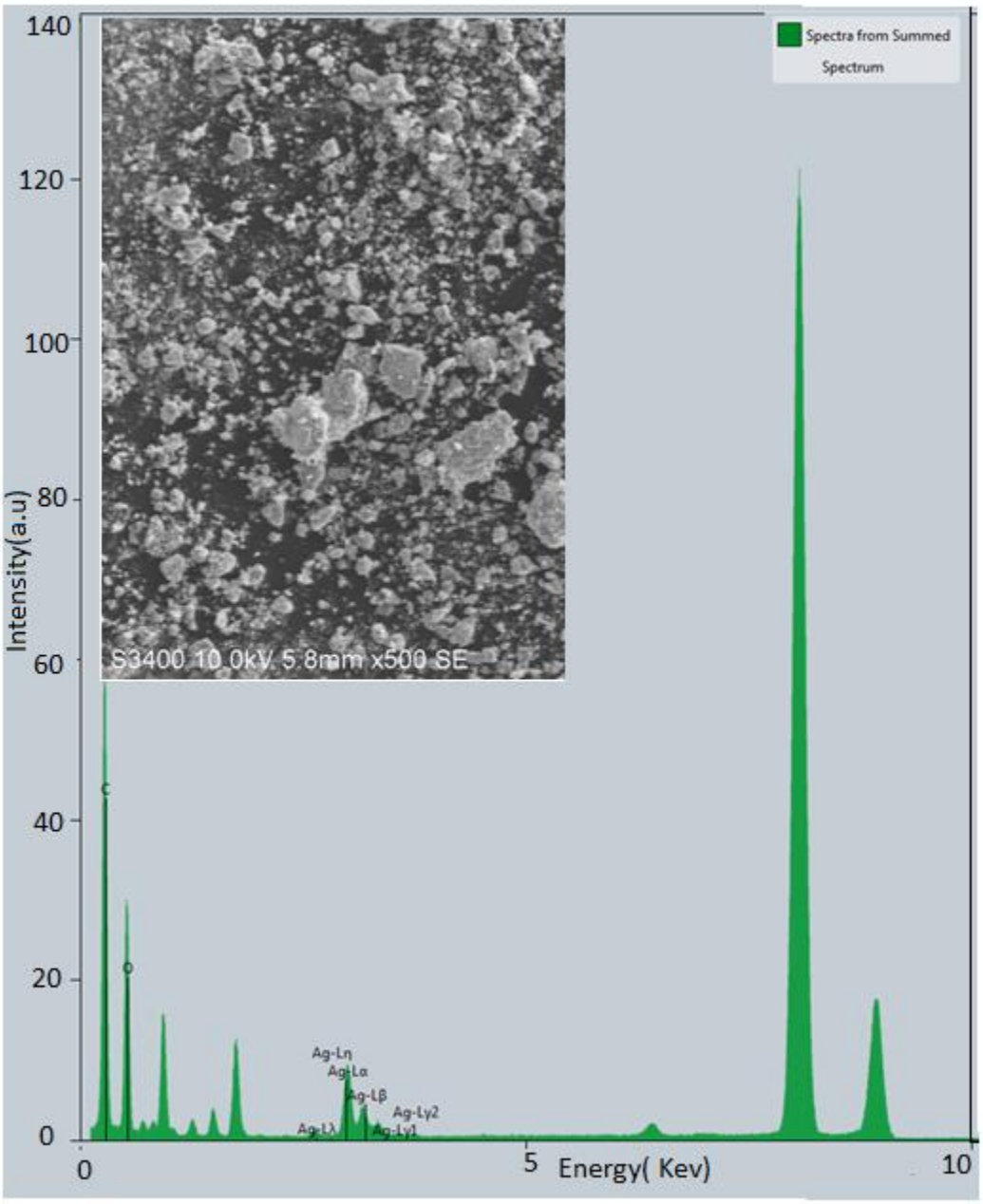

Figure 28. SEM –EDX of as synthesized Ag NPs using leaf extract of *H. abyssinica*

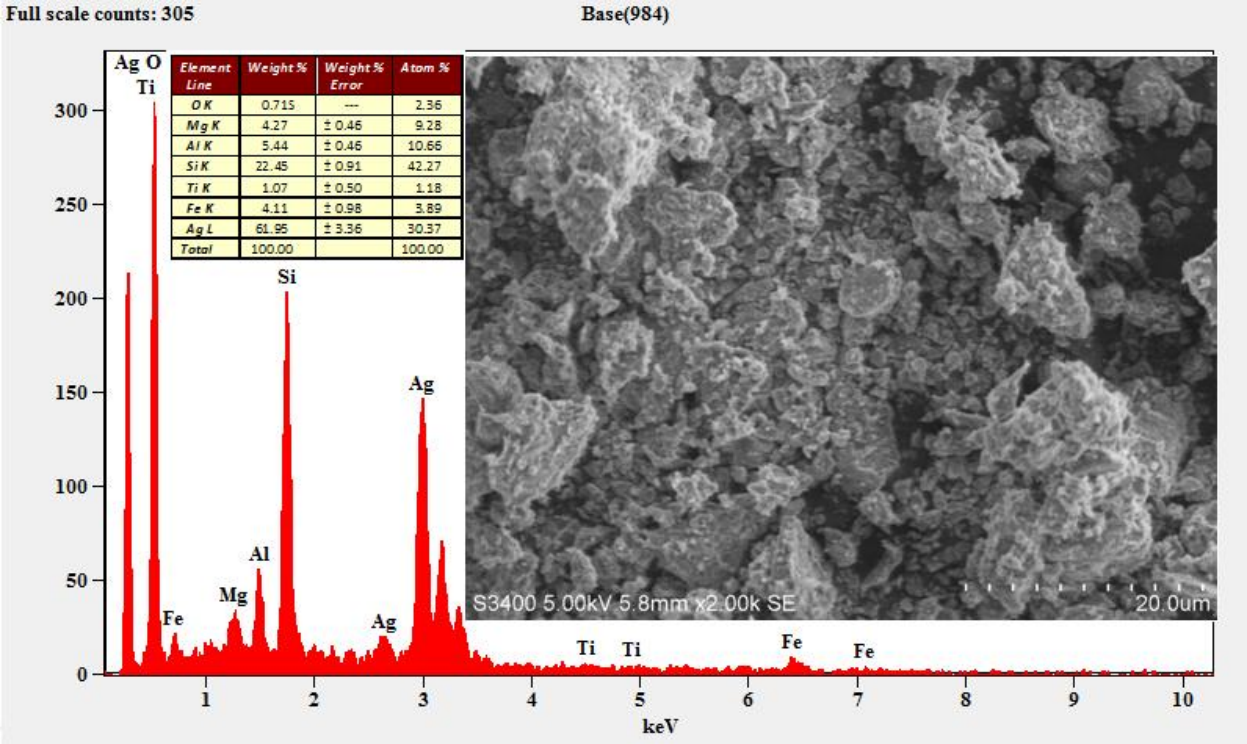

Figure 29: SEM –EDX of as synthesized Ag/Bentonite NPCs using leaf extract of *H. abyssinica*

4.12. HRTEM, TEM images and SAED of Ag NPs and Ag/Bentonite

Transmission electron microscopic (TEM) study was carried out to obtain information about the internal structure (size and morphology) of the biosynthesized Ag and Ag-Bentonite as shown in Figures 30 and 31. From the TEM image, it is clear that the morphology of Ag NPs is hexagonal, cylindrical -shaped or spherical at different nanometer scales and the size ranges between 30 - 70 nm. The average diameter of Ag nanoparticles was found to be around 52 nm which greater than the XRD results. The TEM micrographs which exhibited spherical, cylindrical, as well as hexagonal shapes are clearly presented in fig.26 (a′). HRTEM shows the crystalline structure of single Ag nanoparticle, with a lattice spacing of 1.23 nm was calculated, corresponding to the plane family (111) of (FCC) Ag (Fig.26 d and e). Additionally, Fig. 26 c shows selected area electron diffraction (SAED) pattern and the results are consistent with the XRD diffraction pattern. The XRD pattern of Ag NPs presented earlier in Fg.18, revealed 4 major peaks corresponding to (111), (220), (311), and (200) planes of phase FCC. The d-spacing values of the derived diffraction planes from spot 1 to spot 4; d_{111} = 2.46 Å, d_{220} = 1.46 Å, d_{311} =1.23 Å and d_{200} = 0.96 Å are in good agreement with XRD diffraction pattern of Ag NPs. The HRTEM image as shown in

Figure 26d affirms as the synthesized material is crystalline Ag NPs with the d- spacing value of 2.4 nm for (111) plane from magnified lattice fringer of the indicated HRTEM image.

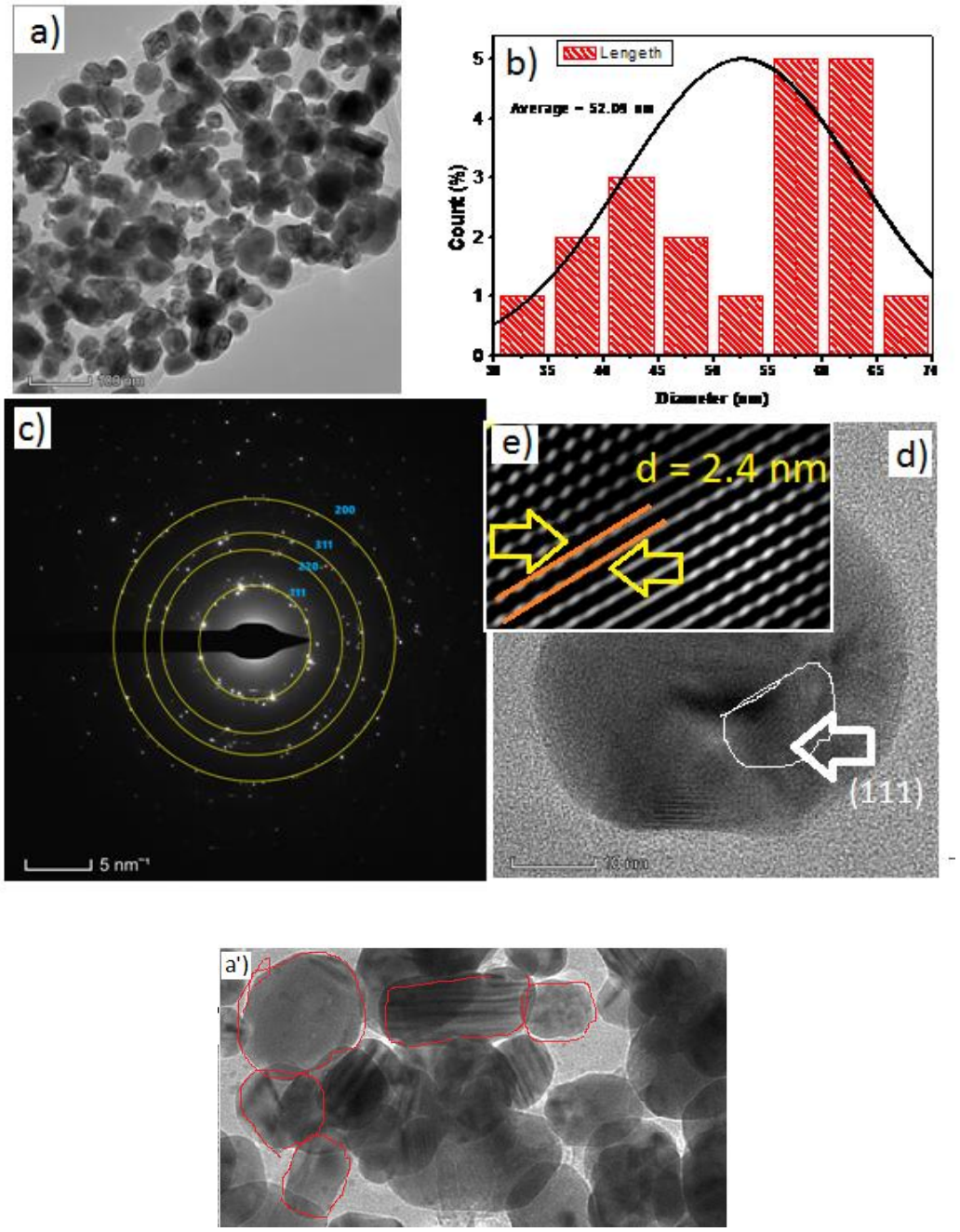

Figure 30**:** a) TEM of Ag NPs (A100) a′) Magnified TEM image of (A100), c) SAED pattern of Ag NPs (A100)(1 to 4 spots) (d) HRTEM with crystal planes,

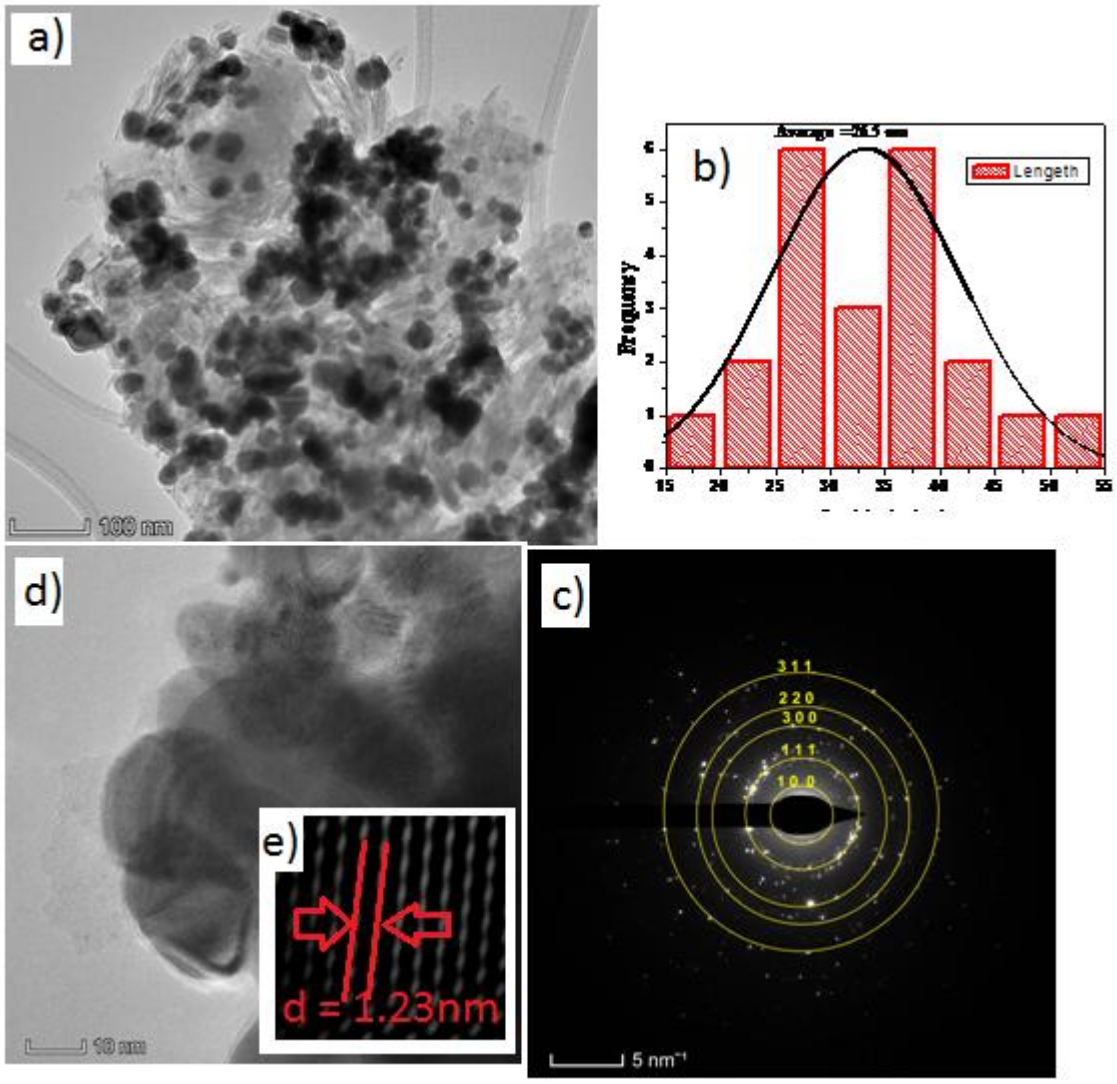

Figure 31: Ag/Bent NCs (AB02) a) TEM images b) histogram, (c) SAED spots and (d) HRTEM of size distribution

The TEM micrographs of Ag/Bentonite NC with spherical, cylindrical, as well as hexagonal shapes were presented in Figure.31 a, the composite particle sizes were vary from 15 nm to 55 nm with an average particle size of 26.5 nm, as determined by image J Software and depicted in Figure 31b. SAED of Ag/Bent displayed on Figure 31 c contains five spots; two spots ((100) and (300)) belongs to bentonite planes and three spots; (111), (220) and (311) from Ag NPs planes of the composite. In the HRTEM of Ag/Bent one of the Ag plane (311) with d-values 1.23 nm obtained from magnified lattice fringer of the HRTEM image as depicted on figures 27(d and e).

4.13. FT-IR Results of Ag NPs & Ag-Bent

Figure 32 shows the FT-IR spectra of the optimized Ag NPs and Ag-Bent NCs. The common peaks detected at around 3559 cm^{-1}, 3438 cm^{-1}, and 1635 cm^{-1} on the surface of nanomaterials indicate typical stretching vibration of the hydroxyl functional group (O-H), stretching vibration of C-H, and bending vibration of O-H, respectively. The stretching vibration of the C=C group was also found in the 1610-1680 cm^{-1} range(Movasaghi et al.,2008). The bonds or functional groups such as –C–O–C–, –C–O, and – C=C– derived from heterocyclic compounds, e.g., alkaloid or flavones and the amide (I) bond derived from the proteins that are present in the leaves extract are the capping ligands of the nanoparticles. The peaks belong to carbonyl, alcohol, and nitro functional groups confirms the presence of alkaloid, phenol, terpenoids, polysaccharides and flavonoid present in the H. abyssinica leaves extract which is responsible for the reduction of Ag^{+} ions to Ag NPs. These functional groups have been observed on the surface of Ag NPs produced from leaf extracts (Maheshwaran et al., 2021). The wide and strong bands at 3559–2925 cm^{-1} were caused by bonded hydroxyl (–OH) or amine groups (–NH) in the H. abyssinica extract, as well as aliphatic C–H. The carboxyl group (C=O) stretching vibrations are responsible for the peak at 1635 cm^{-1} (Shameli et al., 2012). The peak at 1020 cm^{-1} is due to Ag-NP banding with oxygen from hydroxyl group of H. abyssinica compound. The vibration bands in the 3559 cm^{-1} area related to O–H stretching, whereas 3438 cm^{-1} is the interlayer O–H stretching (H bonding), 1635 cm^{-1} corresponded to H–O–H bending. In contrast, these peaks were either absent or displayed drastically reduced intensities in the corresponding silver nanoparticle spectra. This seems to suggest that functional groups in this region are involved in the reduction and stabilization of the Ag NPs by their subsequent oxidation. Additionally, ether linkages, C–O and C–O–C functional groups are thought to be groups of flavones, terpenoids and polysaccharides present in H. abyssinica leaf extract(Melkamu and Bitew , 2021). These reducing agents are able to donate electron pairs to the metals when the reduction occurs on the particles' surface. Also the polyphenols act as capping agent as they introduce negative charge on the reduced metal's surface (Melkamu and Bitew , 2021).

After compositing of Ag NPs with bentonite more peaks appeared around 459 cm^{-1}(Si–O–Al), 520 cm^{-1} (Si–O–Mg), (Peaks emerged around 465 cm^{-1} (Si–O–Al), 516 cm^{-1} (Si–O–Mg), and 465 cm^{-1} (Si–O–Mg) when Ag NPs were coated with bentonite). The stretching vibration of Si–O was also attributed to the bands at 1020 and 770 cm^{-1}, which was typically considered as evidence for a three-dimensional amorphous silica phase (Yang et al.,2007). The band at 682 cm^{-1} was due to Al–OH, while (Al, Mg)–

OH caused the band at 770 cm^{-1}. Si–O–Si bending vibration was attributed to the band between 520 and 459 cm^{-1} (Alemdar et al., 2005). The characteristic Ag NPs peak seen at 460 cm^{-1} was symmetric with Si-O-Al. The band observed in the region of 1413-1635 cm^{-1} in both composite reveals that the leaves extract and silver precursor was successfully incorporated with the produced nanoclay. These results confirmed that the increased amounts of Ag NPs in the Ag-Bent NC at 3438 cm^{-1} broad peak was observed due to the presence of van der Waals interactions between the hydroxyl groups of MMT layers and the partial positive charge on the surface of Ag-NPs (Yang et al., 2010).

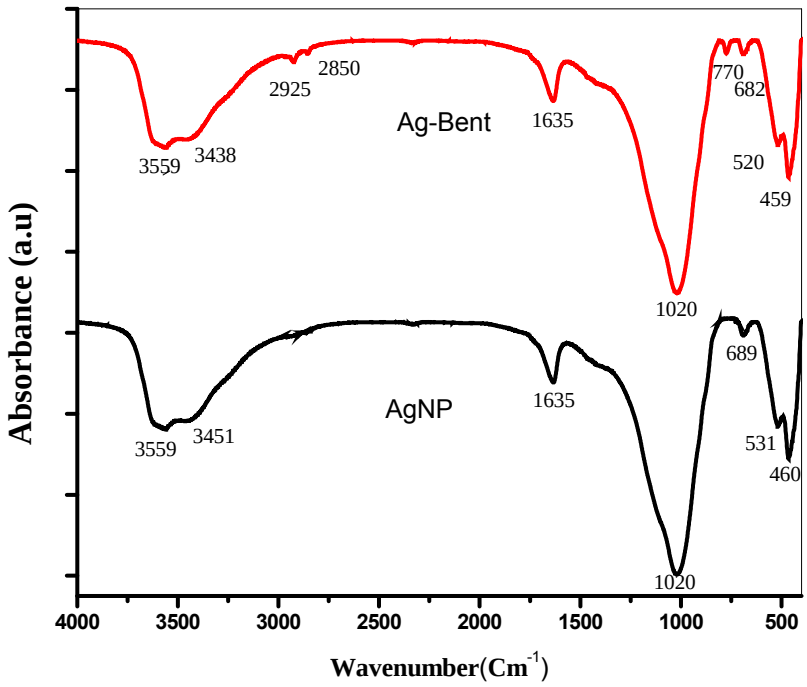

Figure 32: FTIR spectra of Ag NPs and Ag-Bent NCs

5. ANTIBACTERIAL ACTIVITY ANALYSIS BY DISC DIFFUSION METHODS

5.1. Antibacterial Activity Analysis Results of ZnO NPs and ZnO/Bentonite

This method consists of placing paper discs saturated with antimicrobial agents on a neighbourhood of bacteria seeded on the surface of an agar medium, incubating the plate overnight, and measuring the presence or absence of a zone of inhibition around the discs (Figure 33). The antibacterial activity of the targeted sample was evaluated by measuring the zone of inhibition against the test organisms.

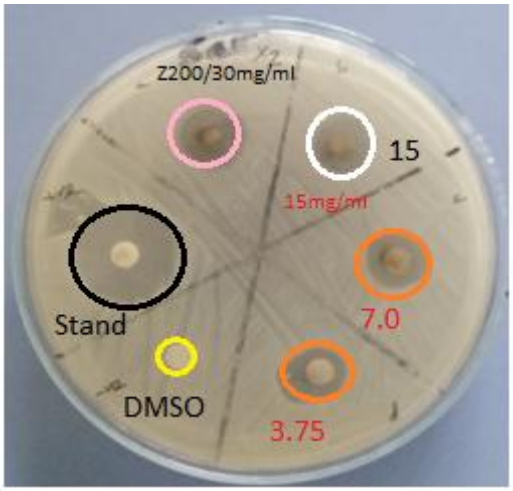

Figure 33: The zone of inhibition measured for a sample at different concentrations

The antibacterial activities of 5%Na-Bentonite and leaf extract with concentration of 3.75 mg/mL to 30 mg/mL against *E. coli* ATCC 25922 and *S. aureus* ATCC 25923 are illustrated using figures 34 a & b. The results revealed that 5% activated bentonite (Na-Bent) exhibited more pronounced zone of inhibition at high concentration, 30 mg/mL, 8±0.3 and 7±0.3 *E. coli* ATCC 25922 and *S. aureus* ATCC 25923 and lowered to 6.6±0 and 6.4±0 at 3.75mg/mL respectively. The review conducted by (Metge et. al., 2009 and Moosavi, 2017) found the strong antibacterial activity of aqueous suspension of clay in killing a broad spectrum of bacteria, and modified montmorillonites have also shown strong antibacterial effect and these antibacterial effects might result from physical interaction, penetration or splitting of the cell and chemical interaction of the clay with bacteria that is poisoning or nutrient withdrawal)

(Moosavi, 2017, Krishnan and Mahalingam, 2017, Pourabolghasem et al., 2017, Guo et al., 2020, Rapacz-kmita et al., 2017, Hu and Xia, 2006, Meng et al., 2009).

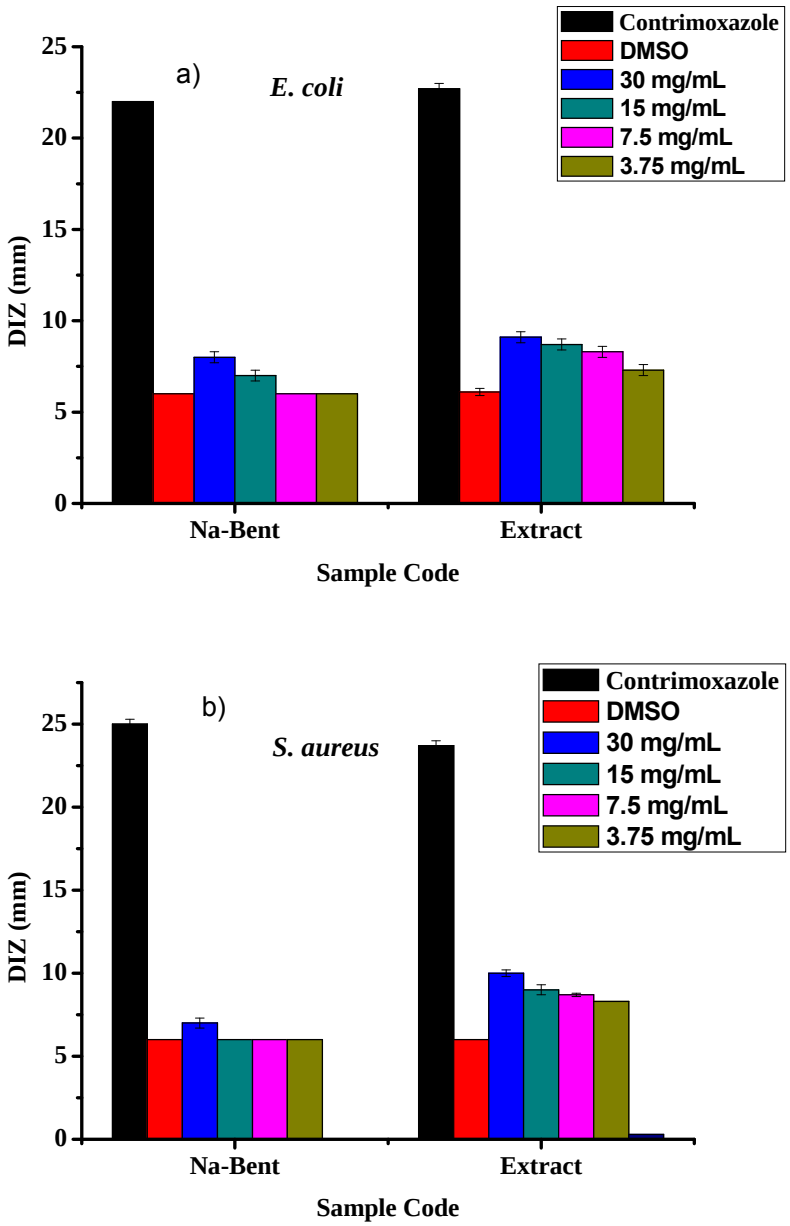

Figure 34 (a & b): Zone of inhibition of 5% Na-Bent and Aqueous extract of *H. abyssinica* at different concentration against *E. coli* and *S. aureus* bacterial strain.

According (Cohn et al., 2006) the bactericidal action of mineral is due to the presence of iron in the mineral sample, and the antibacterial activity observed at different mass ratios of bentonite suspensions

in distilled water of 5% Na activated bentonite results observed in this work might be due to the presence of (7-8%) iron oxide obtained from compositional analysis as indicated in table 11. The reaction between iron (Fe^{2+}) and hydrogen peroxide (a product of mitochondrial oxidative respiration) resulted with ferric iron (Fe^{3+}) and hydroxyl radical. The generated hydroxyl radical damaged iron-sulfur (Fe–S) clusters in the electron transport chain of bacteria (Zholobak et al., 2016). At the same time the plant extract has an effect with the inhibition zone and the results were more pronounced on Gram-positive bacteria *(S. aureus)*. The maximum inhibition zone of plant extract toward *S. aureus* was 10±0.2 mm at 30 mg/mL and minimum 8.3±0.3 mm at 3.75 mg/mL. Whereas 9.1±0.3 mm at 30 mg/mL and 7.3 ± 0.3 mm at 3.75 mg/mL were the Maximum and minimum values respectively toward *E. Coli.* The antibacterial effect of plant extract can be attributed to the large number of different chemical compounds as listed in (table 1) and similar result was reported by (Akinduti et al., 2022). *E. coli* bacteria are more resistance against *H. abyssinica* plant leaf extract than *S. aureus* this may be due to the bacteria structural differences. The results indicated that, standard Contrimoxazole (Ct) has antibacterial activities within the range of 22±0 and 22.7 ± 0.3 and 25±0.3 and 23.7±0.3 for *E. coli* ATCC 25922 and *S. aureus* ATCC 25923 respectively. DMSO (DM) has no activity (6 mm) on both tested bacterial strain and it was used as solvent for serial dilution. The remaining antibacterial tests results of the synthesised samples depicted on (figures 35 a, b, c and d).

The antibacterial activity of ZnO NPs synthesized with different volume ratios of plant leaf extract (Z10, Z20, Z50, Z100, and Z250) were investigated against *E. coli* ATCC 25922 and *S. aureus* ATCC 25923. The feasible disc diffusion method was performed to assess the antibacterial properties of the NPs at various concentrations (30, 15, 7.5 and 3.75 mg/mL). The inhibition zone result of *E. coli* ATCC 25922 and S. *aureus* ATCC 25923 are depicted on the figures 35 (c & d). The results show that ZnO NPs

exhibited considerable antibacterial activities against both bacteria even at low concentration, 3.75 mg/mL for ZnO synthesized with 10 mL volume of leaf extract and 100 mL of 0.2M $Zn(AC)_2$ (Z10). The antibacterial activity of ZnO NPs (denoted Z200 and Z10) has inhibition zone between 12.3 ± 0.3 to 8.0 ± 0.1 mm and 12 ± 0.6 to 7.7 ± 0.2 mm for *E. coli* ATCC 25922 and *S. aureus* ATCC 25923 at 30 mg/mL and 7±0.3 to 6.3±0, and 6.5±0 to 6.2±0 at 3.75 mg/mL concentration respectively. Both bacterial strains have moderate sensitivity toward ZnO NPs and the measured zone of inhibition affected by the concentration of the ZnO NPs suspension and the extract volume ratios used for the synthesis of the nanoparticles. ZnO NPs like Z200 which synthesized with 100 mL 0.2M of zinc acetate by taking 200 mL of leaf extract prepared (by dissolving 25 gm powder in 400 mL distilled water) while Z10 NPs was prepared (using100 mL of 0.5M of the same salt and 10 mL of extract). The inhibition zone of Z200 is larger than Z10, for both strains because of the smaller average crystallite size of Z200 (13.3 nm) over the Z10 (28.7 nm). The reasons behind Z200 NPs activities toward these bacteria are due to the ability of small particles to penetrate bacterial cell walls. The strong antimicrobial action of Z200 NPs is related to its nano-scale size and ZnO properties (Kukushkina et al., 2021, Naqvi et al., 2019). According to other groups the effectiveness is not only limited to the nanoscale size, but also the reactivity of the NPs towards bacteria DNA or amino acids. The increase in permeability of cell membranes, produce reactive oxygen species, and interrupt replication of deoxyribonucleic acid by releasing zinc ions (Yin et al., 2020) and the concentration of the NPs increase the Zn ions released to the bacterial cell. The existing results confirmed the NPs dose dependence of antibacterial activity.

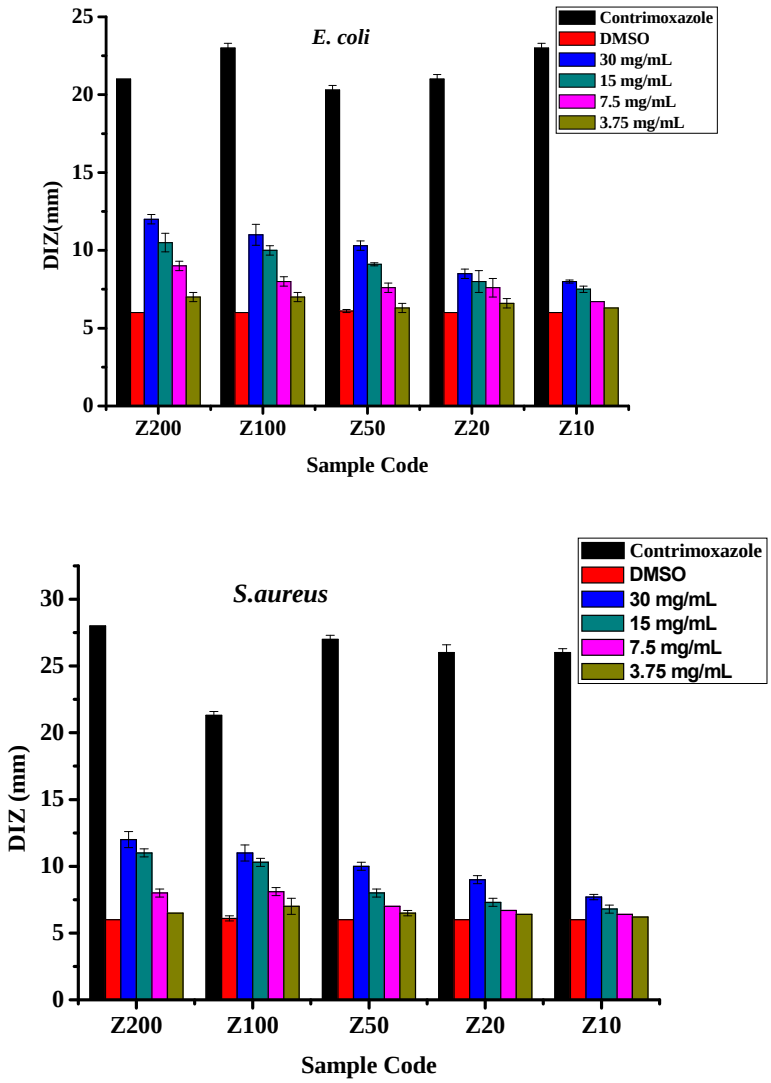

Figure 35 (a & b): Zone of inhibition of synthesized ZnO NPs at different concentration against *E. coli* and *S. aureus* bacterial strain

This suggests that the inhibition zone increased with concentration of ZnO NPs. The release of ions (Espitia et al., 2012), the interaction of NPs with microorganisms (Lin et al., 2018), and the formation of ROS by the effect of light radiation are the different possible mechanisms for NPs to be an antibacterial (Dobrucka and Długaszewska, 2016. Espitia et al., 2012 reported the release antimicrobial ion of metal oxides is dependent on different factors such as the concentration of metal oxides, time of interaction, and the nature of microorganisms. ZnO nanoparticles cause disruption of bacterial membranes probably

by the production of reactive oxygen species, such as superoxide and hydroxyl radicals. Moreover, the antibacterial activity is reported to be dependent on the concentration of ZnO nanoparticles and the impact of the type of support materials used (Buzuayehu et al. 2021). A comparison of zone of inhibition values shows a larger zone of inhibition for Gram-positive bacteria (*S. aureus* ATCC 25923) than that of Gram- negative (*E. coli* ATCC 25922) bacterial strain toward standard and different dosage of ZnO NPs. The observed better inhibition zones shows that the synthesized ZnO NPs disrupt the membrane with high rates of surface oxygen species generation and finally cause the death of pathogens (Motshekga et al.,2013). ZnO shows good antibacterial property on both gram-positive and gram-negative bacteria. But, the results more pronounced against gram-positive this is might be due to the bacterial structure mentioned above.

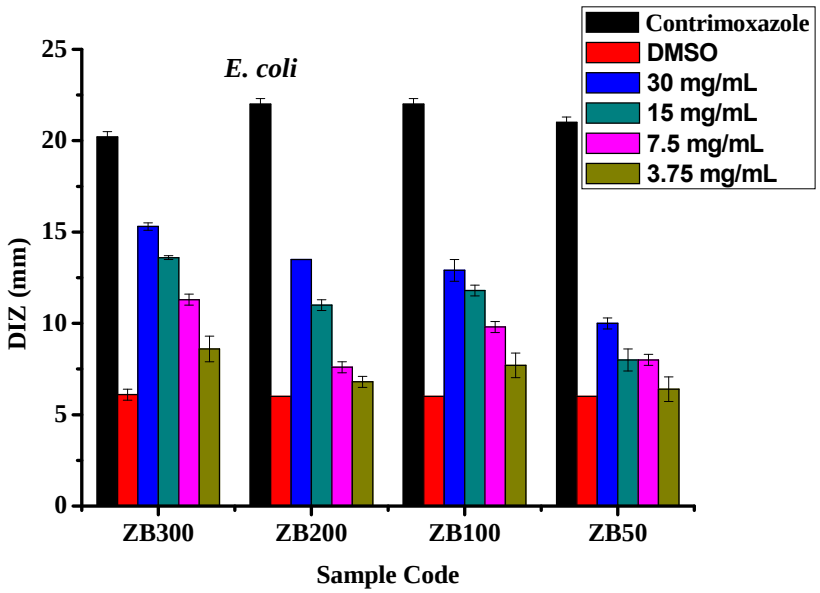

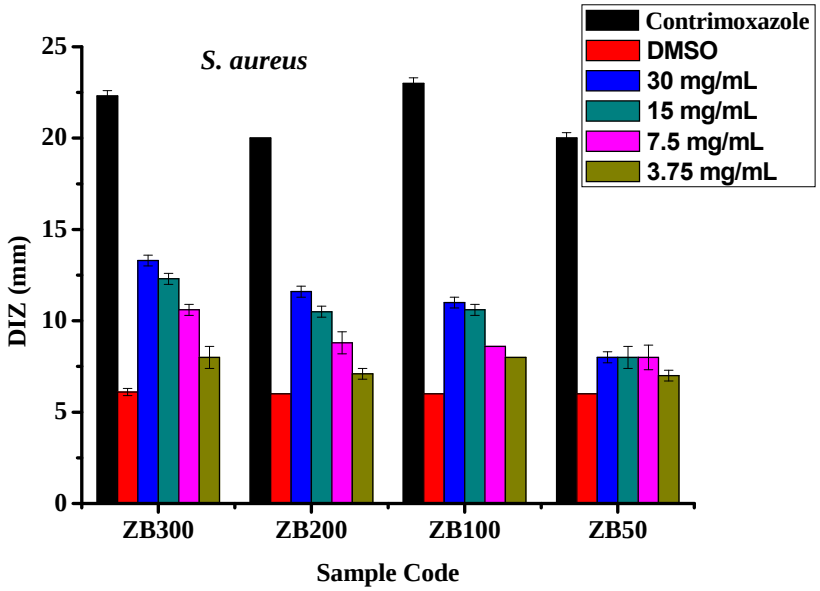

Figure 35 (c & d): Zone of inhibition of synthesized ZnO/Bentonite nanocomposites at different concentration against *E. coli* and *S. aureus* bacterial strain.

The antibacterial analysis of composites denoted ZB300, ZB200, ZB100 and ZB50) showed good antibacterial property. The inhibition zone results of ZB300, ZB200, ZB100 and ZB50 are 15.3 ± 0.2 mm, 13.5±0 mm, 12.9±0.6 mm, and 10±0.3 mm at 30 mg/mL, against *E. coli* ATCC 25922 and 13.3 ±0.3 mm, 11.6±0.3 mm, 11±0.3 mm and 8±0.3 against *S. aureus* ATCC 25923. In this case moreover the bactericidal efficiency are size-dependent of the nanocomposites (Naqvi et al., 2019). The size allows the composites for better penetration and interaction with the bacteria, disrupting the cell membrane (Pouraboulghasem et al., 2016). The results revealed with concentration the inhibition zone of each respective composite ZB300 to ZB50 also increased on both strains under investigations. This is the consequence of high antibacterial materials exposure, resulted with greater inhibition zones. The ZB 300 antibacterial suspensions results: 15.3 ± 0.2 mm and 13.3 ±0.3 mm for *E. coli* ATCC 25922 and *S. aureus* ATCC 25923 at 30 mg/ML and 8.6 ± 0.7 mm and 8 ± 0.6 for 3.75mg/mL and similarly results are reported by (Dejen et al., 2020). The main objective of combining ZnO NPs, and Na-Bent to develop composite with the better antibacterial to target both Gram-negative (*E. coli*) and Gram-positive (*S. aureus*) bacteria. The investigation results of this work also support the better competence of the nanocomposite antibacterial material and related works were reported by (Pouraboulghasem et al., 2016, and Dahonog et al 2019) for transition metal and metal oxide bentonite against antibacterial activity *E.*coli and *S.* Aureus. The enhanced antibacterial activity of the composites can be attributed to chemical

and physical properties of the nanoparticles together with the large surface area of the Na-AB. This means a large amount of nanoparticles were highly dispersed per unit area of the bentonite surfaces, thus, maximizing antibacterial activity. In such combinations, nanoparticles are largely attached on bentonite surfaces which ensure uniform dispersion, and reduced the nanoparticles tendency to agglomerate. Smaller size ZnO NPs kill bacteria more effectively in dark conditions and enhanced antibacterial activity will be achieved in the presence of UV light due to the increased production of ROS from the ZnO NPs (Zholobak et al., 2016). The smaller ZnO NPs have greater surface reactivity and easier cell penetration that released Zn^{2+} which might be bind to proteins and deactivate proteins, interact with bacterial membrane and causing structural changes, and bind to electron donor groups in biological molecules containing sulphur, oxygen or nitrogen like nucleic acids and prevent microbial replication. The antibacterial activity of ZnO was also attributed the reactions between ZnO surface and water, and the aqueous ZnO NPs suspensions are able to produce high levels of ROS species (OH^-, O_2^{-2}, H_2O_2) (Jiang et al., 2016, Slavin et al., 2017, Sivakumar et al., 2018). The antibacterial activity was mainly attributed to both the production of ROS and the accumulation of NPs in the cytoplasm or on the outer membranes. The table 9 below also can summarize the effects of different developed antibacterial agents of Zinc oxide NPs, ZnO-Bentonite NCs, purified bentonite and plant leaf extract with different concentrations on the selected bacteria strain

Table 9: The zone of inhibition in mm for extract,Na-Bent, synthesized ZnO NPs and ZnO/Bent NCs

NPs/NCs	Organisms	30mg/mL	15mg/mL	7.5mg/mL	3.75mg/mL	Contrimoxazole (+ve)	DMSO (-ve)
Z200	E. coli	12±0.3	10.5±0.6	9±0.3	7±0.3	21±0	6 ± 0
	S. aureus	12±0.6	11±0.3	8±0.3	6.5±0	28±0	6 ± 0
Z100	E. coli	11±0.67	10±0.3	8±0.3	7±0.3	23±0.3	6 ± 0
	S. aureus	11 ± 0.6	10.3 ± 0.3	8.1 ± 0.3	7± 0.6	21.3±0.3	6 ± 0
Z50	E. coli	10.3 ± 0.3	9. 1 ± 0.1	7.6±0.3	6.3±0.3	20.3±0.3	6 ± 0
	S. aureus	10±0.3	8±0.3	7±0	6.5±0.2	27±0.3	6 ± 0
Z20	E. coli	8.5±0.3	8±0.7	7.6±0.6	6.6±0.3	21±0.3	6 ± 0
	S. aureus	9±0.3	7.3±0.3	6.7±0	6.4±0	26±0.6	6 ± 0
Z10	E. coli	8±0.1	7.5±0.2	6.7±0	6.3±0	23±0.3	6 ± 0
	S. aureus	7.7±0.2	6.8±0.3	6.4±0	6.2±0	26±0.3	6 ± 0
ZB300	E. coli	15.3 ± 0.2	13.6±0.1	11.3±0.3	8.6 ± 0.7	20.2 ± 0.3	6 .1 ± 0.3
	S. aureus	13.3 ±0.3	12.3±0.3	10.6 ± 0.3	8 ± 0.6	22.3±0.3	6 .1 ± 0.2

ZB200	E. coli	13.5±0	11±0.3	7.6±0.3	6.8±0.3	22±0.3	6 ± 0
	S. aureus	11.6±0.3	10.5±0.3	8.8.±0.6	7.1±0.3	20±0	6 ± 0
ZB100	E. coli	12.9±0.6	11.8±0.3	9.8±0.3	7.7±0.67	22±0.3	6 ± 0
	S. aureus	11±0.3	10.6±0.3	8.6±0	8±0	23±0.3	6 ± 0
ZB50	E. coli	10±0.3	8±0.6	8±0.3	6.4±0.67	21±0.3	6 ± 0
	S. aureus	8±0.3	8±0.6	8±0.67	7±0.3	20±0.3	6 ± 0
Na-Bent	E. coli	8±0.3	7±0.3	6±0	6±0	22±0	6 ± 0
	S. aureus	7±0.3	6±0	6±0	6±0	25±0.3	6 ± 0
Extract	E. coli	9 .1 ± 0.3	8.7 ± 0.3	8.3 ± 0.3	7.3 ± 0.3	22.7±0.3	6 .1 ± 0.2
	S. aureus	10± 0.2	9± 0.3	8.7± 0.1	8.3± 0.3	23.7±0.3	6 ± 0

5.1.1. MIC and (MBC) of ZnO/Bentonite Nanocomposites

In this work, ZnO/Bentonite nanocomposite (ZB300), showed better antibacterial activities against both *Staphylococcus aureus* (ATCC 25923) and *Escherichia coli* (ATCC 25922) when it was compared with the components of the composite, especially for *Staphylococcus aureus* (ATCC 25923). The sensitivity of *S. aureus* toward this nanocomposite is better than *E. coli* is due to Gram–negative bacteria has a thin layer with an additional outer membrane, which makes it resistance than Gram-positive (Slavin et al., 2017, Sivakumar et al., 2018). The MIC observed for composites were 6.25 $x10^2$ μgmL^{-1} and 78.125 μgmL^{-1} for *Escherichia coli* ATCC 25922 and *Staphylococcus aureus* ATCC 25923 respectively. The MBC observed the same material were 1.25 $x10^3$ μgmL^{-1} and 156.25 μgmL^{-1} for *Escherichia coli* ATCC 25922 and *Staphylococcus aureus* ATCC 25923 respectively. The results observed that the *Staphylococcus aureus* were most sensitivity against composite of zinc oxide –bentonite (ZB300).

Table 10: MIC (μgmL^{-1}) and MBC (μgmL^{-1}) of nanocomposites for *E. coli* and *S. aureus* bacterial strain

Sample	Bacterial strain	Strain no	MIC (μgmL^{-1})	MBC(μgmL^{-1})
AB300	*E. coli*	ATCC 25922	6.25 $x10^2$	1.25 $x10^3$
	S. aureus	ATCC 25923	78.125	156.25

5.2.Antibacterial Activity Analysis Results of Ag NPs and Ag-Bentonite

In this section, *H. abyssinica* plant extract synthesized different Ag NPs and Ag-Bent NCs samples in the concentration range of 10- 1.25µg/ml, were tested for antibacterial activity using gram-negative and gram-positive bacteria strains of *Escherichia coli* and *Staphylococcus aureus* using disc diffusion method. Ciprofloxacin was used as positive control.

5.2.1. Antibacterial activity of AgNPs

The results obtained are summarized with the diameter of inhibition zones (in millimetres) measured as shown in Table 11 and figure 36. The clear zone diameter of the bacterial inhibition zone was correlated to antibiotic activity for gram-positive and gram-negative bacteria. The presence of an inhibition zone clearly indicates the antibacterial effect of the nanoparticles. The antibacterial activity results showed that Ag NPs have significant antimicrobial activity against the tested pathogenic organisms. The results specify that Ag NPs synthesized using different ratios of leaf extract showed enhanced antibacterial activities. The impact of the leaf extract volumes used for the synthesis of Ag NPs observed on the antibacterial activities indicated on the figure30 b. Here, the same concentration of Ag NPs (10 mg/ mL) suspensions prepared from A25 and A400 resulted with 11 ± 0.6 mm and 19 ± 0.3 mm zone of inhibitions against gram-positive bacteria strains of *Staphylococcus aureus*, and 10.3 ± 0.3 mm and 13 ± 0.3 mm gram-negative bacteria strains of *Escherichia coli* using disc diffusion method. The bactericidal activity of Ag NPs was influenced by the volume of plant extract used for the synthesis. This results are consistent with earlier reported studies (Christidis et al., 2006, Doulia et al., 2009, Keller-Besrest et al., 1994).

All synthesized Ag NPs A25, A50, A100, A200 and A400 tested for antibacterial activity showed high activity against *S. aureus* bacteria with inhibition zone of 11 ± 0.6 nm, 12.3 ± 0.3 nm, 14.3 ± 0.3 nm, 18 ± 0 nm and 19 ± 0 .3 nm when compared to *E. coli* bacteria with 10.3 ± 0.3 nm, 12.3 ± 0.3 nm, 11.6 ± 0.3 nm, 14 ± 0.3 nm and 13 ± 0.3 nm respectively, in comparison to standard antibiotics. It is assumed that the incorporation of silver nanoparticles into the membrane structure occurs and causing cell death (Meng et al., 2009).

The crystallites sizes of the bio-synthesized Ag nanoparticles estimated are in the range of 9-12 nm, which is very small, having larger surface atoms available for interaction, and will have a stronger bactericidal effect. Hence, Ag NPs are able to penetrate the bacteria and cause further damage, possibly by interacting with sulphur- and phosphorus-containing compounds such as DNA(Hu and Xia., 2006). Yuet Yind *et al* reported that the smaller size of Ag NPs could cause more toxicity to the bacteria and show better bactericidal effect compared to the larger particles as they have larger surface area (Park and Jang., 2003). Because of their small size, Ag NPs can easily adhere to the cell wall and penetrate into the bacteria cell, which in turn improves their antibacterial activity (Park and Jang., 2003). This could be the reason why these nanoparticles have the best antibacterial effect. The mechanism of action of the antimicrobial activity of silver nanoparticles is based on their penetration in the bacteria cell and reaction with thiol and phosphate groups that are present in membrane proteins or enzymes. Therefore, silver nanoparticles bind to the cell membrane inhibiting cellular respiration and leading to cell death.

Table 11. Antibacterial activity of Ag NPs synthesized using *H. abyssinica* plant extract

Types of NPs/NCs and Bacteria Strain		Mean of three replications and Standard error (±SE) of Inhibition zones in mm for different concentrations					
NPs/NCs	Bacteria Strain	10 mg/mL	5 mg/mL	2.5 mg/mL	1.25 mg/mL	Contrimoxazole (+ve)	DMSO (-ve)
A25	*E. coli*	10.3 ± 0.3	10.1 ± 0.3	7.6 ± 0.3	6.3 ± 0.3	20.3 ± 0.3	6 .1 ± 0.1
	S. aureus	11 ± 0.6	10.3 ± 0.3	8.1 ± 0.3	7 ± 0.6	21.3 ± 0.3	6 .1 ± 0.2
A50	*E. coli*	12.3 ± 0.3	10.6±0.3	8.3 ± 0.3	6.6 ± 0.7	20.2 ± 0.3	6 .1 ± 0.3
	S. aureus	12.3 ±0.3	11.3±0.3	8.6 ± 0.3	7 ± 0.6	22.3 ±0.3	6 .1 ± 0.2
A100	*E. coli*	11.6 ± 0.3	11.3 ± 0.3	11 ± 0.6	10.3 ± 0.3	20.3 ± 0.3	6 ± 0
	S. aureus	14.3 ± 0.3	13.3 ± 0.3	13 ± 0.3	11.3 ± 0.3	21.3 ±0.3	6 ± 0
A200	*E. coli*	14 ± 0.3	14 ± 0.3	12 ± 0.3	12 ± 0.3	20 ± 0.3	6 ± 0
	S. aureus	18 ± 0	18 ± 0.3	18 ± 0.6	16 ± 0.3	24 ± 0	6 ± 0
A400	*E. coli*	13 ±0.3	12 ± 0.6	11 ± 0.3	10 ± 0.3	23 ± 0.6	6 ± 0
	S. aureus	19 ± 0.3	18 ± 0.6	15 ± 0.3	13 ± 0.67	24 ± 0.3	6 ± 0

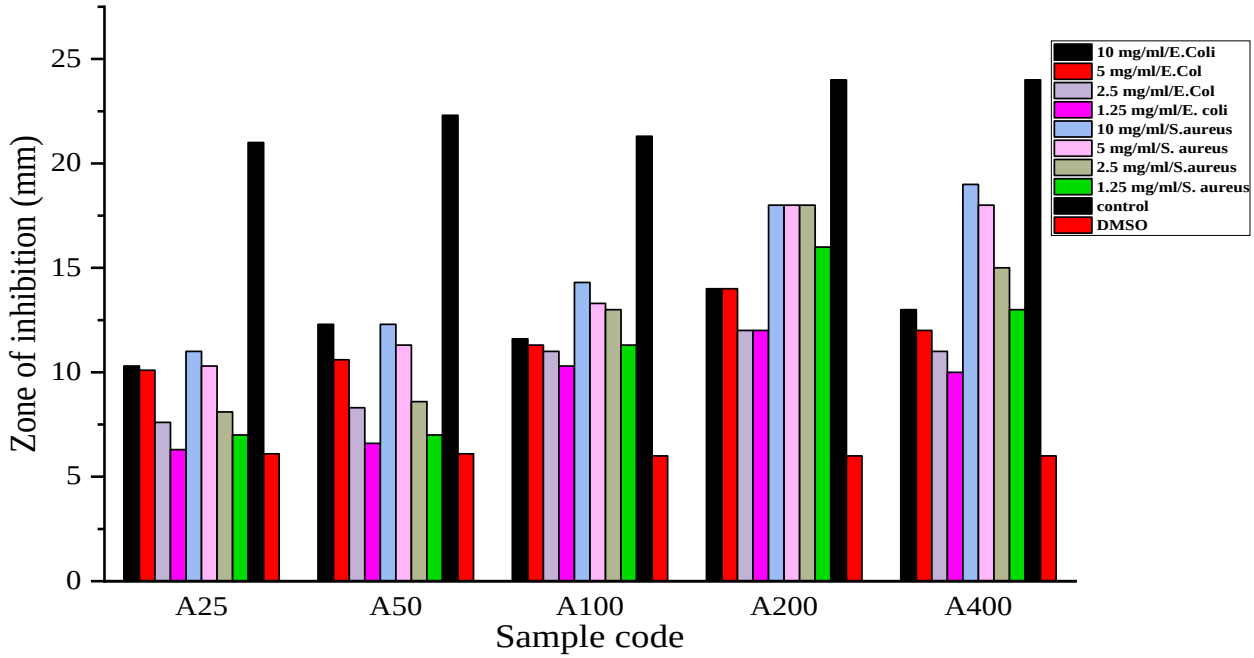

Figure 36: Zone of inhibition of synthesized Ag NPs with different extract volume against *E. coli* and *S. aureus* bacterial strain

5.2.2. Antibacterial activity of Ag-Bentonite Nanocomposite

Figure 30 in section 5.1 shows strong zone of inhibition for 5% Na-Bent and Aqueous extract of *H. abyssinica* at different concentration against *E. coli* and *S. aureus* bacterial strain. The inhibition zone values obtained for the low temperature synthesized composites of Ag-Bent showed excellent antibacterial property against *E. coli* and *S. aureus* bacteria. The presence of an enhanced inhibition zone presented on (Figure 37 and table 12) the excellent antibacterial property of the nanocomposites. Table 12 data shows that Ag-Bent (AB01: 18 ± 0 and 15 ± 0.3) showed high and remarkable antibacterial activity against *S. aurous* bacteria better than Ag-Bent (AB005: 16 ± 0 and 15 ± 0.3) and AB02: 14.7 ± 0.3 and 14.3 ± 0.1), and demonstrated more or less the same inhibition zones against and *E. Coli strain.*

The bactericidal effect of Ag nanoparticles in the composites can be explained by their nano-scale size and its distribution in the matrix of the bentonite clay. That exhibits pronounced bactericides towards a broad range of microorganisms. Thus, AB01 composite (synthesized with 0.1 M $AgNO_3$) had good mono dispersed Ag nanoparticles in the matrix of bentonite and its interaction with the targeted bacteria caused cellular inactivation and disrupting the cell membrane which leads to cell death over AB02 (0.2M) and (0.005M). Furthermore, a combination of the three antibacterial materials: *H. abyssinica* leaf plant extract, sodium carbonate activated bentonite and Ag NPs synergistic effect results in an excellent antibacterial activity composites(Hernández-Sierra *et al., 2008)*[181]. Antibacterial activity of the composites can be attributed to chemical and physical properties of the nanoparticles together with the large surface area of the clay. In such combinations, nanoparticles are largely attached on bentonite surfaces which ensure uniform dispersion, tend to reduce agglomeration and enhance the properties of the composites (Karimi and Salem, 2011, (Hernández-Sierra et al., 2008). The release of ions including Ag^{+}, Si^{4+}, Al^{3+}, and Mg^{2+} from the nanocomposite are accountable for the exhibited antibacterial property of the materials. Under normal environment, bacterial cell walls are negatively charged due to the presence of carboxyl, hydroxyl, and phosphate groups in lipid bi-layer at the cell surface. All released cations from the nanocomposite bind to the above groups that inhibit the normal metabolism of the cellular processes (Meng et al., 2009, Hu and Xia., 2006). This may be the reason for a promising antibacterial activity exhibited by the Ag -bentonite clay nanocomposites (Mohanraj and Chen, 2007). The different sensitivities of gram positive and gram-negative bacteria could be due to the different polarities of their cell membrane. This would allow a higher level of penetration of negatively charged free radicals such as, superoxide radical anions and peroxide ions, causing *S. aureus* damage and cell death at lower concentrations than those required to damage *E. coli*.

Table 12.Antibacterial activity of Ag-Bentonite nanocomposites

Types of NPs	Bacteria Strain	Mean of three replications and Standard error (±SE) of Inhibition zones in mm for different concentrations					
NPs/NCs	Bacteria Strain	10 mg/mL	5 mg/mL	2.5 mg/mL	1.25 mg/mL	Contrimoxazole (+ve)	DMSO (-ve)
AB005	*E. coli*	15 ± 0.3	15 ± 0.6	12 ± 0.3	10 ± 0.7	20 ± 0.3	6 ± 0
	S. aureus	16 ± 0	15 ± 0.3	14 ± 0.67	13 ± 0.3	24 ± 0.3	6 ± 0
AB01	*E. coli*	15 ± 0.3	14 ± 0.6	13 ± 0.67	10 ± 0.3	21 ± 0.3	6 ± 0
	S. aureus	18 ± 0	16.6 ± 0.3	16 ± 0.3	15 ± 0.67	22 ± 0.3	6 ± 0
AB02	*E. coli*	14.3 ± 0.1	13.3 ± 0.3	13 ± 0.6	12 .3 ± 0.0	20.2 ± 0.3	6 ± 0
	S. aureus	14.7 ± 0.3	13.7 ± 0.3	13.3 ± 0.3	12.3 ± 0.3	21.3 ± 0.3	6 ± 0

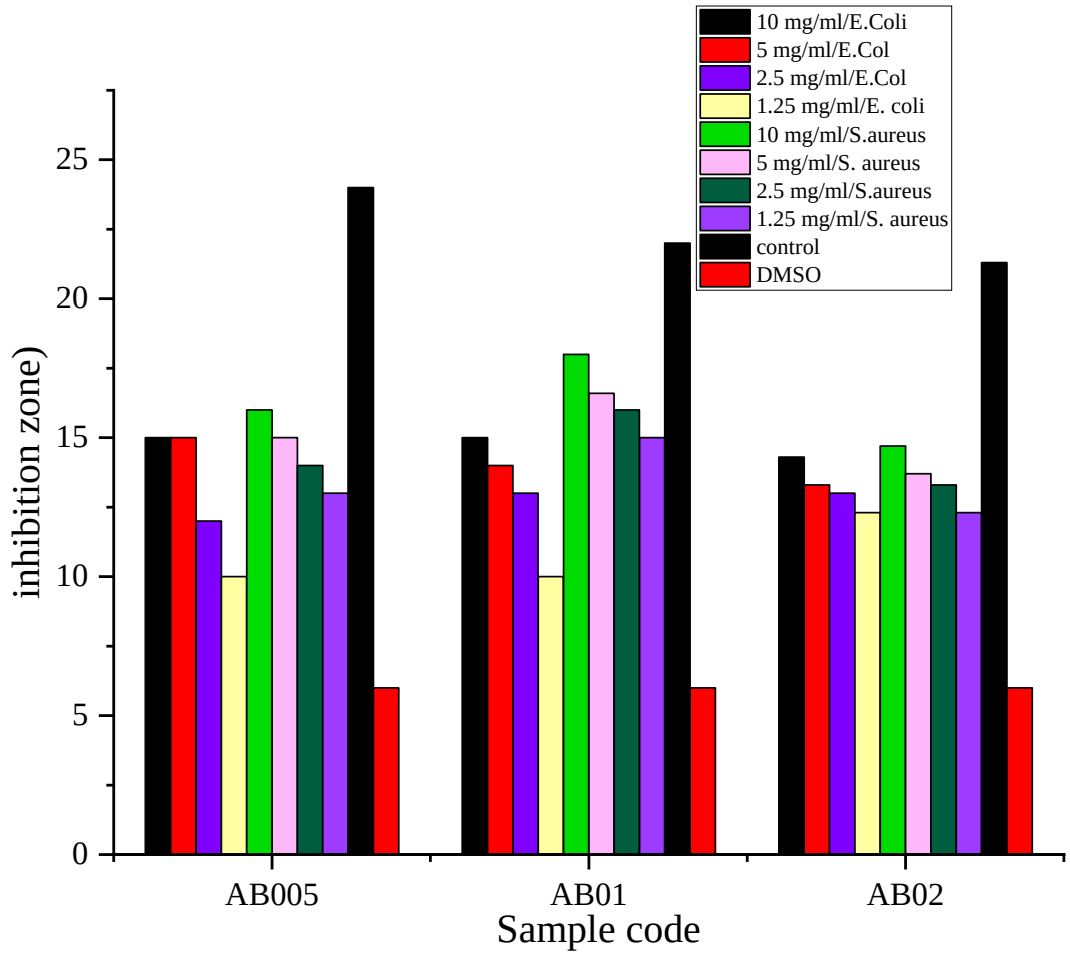

Figure 37: Zone of inhibition of synthesized Ag-Bentonite nanocomposite with different $AgNO_3$ concentration against *E. coli* and *S. aureus* bacterial strain

5.2.3. MIC and MBC of Ag/Bentonite Nanocomposites

The results of the antibacterial effects of Ag/Bentonite nanocomposite(AB01) and (AB02) against selected bacterial via the MIC and the MBC are summarized in Table 13. The bactericidal effect of nanocomposite is dependent on the concentration of nanocomposites and the initial bacterial concentration. In this work, Ag/Bentonite nanocomposite showed better antibacterial activities against both *Staphylococcus aureus* (ATCC 25923) and *Escherichia coli* (ATCC 25922) when it was compared with the components of the composite, especially for *Staphylococcus aureus* (ATCC 25923).The sensitivity of *S. aureus* toward this nanocomposite than *E. coli* is due to its thin membrane layers consisting of lipopolysaccharide.

Table 13: MIC (μgmL^{-1}) and MBC (μgmL^{-1}) of nanocomposites for *E. coli* and *S. aureus* bacterial strain

Sample	Bacterial strain	Strain no	MIC (μgmL^{-1})	MBC(μgmL^{-1})
AB01	*E. coli*	ATCC 25922	78.125	156.25
	S. aureus	ATCC 25923	39.0625	78.125
AB02	*E. coli*	ATCC 25922	312.5	6.25×10^2
	S. aureus	ATCC 25923	156.25	312.5

6. CONCLUSION AND RECOMMENDATION

In this study, ZnO NPs, Ag NPs, ZnO/Bentonite NCs, and Ag/Bentonite NCs were successfully synthesized using *H. abyssinica* leaf extract for antibacterial investigations. TGA analysis of biosynthesized ZnO NPs and ZnO-bentonite NCs showed their respective thermal stability above 500 °C and 650 °C temperatures. The crystal structures of the nanoparticles ZnO (wurtzite) and Ag NPs (FCC); nanocomposites of ZnO/Bentonite mixed phases of (ZnO and MMT) and Ag/Bentonite (Ag NPs and MMT) were determined by XRD, SAED and HRTEM. In this work the effects of using excess volume of *H. abyssinica* leaf extract were observed in the synthesis of pure phase Ag NPs and better antibacterial agent of ZnO/Bentonite nanocomposites. The optical absorption of the ZnO/Bentonite nano nanocomposite in the UV region (273-285 nm) is quite high and this aspect highlights the applications of these composites in UV shielding. The investigation results revealed that the low temperature bio-synthesized Ag NPs and Ag/Bentonite are a promising bactericide agent over ZnO NPs and ZnO/Bentonite nanocomposites synthesized at high temperatures. Hence, from the results obtained we recommend the investigation of the formulations and applications of Ag-Bentonite suspension for disenfctant and ZnO-Bentonite for body lotio, and additional studies on the of the leaching effect of Ag & Zn ions from Ag-Bentonite & ZnO-Bentonite.

REFERENCES

1. Aadnan, I., Zegaoui, O., Daou, I., Esteves da Silva, J.C.G. (2020): Synthesis and physicochemical characterization of a ZnO-Chitosan hybrid-biocomposite used as an environmentally friendly photocatalyst under UV-A and visible light irradiations. Journal of Environmental Chemical Engineering, 8: 104260.

2. Aguzzi *et al.*, (2014): Solid state characterisation of silver sulfadiazine loaded on montmorillonite/chitosan nanocomposite for wound healing. Colloids Surfaces B Biointerfaces, 113:152–157.

3. Ahmed, S., Ahmad, M., Swami, B. L., and Ikram, S. (2016): A review on plants extract mediated synthesis of silver nanoparticles for antimicrobial applications: A green expertise. *Journal of Advanced Research*, 7:17–28.

4. Ahmed, S., Saifullah, M., Ahmad, B. L., Swami, and Ikram, S.(2016): Green synthesis of silver nanoparticles using Azadirachta indica aqueous leaf extract. *Journal of Radiation Research Appied. Science*, 9(1): 1–7).

5. Ahmed. U.and Birnin-Yauri U. A, Analysis of Some Clay Samples from Yauri (Kebbi State), Goronyo, Munwadata and Atokonyo (Sokoto State), Nigeria, Nigerian Journal of Basic and Applied Sciences vol. 16 No. 2 December 2008

6. Ajith, P., Agnes, J., Sappani Muthu, M., Ambrose Rajkumar, M., Prem Anand, D.(2021): Synthesis and Characterization Studies of Pure ZnO and Bentonite Doped ZnO Nanocrystals, Journal of Emerging Technologies and Innovative Research (JETIR), 8(9):2021.

7. Akbar, N., Aslam, Z., Siddiqui, R., Shah, M.R., Khan, N.A.(2012): Zinc oxide nanoparticles conjugated with clinically-approved medicines as potential antibacterial molecules. AMB Express, 11: 104.

8. Akinduti, P. A., Emoh-Robinson , V., Obamoh-Triumphant , H. F., Obafemi1, Y. D., and Banjo, T. T. (2022): Antibacterial activities of plant leaf extracts against multi-antibiotic resistant Staphylococcus aureus associated with skin and soft tissue infections, BMC Complementary Medicine and Therapies, 22:47, https://doi.org/10.1186/s12906-022-03527-y

9. Al Ani, T., and Sarapää,O. (2018): Clay and clay mineralogy," Physical – Chemical Properties and Industrial Uses. Geologian Tutkuskeskus Espoo, 1:1-96.

10. Alemdar, A., Güngör, N., Ece, O. I. , and Atici, O.(2005): The rheological properties and characterization of bentonite dispersions in the presence of non-ionic polymer PEG. *Journal of Materials Sciene.*, 40(1): 171–177.

11. Allo, W. A., and Murray, H. H.(2004): Mineralogy, chemistry and potential applications of a white bentonite in San Juan province, Argentina. *Applied Clay Science*, 25: 237–243.

12. Alzahrani, E., and Ahmed, R.A.(2016): Synthesis of copper nanoparticles with various sizes and shapes: application as a superior non-enzymatic sensor and antibacterial agent. International Journal of Electrochemical Science, 11:4712–23.

13. Assefa, B., Glatzel, G., and Buchmann, C. (2010): Ethnomedicinal uses of Hagenia abyssinica (Bruce) J.F. Gmel. among rural communities of Ethiopia. *Jounal of Ethnobiol Ethnomed*, (6):1–10.

14. Auwal, M. S., Saka, S., Mairiga, I. A., Sanda, K. A., Shuaibu, A., and Ibrahim, A.(2014): Preliminary phytochemical and elemental analysis of aqueous and fractionated pod extracts of Acacia nilotica (Thorn mimosa). *Vetener Research forum an International. Q. J.*, 5(2): 95–100.

15. Awwad, A.M., Albiss, B., and Ahmad, A. L. (2014): Green synthesis, characterization and optical properties of zinc oxide nanosheets using Olea europea leaf extract. Adv. Materials Letters, 5(9): 520-524. https://doi.org/10.5185/amlett.2014.5575

16. Babaki, H., Salem, A.,and Jafarizad, A.(2008): Kinetic model for the isothermal activation of bentonite by sulfuric acid. *Material Chemistry and Physics.*108:263–268.

17. Bar, H., Bhui, D. K., Sahoo, G. P., Sarkar, P., Pyne, S., and Misra, A. (2009): Green synthesis of silver nanoparticles using seed extract of Jatropha curcas. *Colloids Surfaces A Physicochemical Engineering*, 348(1–3):212–216.

18. Bazbouz,M.B., and Russell, S. J. (2018):Cellulose acetate/sodium-activated natural bentonite clay nanofibres produced by free surface electro spinning, Journal of Materials Science, 53:10891–10909, https://doi.org/10.1007/s10853-018-2354-9

19. Bhardwaj, A. K., Sundaram, S., Yadav, K. K., and Srivastav, A. L. (2021). An overview of silver nano-particles as promising materials for water disinfection. *Environmental Technology and Innovation*, *23*:101721. https://doi.org/10.1016/j.eti.2021.101721

20. Brandelli, A., A.C. Ritter and F.F. Veras (2017): Antimicrobial Activities of Metal Nanoparticles, Metal Nanoparticles in Pharma 2017, pp 337–363.

21. Buzuayehu, A., Murthy, H C A., Enyew, A. Z., and Yeshaneh, A.(2021): Synthesis and characterization of ZnO/PVA nanocomposites for antibacterial and electrochemical applications. Inorganic and Nano-Metal Chemistry, 51(8):1127-1138. DOI: 10.1080/24701556.2020.1814338

22. Caglar, B., Afsin, B., Tabak, A., and Eren, E. (2009): Characterization of the cation-exchanged bentonites by XRPD, ATR, DTA/TG analyses and BET measurement. Chemical Engineering Journal, 149: 242–248. https://doi.org/10.1016/j.cej.2008.10.028.

23. Cakić, M., Glišić, S., Nikolić, G., Nikolić, G.M., Cakić, K., and Cvetinov, M. (2016): Synthesis, characterization and antimicrobial activity of dextran sulphate stabilized silver nanoparticles. Journal of Molecular Structures, 1110:156–61.

24. Cao *et al.*, (2014): Sutures modified by silver-loaded montmorillonite with antibacterial properties. Applied. Clay Scicenc, 93/94: 102–106.

25. Chakraborty, T., Chakraborty, A., Shukla, M., & Chattopadhyay, T. (2019): ZnO–Bentonite nanocomposite: an efficient catalyst for discharge of dyes, phenol and Cr(VI) from water. *Journal of Coordination Chemistry*, *72*(1): 53–68. https://doi.org/10.1080/00958972.2018.1560429

26. Chaudhuri, S. K., and Malodia, L. (2017). Biosynthesis of zinc oxide nanoparticles using leaf extract of calotropis gigantea: Characterization and its evaluation on tree seedling growth in nursery stage. *Applied Nanoscience (Switzerland)*, *7*(8): 501–512. https://doi.org/10.1007/s13204-017-0586-7

27. Chernousova, S.,and Epple, M.(2013): Silver as antibacterial agent: Ion, nanoparticle, and metal. Angew. Chemie - Int. Ed., 2(6),: 1636–1653.

28. Chernousova S.,and Epple, M. (2013): Silver as antibacterial agent: Ion, nanoparticle, and metal. Angewandte Chemie International Edition, 52: 1636–1653.

29. Christidis, G. E., Blum, A. E., and Eberl, D. D. (2006): Influence of layer charge and charge distribution of smectites on the flow behaviour and swelling of bentonites," *Applied Clay Science.*, 34: 125–138.

30. Christopher, J.S.G., Saswati, B., Ezilrani, P.S. (2015): Optimization of parameters for biosynthesis of silver nanoparticles using leaf extract of Aegle marmelos. Braz. Arch. Biol. Techn. 58 (2015): 702–710

31. Cohn, C., Laffers, R., Simon, S.R., O'Riordan, T., Schoonen, M.A.A.(2006): Role of pyrite in formation of hydroxyl radicals in coal: possible implications for human health. Particle and Fibre Toxicology, 3(16):16 10.1186/1743-8977-3-16

32. Colín-Luna, J. A., Zamora-Rodea, E. G., González-Brambila, M. M., Barrera-Calva, E., Rosas-Cedillo, R., Medina-Mendoza, A. K., and García-Martínez, J. C. (2018): Biodiesel production using immobilized lipase supported on a zirconium-pillared clay. Effect of the immobilization method. International Journal of Chemical Reactor Engineering, 16(11). https://doi.org/10.1515/ijcre-2017-0260

33. Cubillo, A.E., Pecharromán, C., Aguilar, E., Santarén, J., and Moya, J.S. (2006): Antibacterial activity of copper monodispersed nanoparticles into sepiolite. Journal of Material Science, 41:5208–12.

34. Dadi, R., Azouani, R., Traore, M., Mielcarek, C., and Kanaev, A. (2019): Antibacterial activity of ZnO and CuO nanoparticles against gram positive and gram negative strains. *Materials Science and Engineering C*, *104*(July): 109968.

35. Dahonog, L. A. et al (2019):, Antibacterial Activity of Plasma-Treated Cu/Bentonite Nanocomposites Journal of Physics: Conference Series, 1191 012057

36. Darvishi Cheshmeh Soltani, R., Jorfi, S., Ramezani, H., & Purfadakari, S. (2016). Ultrasonically induced ZnO-biosilica nanocomposite for degradation of a textile dye in aqueous phase. *Ultrasonics Sonochemistry*, *28*: 69–78. https://doi.org/10.1016/j.ultsonch.2015.07.002

37. Dejen, K.D., Zereffa, E.A., Murthy, H.C.A., and Merga, A.(2020): Synthesis of ZnO and ZnO/PVA nanocomposite using aqueous Moringa oleifeira leaf extract template: antibacterial and electrochemical activities. Reviews on Advanced Materials Science, 59: 464–476

38. Demirci, S., Ustaoğlu, Z., Yilmazer, G. A., Sahin, F., and Baç, N. (2014): Antimicrobial properties of zeolite-X and zeolite-A ion-exchanged with silver, copper, and zinc against a broad range of microorganisms. *Applied Biochemistry and Biotechnology*, 172(3): 1652–1662.

39. Demissie, M. G., Sabir, F. K., Edossa, G. D., and Gonfa, B. A. (2020). Synthesis of Zinc Oxide Nanoparticles Using Leaf Extract of Lippia adoensis (Koseret) and Evaluation of Its Antibacterial Activity. Journal of Chemistry, 2020.

40. Dobrucka, R., Długaszewska, J.(2016): Biosynthesis and antibacterial activity of ZnO nanoparticles using Trifolium pratense flower extract. Saudi Journal Biological Science, 23(4):517–23. Available from: http://dx.doi.org/10.1016/j.sjbs.2

41. Doulia, D., Leodopoulos, C., Gimouhopoulos, K.and Rigas, F.(2009): Adsorption of humic acid on acid-activated Greek bentonite. *Journal of Colloid Interface Sciecn.* 340: 131–141.

42. Dutta, P., and Wang, B. (2019). Zeolite-supported silver as antimicrobial agents. *Coordination Chemistry Reviews*, *383*:1–29. https://doi.org/10.1016/j.ccr.2018.12.014.

43. Edeoga, H. O., Okwu, D. E., and Mbaebie, B. O. (2005): Phytochemical constituents of some Nigerian medicinal plants. *African Journal of Biotechnolology*, 4(7):685–688.

44. El Miz, M., Akichoh, H., Berraaouan, D., Salhi, S., and Tahani, A. (2017): Chemical and Physical Characterization of Moroccan Bentonite Taken from Nador (North of Morocco). American Journal of Chemistry, 2017(4): 105–112. https://doi.org/10.5923/j.chemistry.20170704.01

45. El shatter, A., El-haddad, A., El-attaar, A., Abugharbi, M., and Soliman W. (2018):

Characterisation of the Egyptian Pliocene bentonite from the Sohag region for pharmaceutical use, Arabian Journal of Geosciences, 11:385–97. https://doi.org/10.1007/s12517-018-3691-3

46. Espitia, P.J.P., Soares, N., de F.F., Coimbra, J.S., dos, R., de Andrade, N.J., Cruz, R.S., Medeiros, E.A.A.(2012): Zinc Oxide Nanoparticles: Synthesis, Antimicrobial Activity and Food Packaging Applications. Food Bioprocess Technology, 5(5):1447–64.

47. Fernández, A. M., Baeyens, B., Bradbury, M., and Rivas, P. (2004): Analysis of the porewater chemical composition of a Spanish compacted bentonite used in an engineered barrier. Physics and Chemistry of the Earth. 29:105–118.

48. Fisseha, K. (2017): Modification of Bentonite Clay for Adsorption Enhancement for Congo Red Dye Removal from Textile Waste Water. MSc Thesis Addis Ababa University,2017.

49. Feyissa, T., Nybom, H., Bartish, I. V., and Welander, M. (2007): Analysis of genetic diversity in the endangered tropical tree species Hagenia abyssinica using ISSR markers," *Genet. Resour. Crop Evol*, 54(5):947–958.

50. Feyissa, T., Welander, M., and Negash, L(2005): Micropropagation of Hagenia abyssinica: A multipurpose tree. *Plant Cell. Tissue Organ Cult,* 80(2):119–127.

51. Franci, G., Falanga A., Galdiero, S., Palomba, L., Rai, M., Morelli, G., and Galdiero, M. (2015): Silver nanoparticles as potential antibacterial agents. Molecules, 20: 8856–74.

52. Froggett, S.J., Clancy, S.F., Boverhof, D.R.,,Canady, R.A. (2014): A review and perspective of existing research on the release of nanomaterials from solid nanocomposites. Particle and fibre toxicology 11:17

53. Fytianos, G., Rahdar, A., & Kyzas, G. Z. (2020): Nanomaterials in cosmetics: Recent updates. *Nanomaterials*, *10*(5):1–16. https://doi.org/10.3390/nano10050979

54. Galan, C. R., Silva, M. F., Mantovani, D., Bergamasco, R., and Vieira, M. F.(2018): Green synthesis of copper oxide nanoparticles impregnated on activated carbon using Moringa oleifera leaves extract for the removal of nitrates from water. *Canandian Journal of Chemical Engineering*, 96(11): 2378–2386.

55. Ghorbanpour, M., and Lotfiman,, S. (2016):Solid-state immobilisation of titanium dioxide nanoparticles onto nanoclay, Micro and Nano Letters, DOI: 10.1049/mnl.2016.0259.
56. Guo *et al.*, H.(2020): Bioresource Technology Bene fi cial e ff ects of bacterial agent / bentonite on nitrogen transformation and microbial community dynamics during aerobic composting of pig manure," *Bioresources Technolology*, 298: 122384.
57. Gupta, M., and Kumar, A. (2018): Comparison of Minimum Inhibitory Concentration (MIC) value of statin drugs: A Systematic Review. *Anti-Infective Agents*, *17*(1): 4–19. https://doi.org/10.2174/2211352516666180629124433
58. Hayati-Ashtiani ,M., and Azimi, H. (2016): Characterization of different types of bentonites and their applications as adsorbents of Co(II) and Ni(II), *Desalin. Water Treat.*, vol. 57, no. 37, pp. 17384–17399, 2016.
59. Hernández-Sierra J. F. *et al.*, (2008): The antimicrobial sensitivity of Streptococcus mutans to nanoparticles of silver, zinc oxide, and gold. *Nanomedicine Nanotechnology,* 4: 237–240.
60. Hrenovic, J., Milenkovic, J., Ivankovic, T.,, and Rajic, N.(2012): Antibacterial activity of heavy metal-loaded natural zeolite.*Journal of Hazardeous Matert,* 201/202:260–264
61. Hu C. H., and Xia, M. S.(2006): Adsorption and antibacterial effect of copper-exchanged montmorillonite on Escherichia coli K88."*Applied Clay Science*, 31:180–184.
62. Hui, Y., Yan-yu , R. Tao, W., Chuang , W.(2016): Preparation and antibacterial activities of Ag/Ag^{+} /Ag^{3+} nanoparticle composites made by pomegranate (Punica granatum) rind extract. Results in Physics, 6 (2016): 299–304
63. Isah, K. U., Jolayemi, B. J., Ahmadu, U., Kimpa, M. I., and Alu, N. (2016): Plasmonic effect of silver nanoparticles intercalated into mesoporous betalain-sensitized-TiO2 film electrodes on photovoltaic performance of dye-sensitized solar cells. Materials for Renewable and Sustainable Energy, 5(10): 1-10.
64. Jamdagni, P., Khatri, P., and Rana, J. S. (2016): Green synthesis of zinc oxide nanoparticles using flower extract of Nyctanthes arbor-tristis and their antifungal activity. Journal of King Saud University - Science. https://doi.org/10.1016/j.jksus.2016.10.002
65. Jiang, Y., Zhang, L., Wen, D., and Ding, Y. (2016). Role of physical and chemical interactions in the antibacterial behavior of ZnO nanoparticles against E. coli. *Materials Science and Engineering: C*, *69*: 1361-1366

66. Karimi, L., and Salem, A. (2011): Analysis of bentonite specific surface area by kinetic model during activation process in presence of sodium carbonat, Microporous and Mesoporous Materials, 141: 81–8.
67. Kassem, M.(2015): Performance evaluation of natural bentonite loaded with zinc oxide for the photocatalytic degradation of methyl red. Romanian Journal of Chemistry, 60(10):957–63.
68. Keller-Besrest, F., Benazeth, S.,and Souleau, C.(1994): Pharmaceutical silver doped clays: an EXAFS study from silver to silicon K-edges absorption," *J. Phys. IV JP*, vol. 4, no. 9, 1994.
69. Khansaa Al-Essa and Ethar M. Al-Essa. Effective Approach of Activated Jordanian Bentonite by Sodium Ions for Total Phenolic Compounds Removal from Olive Mill Wastewater, Journal of Chemistry Volume 2021, Article ID 7405238, 16 pages https://doi.org/10.1155/2021/7405238
70. Kifle, Z. D., Kidanu, B. B., Tadesse, T. Y., Belachew, T. F., and Atnafie, S. A.(2021): Evaluation of in Vivo Antidiarrheal Activity of Solvent Fractions of Hagenia abyssinica (Rosaceae) in Swiss Albino Mice, *Evidence-based Complement. Altern. Med*, 2021, 2021. PMID: 33628317, DOI: 10.1155/2021/8828331
71. Kilonzo M., and Munisi, D. (2021): Antimicrobial activities and phytochemical analysis of Harrisonia abyssinica (Oliv) and Vepris simplicifolia (Verd) extracts used as traditional medicine in Tanzania. *Saudi Journal of Biological Science*, 28(12: 7481–7485.
72. Kim, M. H., Choi, G., Elzatahry, A., Vinu, A., Bin Choy, Y., and Choy, J. H. (2016): Review of clay-drug hybrid materials for biomedical applications. *Clays Clay Minerials*, 64: 115–130.
73. Krishnan, B., and Mahalingam, S.(2017): Improved surface morphology of silver/copper oxide/bentonite nanocomposite using aliphatic ammonium based ionic liquid for enhanced biological activities. *Journal of Molecular Liquid*, 241:1044–1058.
74. Krishnan, B., and Mahalingam, S. (2017a). Ag/TiO2/bentonite nanocomposite for biological applications: Synthesis, characterization, antibacterial and cytotoxic investigations. *Advanced Powder Technology*, *28*(9): 2265–2280. https://doi.org/10.1016/j.apt.2017.06.00.
75. Król-Gracz, A..et al. 2011), Photo-induced chemical reduction of silver bromide to silver nanoparticles, Cent. Eur. J. Chem. 9(6) : 982-989
76. Kukushkina, E.A., Hossain, S.I., Sportelli, M.C., Ditaranto, N., Picca, R.A., Cioffi N.(2021): Ag-based synergistic antimicrobial composites. A critical review. Nanomaterials, 2021:11(7).

77. Kumar, A., and Lingfa, P. (2020); Sodium bentonite and kaolin clays: Comparative study on their FT-IR, XRF, and XRD. Materials Today: Proceedings, 22: 737–742. https://doi.org/10.1016/j.matpr.2019.10.037
78. Kumar, S., Abedin, M. M., Singh, A. K., and Das, S. (2020): Role of Phenolic Compounds in Plant-Defensive Mechanisms. *Plant Phenolics in Sustainable Agriculture*, 517–532. https://doi.org/10.1007/978-981-15-4890-1_22
79. Kuruppu, K. A. S. S., Perera, K. M. K. G., Chamara, A. M. R., and Thiripuranathar, G. (2020): Flower Shaped ZnO-NPs; Phytofabrication, Photocatalytic, Fluorescence Quenching, and Photoluminescence Activities. Nano Express, 1 (2): 020020. doi:10.1088/2632-959x/aba862.
80. Lavorgna *et al.*, (2014):MMT-supported Ag nanoparticles for chitosan nanocomposites: Structural properties and antibacterial activity. Carbohydrate. Polymer, 102: 385–392.
81. Lee, J.M., Charles, D., and Shackelford, (2005): Solution Retention Capacity as an Alternative to the Swell Index Test for Sodium Bentonite. *Geotechnical Testing Journal*, 28(1):61-70.
82. Leena, S.(2017): Activation of raw bentonite (afar region) using sulfuric acid for rapeseed and niger seed oil bleaching. A Thesis in Process Engineering Stream, 19 June 2017.Addis Ababa University.
83. Lei, C., Pi, M., Jiang, C., Cheng, B., and Yu, J. (2017): Synthesis of hierarchical porous zinc oxide (ZnO) microspheres with highly efficient adsorption of Congo red. In *Journal of Colloid and Interface Science* (Vol. 490). https://doi.org/10.1016/j.jcis.2016:11.049
84. Lin, H., Yang, M., Tang, H., Pan, F.(2018): Effect of minor Sc on the microstructure and mechanical properties of AZ91 Magnesium Alloy. Prog Nat Sci Mater Int [Internet]. 2018;28(1):66–73. Available from: https://doi.org/10.1016/j.pnsc.2018.01.006.
85. Maga˜na , S.M., Quintana , P., Aguilar , D.H., Toledo , J.A., ngeles-Cha´vez, C.A., Cort´es, M.A., Le´on, L., Freile-Pelegr´ın, Y., L´opez, T., Torres S´anchez, R.M.(2008): Antibacterial activity of montmorillonites modified with silver. Journal of Molecule and Catalyst A, 281 (2008): 192–199.
86. Maheshwaran, G., Malai Selvi, M., Selva Muneeswari, R., Nivedhitha Bharathi, A., Krishna Kumar, M., and Sudhahar, S.(2021): Green synthesis of lanthanum oxide nanoparticles using Moringa oleifera leaves extract and its biological activities. *Adv. Powder Technol*, 32(6): 1963–1971.

87. Maisanaba, S., Pichardo, S., Puerto, M., Gutiérrez-Praena, D., Cameán, A. M., and Jos, A. (2015): Toxicological evaluation of clay minerals and derived nanocomposites: A review,Environomental Research, 138: 233–254.
88. Manfredini, T., and Hanuskova, M. (2012): Natural raw materials in ‘ Traditional ’ ceramic manufacturing, 2012: 465–470.
89. Mankad, M., Patil, G., Patel, S., Patel, D., and Patel, A. (2016): Green synthesis of zinc oxide nanoparticles using Azadirachta indica A. Juss. leaves extract and its antibacterial activity against Xanthomonas orzyae pv. oryzae. *Annals of Phytomedicine : An International Journal*, *5*(2):76–86. https://doi.org/10.21276/ap.2016.5.2.9
90. Melkamu W. W., and Bitew, L. T.(2021): Green synthesis of silver nanoparticles using Hagenia abyssinica (Bruce) J.F. Gmel plant leaf extract and their antibacterial and anti-oxidant activities. *Heliyon*, 7(11): e08459.
91. Meng, N., Zhou, N., Zhang, S., and Shen, J.(2009): Controlled release and antibacterial activity chlorhexidine acetate (CA) intercalated in montmorillonite.382:45–49.
92. Meshram, S., Limaye, R., Ghodke, S., Nigam, S., Sonawane, S., and Chikate, R. (2011): Continuous flow photocatalytic reactor using ZnO-bentonite nanocomposite for degradation of phenol. Chemical Engineering Journal, 172(2–3): 1008-1015.
93. Metge, D.W., Harvey, R.W., Eberl,D.D., Wasylenki, L.E., Williams, L.B. (2009): Evaluating the oxidation state of antibacterial minerals. Geo-chemistry. Cosmochim. Acta, Suppl. 2009(73):A875
94. Moharram, A. H., Mansour, S. A., Hussein, M. A., and Rashad, M.(2014): Direct Precipitation and Characterization of ZnO Nanoparticles,” Journal of Nanomaterials 2014: 5 pages http://dx.doi.org/10.1155/2014/716210
95. Mohanraj, V. J., and Chen, Y. (2007): Nanoparticles - A review, *Trop. J. Pharm. Res.*, 5(1) 561–573.
96. Motshekga, S. C., Ray, S. S., Onyango, M. S., and Momba, M. N. B. (2013): Microwave-assisted synthesis, characterization and antibacterial activity of Ag/ZnO nanoparticles supported bentonite clay. Journal of Hazardous Materials, 262:439–446. https://doi.org/10.1016/j.jhazmat.2013.08.074

97. Motshekga, S. C., Ray, S. S., Onyango, M. S., and Momba, M. N. B. (2015). Preparation and antibacterial activity of chitosan-based nanocomposites containing bentonite-supported silver and zinc oxide nanoparticles for water disinfection. *Applied Clay Science*, *114*, 330–339. https://doi.org/10.1016/j.clay.2015.06.010

98. Motshekga, S. C., Ray, S. S., Onyango, M. S., and Momba, M. N. B.(2013): Microwave-assisted synthesis, characterization and antibacterial activity of Ag/ZnO nanoparticles supported bentonite clay. Journal of Hazardous Materials, 262:439–446.

99. Movasaghi, Z., Rehman, S., and Rehman, I. U. (2008): Fourier transform infrared (FTIR) spectroscopy of biological tissues. *Appl. Spectrosc. Rev,* 43(2):134–179, 2008.

100. Moosavi, M. (2017): Bentonite Clay as a Natural Remedy. A Brief Review, Iran Journal Public Health, 46(9): 1176–1183.

101. Murthy, H. C. A., Desalegn, T., Kassa, M., Abebe, B., and Assefa, T.(2020):Synthesis of Green Copper Nanoparticles Using Medicinal Plant Hagenia abyssinica (Brace) JF. Gmel. Leaf Extract: Antimicrobial Properties. *J.ournal of Nanomaterils*, 2020: 2020.

102. Murthy, H. C.A., Desalegn Zeleke, T., Ravikumar, C. R., Anil Kumar, M. R., and Nagaswarupa, H. P.(2020): Electrochemical properties of biogenic silver nanoparticles synthesized using Hagenia abyssinica (Brace) JF. Gmel. medicinal plant leaf extract," *Materials Research. Express*, 7(5):2020.

103. Mustapha, S., Ndamitso, M. M., Abdulkareem, A. S., Tijani, J. O., Shuaib, D. T., Ajala, A. O., and Mohammed, A. K. (2020): Application of TiO_2 and ZnO nanoparticles immobilized on clay in wastewater treatment: a review. In Applied Water Science 10(1):1-36

104. Nadzir, M.M., Idris, F.N., Hat, .K. (2019): Green synthesis of silver nanoparticle using Gynura procumbens aqueous extracts, AIP Conference Proceeding, 2124 (2019):l 1–7.

105. Nagarajan, P., Rajagopalan,V. (2008): Enhanced bioactivity of ZnO nanoparticles-an antimicrobial study, Science and Technology Advanced Materials,9(3): doi: 10.1088/1468-6996/9/3/035004.

106. Negash, L.(1995): .*Indigenous trees of Ethiopia: biology, uses and propagation techniques*, no. March. 1995.

107. Nethravathi, P. C., Shruthi, G. S., Suresh, D., Udayabhanu, H., Nagabhushana, H., and Sharma, S. C. (2015): Garcinia Xanthochymus Mediated green Synthesis of ZnO Nanoparticles:

Photoluminescence, Photocatalytic and Antioxidant Activity Studies. Ceramics Int. 41 (7): 8680–8687. doi:10.1016/j.ceramint.2015.03.084.

108. Nikaido, H. (2009): Multidrug Resistance in Bacteria. Annual Review Biochemistry.78: 119–146.

109. Obakiro S. B. *et al.*,(2021): Traditional Medicinal Uses, Phytoconstituents, Bioactivities, and Toxicities of Erythrina abyssinica Lam. ex DC. (Fabaceae): A Systematic Review. *Evidence-based Complement. Altern. Med.*, 2021, 2021.

110. Panyala, N. R., Pena-Mendez, E. M., and Havel, J (2008). Silver or silver nanoparticles: a hazardous threat to the environment and human health, Journal of Applied Biomedicine, 6: 117–129, www.zsf.jcu.cz/jab

111. Park S., and Jang, Y. (2003): Preparation and characterization of activated carbon fibers supported with silver metal for antibacterial behavior. Journal of Colloid and Interface Science, 261: 238–243.

112. Pourabolghasem, H., Ghorbanpour, M., and Shayegh, R.(2016): Antibacterial activity of copper-doped montmorillonite nanocomposites prepared by alkaline ion exchange method. *Journal of Physical Science*, 27: 1–12.

113. Pouraboulghasem, H., Ghorbanpour, M., Shayegh, R., and Lotfiman, S. (2016): Synthesis, characterization and antimicrobial activity of alkaline ion-exchanged ZnO/bentonite nanocomposites. *Journal of Central South University*, *23*(4): 787–792. https://doi.org/10.1007/s11771-016-3124-y

114. Qurat-ul-Ain Naqvi, Amber Kanwal, Qaseem, S., Naeem, M., Rizwan Ali, S., Shaffique, M., Maqbool, M.(2019): Size-dependent inhibition of bacterial growth by chemically engineered spherical ZnO nanoparticles. Journal of Biological Physics, 45:147–159 https://doi.org/10.1007/s10867-019-9520-4

115. Rahmati, Z., Abdi, J., Vossoughi, M.,and Alemzadeh, I. (2020): Ag-doped magnetic metal organic framework as a novel nanostructured material for highly efficient antibacterial activity. Environmental Research, 188: 109555

116. Rajakannu, S., Shankar, S., Perumal, S.,and Subramanian, S. (2015): Original Research Article Biosynthesis of Silver Nanoparticles using Garcinia mangostana Fruit Extract and their

Antibacterial , Antioxidant Activity. International Journal of Currernt Microbiology Applied Scicence, 4:944–952.

117. Rajendran, S. P., and Sengodan, K. (2017). Synthesis and Characterization of Zinc Oxide and Iron Oxide Nanoparticles Using Sesbania grandiflora Leaf Extract as Reducing Agent. Journal of Nanoscience, 17:1-7

118. Rapacz-kmita, A., Bu, M. M., Stodolak-zych, E., Miko, M., Dudek, P., and Trybus, M.(2017): Characterisation , in vitro release study , and antibacterial activity of montmorillonite-gentamicin complex material. 70: 471–478.

119. Şahin, Ö. Kaya, M., and Saka, C. (2015): "Plasma-surface modification on bentonite clay to improve the performance of adsorption of methylene blue. Applied Clay Science, vol. 116/117: 46–53.

120. Sajadi, S. M., Kolo, K., Hamad, S. M., Mahmud, S. A., Barzinjy, A. A., and Hussein, S. M.(2018): Green Synthesis of the Ag/Bentonite Nanocomposite UsingEuphorbia larica Extract: A Reusable Catalyst for Efficient Reduction of Nitro Compounds and Organic Dyes. *ChemistrySelect*, 3(43):12274–12280.

121. Salam, H., Sivaraj, R., and Venckatesh, R. (2014): Green synthesis and characterization of zinc oxide nanoparticles from Ocimum basilicum L. var. purpurascens Benth.-Lamiaceae leaf extract. Materials Letters, 131, 16-18

122. Salwa, D., Abayazeed, and Essam El-Hinnawi.(2021): Characterization of Egyptian Smectitic Clay Deposits by Methylene Blue Adsorption. *American Journal of Applied Sciences*, 6(12): 1282-1286.

123. Sánchez-López, E., Gomes, D., Esteruelas, G., Bonilla, L., Lopez-Machado, A. L., Galindo, R., Cano, A., Espina, M., Ettcheto, M., Camins, A., Silva, A. M., Durazzo, A., Santini, A., Garcia, M. L., and Souto, E. B. (2020): Metal-based nanoparticles as antimicrobial agents: An overview. *Nanomaterials*, *10*(2): 1–39. https://doi.org/10.3390/nano10020292

124. Santos, M.F., Oliveira, C.M., Tachinski, C.T., Fernandes, M.P., Pich, C.T., Angioletto, E., Riella, H.G.,. Fiori, M.A.(2011): Bactericidal properties of bentonite treated with Ag+ and acid, International Journal of. Minerals Process. 100 (2011) 51–53.

125. Sasikala, S. P., Nibila, T. A., Babitha, K. B., Mohamed, A. A. P., and Solaiappan, A. (2019): Competitive photo-degradation performance of ZnO modified bentonite clay in water

containing both organic and inorganic contaminants. *Sustainable Environment Research*, *29*(1): 1-12.

126. Schneid *et al.*,(2014): Silver nanoparticle-ionic silsesquioxane: A new system proposed as an antibacterial agent. Journal Materials.Chemistry. B, 2:1079–1086.

127. Senthil kumar, N., Nandhakumar, E., Priya, P., Soni, D., Vimalan, M., Potheher, I.V.(2017): Synthesis of ZnO nanoparticles using leaf extract of Tectona grandis (L.) and their anti-bacterial anti-arthritic anti-oxidant and in vitro cytotoxicity activities. New Journal of Chemistry, 41:10347–10356.

128. Shah, L. A., Khattak, N. S., Valenzuela, M. G. S., Manan, A., & Valenzuela Díaz, F. R. (2013): Preparation and characterization of purified Na-activated bentonite from Karak (Pakistan) for pharmaceutical use. Clay Minerals, 48(4): 595–603. https://doi.org/10.1180/claymin.2013.048.4.03

129. Shalini Agarwa, Y. K., Saraswat, Saraswat, V. K.(2019): Study of Optical Constants of ZnO Dispersed PC/PMMA Blend Nanocomposites. Open Physics Journal, 5: 2019

130. Shameli, K., Bin Ahmad, M., Zargar, Yunus, A., Rustaiyan, and Ibrahim, N. A. (2011): Synthesis of silver nanoparticles in montmorillonite and their antibacterial behavior. *International Journal of Nanomedicine*, 6:581–590.

131. Shameli, K., Ahmad, M.B., Yunus, W.M.Z.W., Ibrahim, N.A., Gharayebi, Y., Sedaghat, S. (2010): Synthesis of silver/montmorillonite nanocomposites using γ-irradiation, International Journal of Nanomediceine, 5 (2010): 1067–1077.

132. Shameli, K., Ahmad, M..B., Zargar, M., Yunus, W.M., Ibrahim, N.A., Shabanzadeh, P., Moghaddam, M.G.(2011): Synthesis and characterization of silver/montmorillonite/ chitosan bionanocomposites by chemical reduction method and their antibacterial activity. International Journal of Nano medicine. 6 (2011) 271–284

133. Shameli, K.*et al.*,(2012): Green biosynthesis of silver nanoparticles using callicarpa maingayi stem bark extraction. Molecules, 17(7): 8506–8517.

134. Shao, W., Liu, X., Min, H., Dong, G., Feng, Q., and Zuo, S. (2015): Preparation, characterization, and antibacterial activity of silver nanoparticle-decorated graphene oxide nanocomposite. ACS Applied Materials and Interfaces, *7*(12): 6966–6973. https://doi.org/10.1021/acsami.5b00937

135. Sharma, K., Guleria, S., Razdan, V.K.(2020): Green synthesis of silver nanoparticles using Ocimum gratissimum leaf extract: characterization, antimicrobial activity and toxicity analysis. Journal of Plant Biochemistry and Biotechnology, 29 (2020): 213–224.

136. Sivakumar,P., Lee, M., Kim,Y.S.,Shim,M.S.(2018): Photo-triggered antibacterial and anticancer activities of zinc oxide nanoparticles, Journal of Materials Chemistry B 6(30), DOI: 10.1039/C8TB00948A

137. Slane, J., Vivanco, J., Rose, W., Ploeg, H. L., and Squire, M. (2015):Mechanical, material, and antimicrobial properties of acrylic bone cement impregnated with silver nanoparticles. Materials Scicence Engineering, 48:188–196.

138. Slavin, Y.N., Asnis, J., Häfeli, U.O.,and Bach,H.(2017): Metal nanoparticles: Understanding the mechanisms behind antibacterial activity. Journal of Nanobiotechnology. 15: 65.

139. Sondi I., and Salopek-Sondi, B.(2004): Silver nanoparticles as antimicrobial agent: A case study on E. coli as a model for Gram-negative bacteria. *Journal of Colloid Interface Science.*, 275:177–182.

140. Sruthi, B., Dharan, and Rani, V.(207): Study on the effect of pH on clay. International Research Journal of Engineering and Technology, vol. 4(11):1751-1755.

141. Susanto, H., et al., (2018): Moringa oleifera Leaf Powder Madura Variety: Characterization and Biomaterials Property for Biomedical and Nanotechnology Application. Journal of Physics: ConferenceSeries 1093(2018) 012007 doi :10.1088/1742-6596/1093/1/012007

142. Suresh, J., Pradheesh, G., Alexramani, V., Sundrarajan, M., and Hong, S. I. (2018): Green synthesis and characterization of zinc oxide nanoparticle using insulin plant (Costus pictus D. Don) and investigation of its antimicrobial as well as anticancer activities. Advances in Natural Sciences: Nanoscience and Nanotechnology, 9(1). https://doi.org/10.1088/2043-6254/aaa6f1

143. Suyoulema, J. Li., Wang, W., and Sarina, A. (2009): Study of photodegradation of sulforhodamine B on Au-TiO_2/bentonite under UV and visible light irradiation. Solid State Sciecnce, 11: 2037–2043.

144. Tanaka, R., Matsunanga, S., and Sasaki, T.(1989): A new flavanone derivative from the leaves of Tsuga diversifolia. *Planta Med*, 55(6):570–571.

145. Targino *et al.*,(2014): An innovative approach to treating dental decay in children. A new anti-caries agent. Journal Matererials. Scicence, 25: 2041–2047.

146. Theivasanthi,T., and Alagar, M.(2011): Anti-bacterial Studies of Silver Nanoparticles," no. 1.

147. Uddin, F. (2018): Montmorillonite: An Introduction to Properties and Utilization.Current Topics in the Utilization of Clay in Industrial and Medical Applications. pp. 3–24, DOI: 10.5772/intechopen.77987

148. Unnithan, R. R. (2017): Characterization of Na_2CO_3 activated Calcium Bentonite and its application as a GCL. International Journal of Engineering Research and Technology (IJERT), 5(08):3–6.

149. Upadhyaya, H.,Shome, S., Sarma, R., Tewari, S.,Bhattacharya, M. K.and Panda, S. K.(2018): Green Synthesis, Characterization and Antibacterial Activity of ZnO Nanoparticles. American Journal of Plant Sciences, (9): 1279-1291

150. Venkatathri, N. (2006): Characterization and catalytic properties of a naturally occurring clay, Bentonite. Bulletin of the Catalysis Society of India 5 (2006): 61-72

151. Wani, I. A., Ganguly, A., Ahmed, J., and Ahmad, T. (2011): Silver nanoparticles: Ultrasonic wave assisted synthesis, optical characterization and surface area studies. *Materials Letter*, 6(3): 520–522.

152. Wolde, T., Bizuayehu, B., Hailemariam, T., and Tiruha, K.(2016): Phytochemical analysis and Antimicrobial activity of Hagenia Abyssinica. *Indian Journal of* Pharmacy and Pharmacology, 3(8):1-9.

153. Wu, T .S., Wang, K.X., Li, G. D., Sun, S.-Y., Sun, J., Chen, J.-S. (2010): Montmorillonitesupported Ag/TiO2 nanoparticles: an efficient visible-light bacteria photodegradation material. ACS Appl. Mater. Interfaces 2 (2010): 544–550.

154. Xu, H., Zhang, D., Xu, A., Wu, F., and Cao, R. (2015): Quantum Sized Zinc Oxide Immobilized on Bentonite Clay and Degradation of C.I. Acid Red 35 in Aqueous under Ultraviolet Light. International Journal of Photoenergy, 2015.

155. Yang, G., Wang, . C., Hong, F., Yang, X.,and Cao, Z. (2015): Preparation and characterization of BC/PAM-AgNPs nanocomposites for antibacterial applications," *Carbohydrate Polymer*, 115,:636–642.

156. Yang, H., Du, C., Jin, S.., and Tang, A. (2007): Preparation and characterization of SnO2 nanoparticles incorporated into talc porous materials (TPM). *Materials Letter*,, 61(17):3736–3739.

157. Yang, T., Wen, X. D., Li, J., and Yang, L.(2006): Theoretical and experimental investigations on the structures of purified clay and acid-activated clay. Applied Surface Science, 252: 6154–6161.

158. Yang, Z., Peng, H., Wang, W., and Liu, T. (2010): Crystallization behavior of poly(ε-caprolactone)/layered double hydroxide nanocomposites. *Journal of Applied Polymer Science*, 116(5): 2658–2667.

159. Ye, W.M., He, Y., Chen, Y.G., Chen, B., Cui, Y.J.(2016): Thermochemical effects on the smectite alteration of GMZ bentonite for deep geological repository. Environmental Earth Science, 75 (10):1–11.

160. Yin, I.X., Zhang, J., Zhao, I.S., Mei, M.L., Li, Q., Chu, C.H.(2020): The antibacterial mechanism of silver nanoparticles and its application in dentistry. International Journal of Nanomedicine, 15:2555–62.

161. Yukselen, Y., and Kaya, A. (2008): Suitability of the methylene blue test for surface area, cation exchange capacity and swell potential determination of clayey soils. Engineering Geology, 102: 38-45

162. Zak, A. K., Hashim, A. M., and Darroudi, M. (2014): Optical properties of ZnO/$BaCO_3$ nanocomposites in UV and visible regions. Nanoscale Research Letters, 9(1): 1-6.

163. Zak, A.K., Yousefi, R., Abd Majid, W.H., Muhamad, M.R.(2012): Facile synthesis and X-ray peak broadening studies of Zn1− xMgxO nanoparticles. Ceramic Internation, 38: 2059–2064.

164. Zdravković ,S. A.(2019): Application of activated bentonite for the removal of direct and reactive dye from aqueous solutions. Chemical Industry & Chemical Engineering Quarterly, 4(25): 341−351.

165. Zhang, H., Chen, B., Jiang, H., Wang, C., Wang, H., Wang, X. (2011): A strategy for ZnO nanorod mediated multi-mode cancer treatment. Biomaterials, 32: 1906–14.

166. Zholobak, N. M., Ivanov, V. K., Shcherbakov, A. B.(2016): Interaction of Nanoceria with Microorganisms. In N,anobiomaterials in Antimicrobial Therapy; Elsevier, 2016: 419–450. https://doi.org/10.1016/B978-0-323-42864-4.00012-9

167. Zuber, M., Zia, K. M., Mahboob, S., Hassan, M., and Bhatti, I. A. (2010): Synthesis of chitin-bentonite clay based polyurethane bio-nanocomposites," *International Journal of Biolological Macromolecules*, 47(2): 196–200. https://doi.org/10.1007/s11771-016-3124-y